VILNIUS UNIVERSITY

Georgij Kostiuk

Single molecule studies of the monomeric restriction endonuclease BcnI-DNA interactions

Doctoral dissertation

Physical sciences, biochemistry (04 P)

Vilnius, 2017

The work presented in this doctoral dissertation has been carried out at the Institute of Biotechnology, Vilnius University during 2010-2014.

Supervisor:

Prof. dr. **Virginijus Šikšnys** (Vilnius University, physical sciences, biochemistry - 04 P). From 2010 october 1st till 2014 september 30th.

Scientific advisor:

Dr. **Giedrius Sasnauskas** (Vilnius University, physical sciences, biochemistry - 04 P)

VILNIAUS UNIVERSITETAS

Georgij Kostiuk

Monomerinės restrikcijos endonukleazės BcnI-DNR sąveikos tyrimas pavienių molekulių metodais

Daktaro disertacija

Fiziniai mokslai, biochemija (04 P)

Vilnius, 2017

Disertacija rengta 2010-2014 m. Vilniaus universiteto Biotechnologijos institute studijuojant doktorantūroje ir ginama eksternu.

Mokslinis vadovas:

Prof. dr. **Virginijus Šikšnys** (Vilniaus universitetas, fiziniai mokslai, biochemija - 04 P). Nuo 2010 m. spalio 1 d. iki 2014 m. rugsėjo 30 d.

Mokslinis konsultantas:

Dr. **Giedrius Sasnauskas** (Vilniaus universitetas, fiziniai mokslai, biochemija - 04 P).

CONTENTS

LIST OF ABBREVIATIONS

2-ME	2-mercaptoethanol
AFM	atomic force microscopy
ALEX	alternating-laser excitation
BSA	bovine serum albumin
CCD	charge-coupled camera
COT	1,3,5,7 cyclooctatetraene
DTT	dithiothreitol
EDTA	ethylenedinitrilotetraacetic acid
EMCCD	electron-multiplying charge-coupled camera
EMSA	electrophoretic mobility shift assay
FCCS	fluorescence cross-correlation spectroscopy
FCS	fluorescence correlation spectroscopy
FP	fluorescent protein
FRET	Förster resonance energy transfer
GFP	green fluorescent protein
GOD-CAT	glucose oxidase – catalase
GR	germinal recombination
IC	internal conversion
ISC	intersystem crossing
LRET	luminescence resonance energy transfer
MSD	mean-squared displacement
MTase	methyltransferase
NA	numerical aperture
NBA	4-nitrobenzylalcohol
PAGE	polyacrylamide gel electrophoresis

Pi	phosphate
PIE	pulsed interleaved excitation
PIFE	protein induced fluorescence enhancement
PCA – PCD	protocatechuic acid – protocatechuate-3,4-dioxygenase
PEG	polyethylene glycol
POC	pyranose oxydase – catalase
PSD	position sensitive detector
QD	quantum dot
R – M	restriction – modification system
REase	restriction endonuclease
ROS	reactive oxygen species
ROXS	reducing and oxidazing system
S	C or G
S_0, S_1, S_2	singlet states of the electrons
SDS	sodium dodecyl sulfate
T_0, T_1	triplet states of the electrons
TCEP	tris(2-carboxyethyl)phosphine
TEMED	N,N,N’,N’-tetramethylethylenediamine
THF	tetrahydrofuran
TIRF	total internal reflection fluorescence
Tris	2-amino-2-hydroxymethyl-1,3-propanediol
TROLOX	6-hydroxy-2,5,7,8-tetramethylchroman-2-carboxylic acid
TXQ	TROLOX quinone
UV-Vis	ultraviolet visible
VR	vibrational relaxation
WLC	worm-like chain

INTRODUCTION

Many vital cellular processes, including DNA replication, DNA repair, gene expression control, recombination and antiviral defence are mediated by proteins that recognize specific DNA targets. These proteins must locate their target sites in the sea of the non-specific DNA sequences. Understanding molecular mechanisms of how DNA binding proteins locate specific sites amongst huge amounts of non-specific DNA is a fundamental problem in both biology and biophysics. Different regulatory proteins, like transcription factors, must find their target sites first to initiate complex biological processes such as gene activity regulation. Enzymes that excise or modify DNA bases or hydrolyse phosphodiester bonds at specific sites have not only to locate their target sequence but also trigger a chemical reaction upon formation of the specific protein-DNA complex.

Type II restriction enzymes (REases) form one of the largest groups of site-specific DNA-acting enzymes. They recognize short (4-8 bp) DNA sequences and cleave both DNA strands within or close to the recognition sites. REases are part of restriction-modification (R – M) systems that protect host bacteria and archaea cells from foreign (e.g, bacteriophage) DNA (Pingoud et al., 2014). Due to simple cofactor requirements (most enzymes require only Mg^{2+} ions), extraordinary specificity and efficiency, REases became indispensable tools for *in vitro* DNA manipulations, and also convenient model systems for the studies of target site location, site-specific DNA recognition, and DNA cleavage by site-specific proteins. For example, studies performed on REases have contributed to our understanding of facilitated diffusion, i.e. target site location mechanism employed by most site-specific proteins involving sliding and hopping (Halford, 2004). Of particular interest are studies that examine the relationship between

formation of a specific REase complex with the target site(s), enzyme activation and mechanisms of DNA cleavage (Kurpiewski et al., 2004). Indeed, despite a similar function – DNA cleavage at specific sites – REases are a highly heterogeneous group of enzymes that differ in their oligomeric structure, domain organization, recognition sites, and reaction mechanisms. For example, orthodox restriction enzymes, like EcoRI (Kim et al., 1990) or MunI (Deibert, 1999), are symmetric homodimers, that place the catalytic centre and sequence recognition elements of one subunit against the scissile phosphate and DNA bases in one half of their palindromic recognition site, and the other subunit against the symmetry related half-site. A similar strategy, where the number of cleaved DNA strands matches the number of catalytic centres, is also employed by the homotetrameric Type IIF enzymes, which simultaneously bind and cleave two copies of the symmetric recognition sequence (e.g., Cfr10I (Siksnys et al., 1999), NgoMIV (Embleton et al., 2001), Bse634I (Zaremba et al., 2005), and Cfr42I (Gasiunas et al., 2008)), and some Type IIS REases, which recognize asymmetric DNA sequences and cut DNA at one side of the recognition site, including the monomeric REase Mva1269I (it contains two active sites in one polypeptide chain (Armalyte et al., 2005)), and the monomeric enzyme FokI (it dimerizes upon DNA binding (Catto et al., 2008)).

However, some enzymes introduce double-strand DNA breaks employing just a single catalytic centre. For example, Type IIS REase BfiI is a homodimer that contains a single catalytic centre at the interface of the nuclease domains, and uses it for sequential nicking of the two DNA strands. Throughout these reactions, which involve swivelling of the catalytic centre between DNA strands of opposite polarity, the catalytic domains of BfiI remain tethered to the DNA via the DNA recognition domain (Sasnauskas et al., 2010). Available structural and biochemical data indicate that some other REases also employ a single catalytic centre for dsDNA cleavage. For example, BcnI is a monomeric REase, which

forms an asymmetric complex with its pseudopalindromic recognition site 5′-CC/SGG-3′ (where S is C or G, and ‘/’ marks cleavage position), placing the single catalytic centre in the vicinity of the scissile phosphate in one DNA strand (Sokolowska et al., 2007). This raised a question of how BcnI accomplishes cleavage of double stranded DNA. We have employed various biochemical and biophysical methods, including bulk kinetics and single-molecule techniques, to elucidate the target site location and DNA cleavage mechanisms of BcnI.

The specific aims of this study were:

i to determine the mechanism of double-stranded DNA cleavage employed by the monomeric restriction endonuclease BcnI;

ii to characterise the process of target site location employed by BcnI, including the conformational states of BcnI, dynamics of specific and non-specific BcnI-DNA interactions, and facilitated diffusion on the DNA using various single molecule techniques.

Scientific novelty:

We present the first detailed kinetic analysis of double-stranded DNA cleavage by a monomeric restriction enzyme;

This is the first study that addresses the mechanism of target site location by the site-specific DNA binding protein using a combination of different single-molecule techniques, including, but not limited to, confocal microscopy study of DNA binding and conformational dynamics of BcnI using single/double-labelled protein, and BcnI movement on stretched DNA using a combination of TIRF microscopy and magnetic tweezers.

Practical value

The set of single-molecule techniques employed and described here could be successfully applied to characterisation of other DNA-binding proteins, including DNA polymerases, CRISPR-Cas endonucleases, and various other DNA modifying enzymes that are currently used as molecular tools in genetic engineering and genome editing. The BcnI reaction mechanism characterised here also enabled engineering of nicking endonucleases, i.e. BcnI variants hydrolysing only one particular DNA strand at the recognition site (Kostiuk et al., 2011).

The major findings presented for defence in this thesis:

- Monomeric REase BcnI sequentially hydrolyses two DNA strands within the pseudopalindromic recognition site 5′-CCSGG-3′;
- The switch in BcnI orientation on the DNA occurs without dissociation of the enzyme into bulk solution;
- Target site location and the switch in BcnI orientation involve sliding and jumping of the enzyme on the nonspecific DNA;
- The conformational flexibility of BcnI and the relative positions of the recognition and catalytic subdomains depend on DNA and divalent metal ion binding.

1. REVIEW OF LITERATURE

The first two parts of this review cover various fluorescence-based and single molecule force microscopy techniques, with a special focus on methods used in this work. The final part of this review is dedicated to facilitated diffusion of proteins on DNA, a target-site location mechanism demonstrated for many DNA-acting enzymes, including the monomeric restriction endonuclease BcnI.

1.1. Single molecule fluorescence spectroscopy

1.1.1. Fluorescence

Luminescence is the emission of light from any substance, and occurs from electronically excited states. Upon absorption of a photon, electrons of the fluorophores are excited from the ground singlet state (S_0) to a certain vibrational energy level of higher electronic singlet states (S_1, S_2, etc.). After excitation, electrons rapidly relax to the lowest vibrational level of S_1 singlet state by vibrational relaxation (VR) and internal conversion (IC) processes. The following energetic return from S_1 to S_0 singlet state, which causes energy release by light emission, is called **fluorescence** (Figure 1A). Fluorescence emission spectra are usually independent of the excitation wavelength, due to the fact that electrons rapidly return from higher excited vibrational state levels to the lowest vibrational state level of S_1 by VR. In excited singlet states, the electron of the fluorophore in the excited orbital is paired by opposite spin to the second electron in the ground-state orbital. Consequently, return to the ground state is spin-allowed and occurs rapidly by emission of a photon. Fluorescence typically occurs at lower energies or longer wavelengths than excitation spectra because part of the energy is lost during the return to the lowest vibrational level of S_1 singlet state. This

phenomenon is known as **Stokes shift** and is evaluated as the difference between absorption and emission maxima (Δλ, Figure 1B). The energy of the S_1 excited state can also be dissipated by non-radiative heat release or by quenching, when energy is transferred to another molecule during a collision.

Molecules can also undergo a spin conversion from S_1 to T_1, which is known a intersystem crossing (ISC) to the first triplet state T_1. Emission from T_1 is termed **phosphorescence**, and is generally shifted to longer wavelengths (lower energy) relative to the fluorescence. Reversible ISC process transits electron back to the S_1 state and yields **delayed fluorescence**. Transition from T_1 to the singlet ground state S_0 is forbidden, and as a result the rate constants for triplet emission are several orders of magnitude lower than those for fluorescence (Figure 1A) (Lakowicz, 2006).

1.1.2. Förster resonance energy transfer

Förster resonance energy transfer (FRET) is the phenomenon based on the non-radiative energy transfer that occurs between a donor (D) fluorophore molecule in the excited state and an acceptor (A) molecule in the ground state. The fluorophore donor molecules typically emit light (see 1.1.1.) at shorter wavelengths than absorption spectrum of the acceptor and partially overlaps with it (*J(λ)*, Figure 1B). Energy transfer occurs without the appearance of a photon and is the result of long range dipole-dipole interactions between the donor and the acceptor. The transferred energy excites acceptor and enables it to emit light (see 1.1.1.), although acceptor does not need to be fluorescent because RET does not involve emission of light by the donor (Figure 1C). Förster resonance energy transfer is characterized by the rate $k_T(r)$:

$$k_T(r) = \frac{1}{\tau_D}\left(\frac{R_0}{r}\right)^6 \quad (1)$$

where τ_D is the decay time of the donor in the absence of acceptor, R_0 is the Förster radius, and r is the distance between donor and acceptor. Förster radius (R_0) is the characteristic measure of the resonance energy transfer, which is a constant for a certain donor-acceptor pair of fluorophores. When the donor-to-acceptor distance (r) equals to R_0, then resonance energy transfer rate equals donor decay rate in the absence of acceptor ($1/\tau_D$) and at this distance, half the donor molecules decay by energy transfer and half decay by the usual radiative and non-radiative rates. If the transfer rate is faster than donor decay in the absence of acceptor, then transfer is considered as efficient, if slower –as inefficient. For convenience the measure of FRET efficiency was introduced. It is the fraction of photons absorbed by the donor, which are transferred to the acceptor:

$$E_{FRET} = \frac{k_T(r)}{k_T(r) + \tau_D^{-1}} \quad (2)$$

The given fraction is the ratio of the transfer rate to the total decay rate of the donor in the presence of acceptor. Combination of equations (1) and (2) gives us the following expression for the FRET efficiency (E_{FRET}) (eq. 3):

$$E_{FRET} = \frac{1}{1 + \left(\frac{r}{R_0}\right)^6} \quad (3)$$

Equation (3) reveals that FRET efficiency is very sensitive to the distance changes between the donor and the acceptor. In the range of 0.2-0.8, E_{FRET} linearly depends on the distance between donor and acceptor (Figure 1D), and for this reason FRET is used as a "spectroscopic ruler" to measure distances between different sites of macromolecules or distances between different interacting macromolecules (protein-protein, protein-nucleic acids) (Stryer, 1978). Multiple methods employing FRET were developed that allow detection and observation of biochemical processes at the single molecule level (Joo et al., 2008; Kim and Ha, 2013; Preus and Wilhelmsson, 2012; Roy et al., 2008; Sisamakis et al., 2010).

To implement distance measurements, the distance between donor and acceptor on the investigated protein or nucleic acids sites must be in the linear region, and the Förster radius (R_0) for the corresponding pair of fluorophores must be calculated.

Förster radius (R_0) depends on multiple factors (eq. (4)), such as dipole orientation factor (κ^2, dynamic averaged value of which is 2/3) (Loura, 2012), quantum yield (Φ_D) of the donor fluorescence in the absence of acceptor, spectral overlap integral ($J(\lambda)$), Avogadro's number (N) and refractive index (n) of the medium. All terms of the equation are constants except for Φ_D and $J(\lambda)$, which have to be experimentally determined to calculate Förster radius at the actual experimental conditions (Lakowicz, 2006).

$$R_0^6 = \frac{9000\ln(10)\kappa^2\Phi_D J(\lambda)}{128\pi^5 N n^4} \quad (4)$$

The fluorescence quantum yield (Φ_D) (eq. (5)) is the ratio of the number of emitted photons to the number of absorbed photons, or the fraction of fluorophores that decay through emission (eq. 5):

$$\Phi_D = \frac{\#\ of\ photons\ emitted}{\#\ of\ photons\ absorbed} = \frac{\Gamma}{\Gamma + k_{nr}} \quad (5)$$

where Γ is the sum of radiative decay constants, k_{nr} – the non-radiative decay constant. Quantum yield of the donor (Φ_D) is determined by comparison of the fluorophore to standard fluorophores (Vámosi et al., 1996) (see 2.2.8.1).

The overlap integral $J(\lambda)$ (eq. (6), Figure 1B) expresses the degree of spectral overlap between the donor emission and the acceptor absorption:

$$J(\lambda) = \frac{\int_0^\infty F_D(\lambda)\varepsilon_A(\lambda)\lambda^4 d\lambda}{\int_0^\infty F_D(\lambda)\, d\lambda} \quad (6)$$

$F_D(\lambda)$ is the corrected fluorescence intensity of the donor at λ, $\varepsilon_A(\lambda)$ is the extinction coefficient of the acceptor at λ, which is typically in units of $M^{-1}cm^{-1}$ (Lakowicz, 2006) (see 2.2.8.2.).

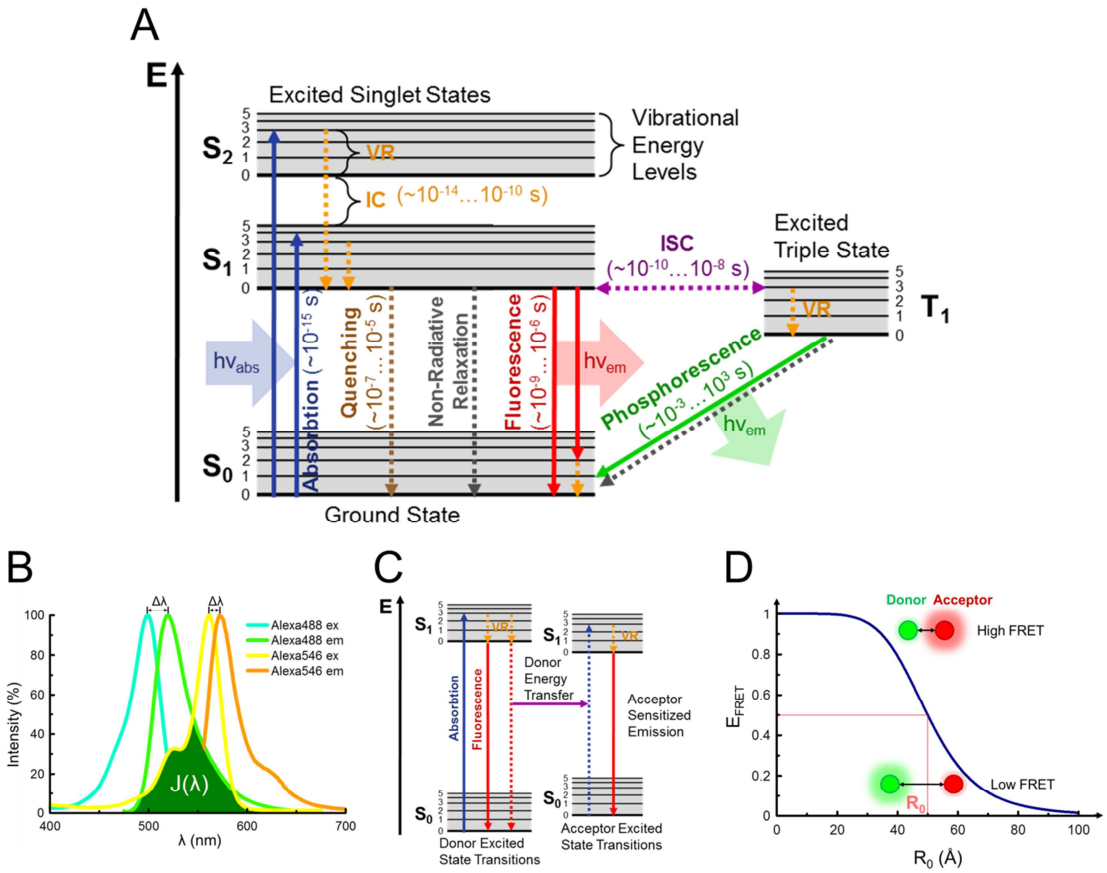

Figure 1. Fluorescence theory. (A) Jablonski diagram. Upon absorption of a photon, fluorophore molecules from the ground singlet state (S_0) are excited to a certain vibrational energy level of higher electronic singlet states (S_1, S_2, etc.). Rapid relaxation to the lowest vibrational level of S_1 singlet state occurs by vibrational relaxation (VR) and internal conversion (IC) processes. From this point competitive processes like Quenching, Non-Radiative Relaxation, Fluorescence or reversible Intersystem Crossing (ISC) may occur. After ISC fluorophore molecule by VR reaches the lowest vibrational energy level of the electronic triplet state T_1 and then phosphorescence occurs ($T_1 \rightarrow S_0$). **(B)** Stokes shifts between Alexa488 excitation (cyan) and emission (green) spectra maximum and between Alexa546 excitation (yellow) and emission (orange) spectra maximum are marked as $\Delta\lambda$. Overlap integral $J(\lambda)$ of Alexa488 (donor) emission spectra and Alexa546 (acceptor) spectra are depicted as a dark green area. **(C)** Jablonski diagram for the FRET process. **(D)** E_{FRET} dependence from R_0 graph reveals linear dependence in the 0.2-0.8 E_{FRET} values interval. Figure 1D is adapted from (Roy et al., 2008).

1.1.3. Fluorophores

Observation of single molecules allows experimenters to detect and quantify subpopulations in a sample and directly observe the dynamic structural changes that macromolecules undergo during various biological processes. Proteins and nucleic acids rarely have efficient natural intrinsic fluorophores, for this reason scientists use extrinsic fluorophores. High quantum yield, high extinction coefficient and photostability are crucial for success of almost all types of fluorescence experiments (Stennett et al., 2014). Another important feature is the fluorophore size, which can be suitable for certain experiment types. There are three types of fluorophores: Quantum dots, fluorescent proteins and organic fluorophores (Figure 2).

1.1.3.1. Quantum Dots

Quantum dots (QDs), the biggest fluorophores, are inorganic nanocrystals that fluoresce at sharp and discrete wavelengths depending on their core size (1-10 nm). QD‘s have high extinction coefficients (10 to 100 times those of fluorescent proteins (see 1.1.3.2.) or small organic fluorophores (see 1.1.3.3)) and have high quantum yields. QDs typically contain a CdSe or CdTe core and ZnS shell (Figure 2A). Their absorbance extends from short wavelengths, up to just below the emission wavelength, so that a single excitation wavelength is able to excite different QDs with different emission maxima. Crucial for biological applications was the development of coatings that make QDs water-soluble, prevent quenching by water, and allow conjugation to protein-targeting molecules such as antibodies and streptavidin (Medintz et al., 2005; Petryayeva et al., 2013; Zhang and Wang, 2012). Due to massive size QDs generally unsuitable for FRET applications (Hohng and Ha, 2005), but long lasting QDs emission is ideal for

particle tracking on the cell surface (Dahan, 2003) or on DNA (Gorman et al., 2007).

1.1.3.2. Fluorescent proteins

Small size (25-30 kDa) of fluorescent proteins (FP) allows their attachment to any protein of interest. The prototypical green fluorescent protein (GFP) consists of 238 amino acids that fold into a rigid 11-sheet β-barrel with a central α-helix (Figure 2B). The fluorescent chromophore 4-(p-hydroxybenzyliden)-5-imidazolinone forms autocatalytically from a tripeptide (Ser65-Tyr66-Gly67 for GFP) (Orm et al., 1996; Tsien, 1998). Single molecule emission detection experiments revealed that GFP are blinking, are involved in triplet or radical states (see 1.1.4.2.), and their emission often fluctuates. To avoid fluctuations, the chromophore must be in planar orientation and rigidly trapped inside the protein (Ha and Tinnefeld, 2012). Discovery of GFP triggered scientists to engineer a set of FPs that span the visible spectrum from deep red to deep blue (Day and Davidson, 2009; Shaner et al., 2005). Due to10-times lower photostability in comparison to small organic fluorophores FPs are unsuitable for particle tracking, but FPs ability to be fused and genetically encoded with almost every protein of interest allows to monitor localization and interaction of proteins inside living cells (Day and Davidson, 2012; Miyawaki, 2011).

1.1.3.3. Organic fluorophores

The smallest known extrinsic fluorophores are organic fluorophores. Proper positioning makes them the least perturbing and the most accurate signal reporters for the single molecule system of investigation. Because organic fluorophores are less stable than quantum dots, a number of chemical modifications and medium developments were discovered that improve the photostability of the dyes, and have markedly expand their applicability almost in every imaging application

thereby advancing our knowledge of molecular structure, dynamics and function (Zheng et al., 2014). According to structure, organic fluorophores are divided in three major categories: rhodamines, carbopyronins/oxazines, and carbocyanines.

1.1.3.3.1. Rhodamines

Rhodamine dyes absorb in the 520-570 nm range, and their photophysical properties depend greatly on the substituents attached to the amino groups and esterification of the carbonyl group in the phenyl ring (Figure 2C). Rhodamines with amino groups alkylated (Rh6G) or integrated into aliphatic rings (Rh101) have quantum yield close to unity. Rhodamines containing non-esterified carbonyl group (TMR and RhB), exhibit a pH-dependent equilibrium between fluorescent cationic form at pH=2 and a higher quantum yield fluorescent zwitterionic form at pH=8. Rhodamines are efficiently quenched by guanosine, tryptophane and are self-quenched when form dimers. Rhodamine derivatives have bulky substituents and sulphate groups to prevent strong interactions and to increase water solubility respectively (Figure 2C). Examples used in sm-fluorescence include Alexa 488, Alexa532, Alexa546, ATTO 532, ATTO 565, ATTO 590, TAMRA (Stennett et al., 2014).

1.1.3.3.2. Carbopyronines and oxazines

Carbopyronines are rhodamines with oxygen replacement by a geminal dimethyl group, it shifts absorption spectrum of dyes to longer waves. Popular red-adsorbing carbopyronin is ATTO 647N (Figure 2D) used as acceptor in sm-fluorescence experiments. Oxazines are a family of red-shifted absorption spectrum compounds, where the central carbon atom of the xantene chromophore is replaced by a nitrogen (Figure 2E). High oxidative potential (high electron affinity) compared to rhodamines or cyanines makes them resistant to oxidation by molecular oxygen, and thereby more resistant to photobleaching (see 1.1.4.1.). In the presence of oxygen-scavenging buffer, oxazines form semi-reduced species,

with fluorescence lasting up to several minutes. They are also prone to redox blinking (see 1.1.4.2.) in the presence of oxidating and reducing agents. Examples of commercial oxazines are ATTO 655, ATTO 680 and ATTO 700 (Stennett et al., 2014).

1.1.3.3.3. Cyanines

Cyanine dyes consist of two nitrogen atoms linked by a conjugated polymethine chain containing an odd number of carbon atoms. Heterocyclic groups are required to stabilize cyanine dyes at both ends. The most popular cyanine dyes like Cy3 and Cy5 have indol groups (Figure 2F). The longer chain in Cy5 is responsible for the redshift in absorption and emission spectra, making it an ideal acceptor in FRET experiments when paired with a Cy3 donor. In contrast to rhodamines, cyanines are not effectively quenched by tryptophan or guanosine due to their lower electron accepting tendency. Instead, stacking interactions between Cy3 and the DNA nucleobases or attachment to protein increases fluorescence and lifetime. At room temperature carbocyanines exist in all *trans* form at the ground state in solution. Upon light absorption competing processes like fluorescence, internal conversion (Figure 1B) and rotation around C-C bond of the polymethine chain occurs. Bond rotation results in a twisted intermediate that deactivates rapidly to the ground state to yield *cis* or *trans* isomers. To prevent formation of poorly fluorescent *cis* isomer, cyanine structure must be rigidized around the polymethine chain like in Cy3B. Reaction of longer polymethine chain's double bond (Cy5) with thiols interrupts the conjugated system and converts the cyanine to a dark state, which can be healed by excitation below 540 nm or by excited Cy3 fluorophore presence closer than the FRET distance. Examples of commercial cyanines are Cy2, Cy3, Cy3B, Cy3.5, Cy5, Cy5.5, Cy7 (Ha and Tinnefeld, 2012; Stennett et al., 2014).

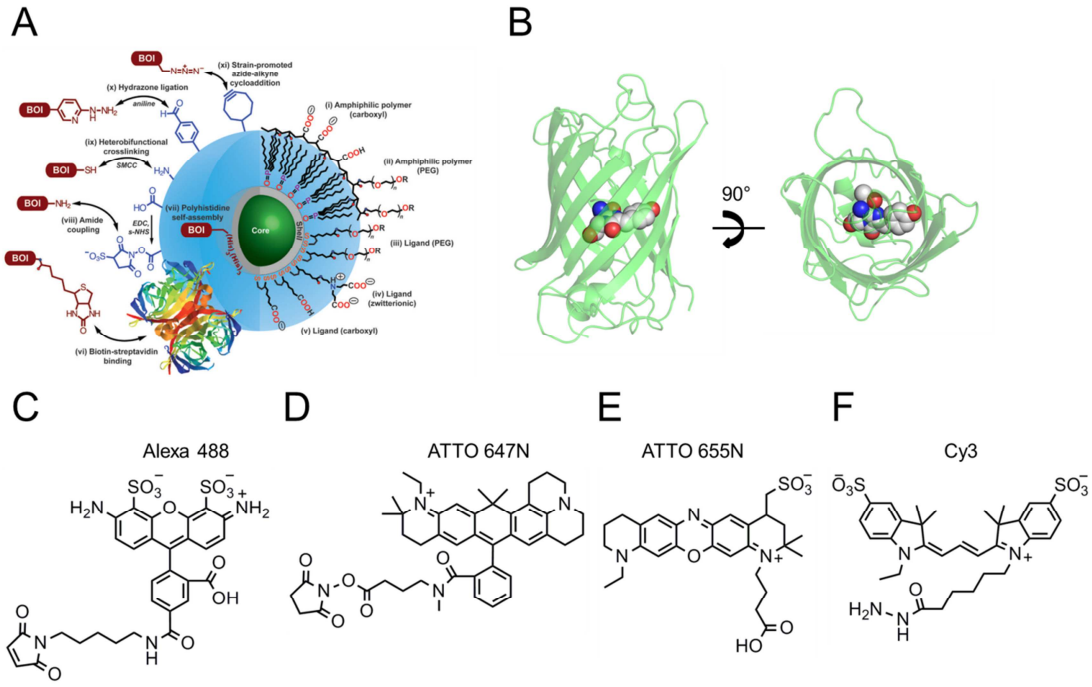

Figure 2. Fluorophores. (A) Quantum Dots consist of core (green), shell (grey) and coatings (cyan) that increase water solubility ((i)-(v)) and allows bioconjugation to biomolecule of interest (BOI) ((vi)-(xi)). Figure 2A adopted from (Petryayeva et al., 2013). **(B)** Structure of *A.victoria* GFP consists of a rigid 11-sheet beta barrel with a helix in the centre (transparent green cartoon) fluorescent chromophore 4-(p-hydroxybenzyliden)-5-imidazolinone (colourful spheres) forms autocatalytically from a tripeptide (Ser65-Tyr66-Gly67) (PDB ID 1EMA). Structural formulas of organic fluorophores with functional groups for specific conjugation: **(C)** Rhodamine Alexa488-C5-maleimide. **(D)** Carbopyronine ATTO647N-NHS esther. **(E)** Oxazine ATTO 655 carboxylic acid. **(F)** Cyanine Cy3-hydrazide.

1.1.4. Improving the characteristics of the fluorophores

Upon appropriate illumination, an ideal fluorophore cycles between the S_0 and S_1 states, resulting in a long-lasting fluorescence. In practice excited fluorophore can return to S_0 state through radiative or non-radiative relaxation pathways (Figure 1B). Excursions to the triplet state attenuate the observed photon emission rate and causes **blinking**. Fluorophores in T_1 triplet state are active in electron transfer reactions that result in formation of the non-fluorescent radical species R^+ and R^-, and subsequent degradation and **bleaching** of the fluorophore

(Gust et al., 2014; Ha and Tinnefeld, 2012; Vogelsang et al., 2008; Zheng et al., 2014).

Two main problems for single-molecule biophysical studies using fluorescence are photobleaching (reactions with oxygen) and undesired intensity fluctuations (blinking caused by intersystem crossing ($S_1 \rightarrow T_1$) or dark states caused by formation of radical ions from the triplet state T_1 (Ha and Tinnefeld, 2012).

1.1.4.1. Bleaching

Oxygen is a good triplex state quencher, although it is also the main participant in fluorophore oxidation. Electron transfer from a triplet state fluorophore to molecular oxygen produces a superoxide radical (O_2^-) and a non-fluorescent cationic state (R^+) of the fluorophore. Energy transfer from a triplet fluorophore to molecular oxygen produces excited singlet oxygen ($^1O_2$), an oxidizing agent stronger than ground state molecular oxygen. Superoxide radicals and singlet oxygen, along with other downstream reactive oxygen species (ROS), including HO・, HO_2・and H_2O_2, can cause photobleaching by directly reacting with the delocalized π-electron system, or phototoxicity by reacting with nearby biomolecules (Zheng et al., 2014). For this reason enzymatic oxygen scavenging systems were developed for imaging experiments. The most popular are the GOD-CAT system (BENESCH and BENESCH, 1953), comprised of glucose, glucose oxidase and catalase, and the PCA-PCD system (Aitken et al., 2008), comprised of protocatechuic acid and protocatechuate-3,4-dioxygenase. Application of these systems for oxygen removal leads to production of organic acids and a decrease in medium pH. For this reason the experimental medium must be well buffered An alternative oxygen removal system is pyranose oxydase in combination with catalase (POC), which produces ketone and has no effect on the pH. Another

oxygen scavenging system is comprised from methylene blue and a thiol (Gust et al., 2014).

1.1.4.2. Blinking

Removal of molecular oxygen from solution reduces fluorophore photobleaching, but accentuates the redox characteristics of the fluorophore's triplet state, which results in severe blinking due to formation of radical states lasting from milliseconds to hours.

The blinking problem can be solved using protective agents. One of the first stabilizing agents was 2-ME, which is still used for stabilization of Q-Dot fluorescence (Schwarz et al., 2013). Most popular protecting agents are 1,3,5,7 cyclooctatetraene (COT), 4-nitrobenzylalcohol (NBA) and 6-hydroxy-2,5,7,8-tetramethylchroman-2-carboxylic acid (TROLOX). The combined use of COT, NBA and Trolox under oxygen scavenging conditions significantly increases the mean fluorescence intensity and duration of photon emission. Protecting agents are more effective if they act as **reducing and oxidizing systems** (ROXS). Systems like ascorbic acid – n-propyl galate, TROLOX/TROLOXquinone (TX/TXQ) and NBA have been shown to function through ROXS mechanisms (Zheng et al., 2014). After intersystem crossing to T_1, the fluorophore can be reduced by the reducing agent yielding the radical anion R^- and then quickly re-oxidized by the oxidizing agent to return to the S_0 (Figure 1A). Alternatively, the fluorophore is oxidized from T_1 by the oxidant to form R^+ and subsequently returns to the ground state by reduction (Vogelsang et al., 2008).

It was demonstrated that the ROXS mechanism using TX/TXQ improves the photostability of Alexa647, ATTO647N or Cy3/Cy5 FRET pair. Photostability of fluorophores with excitation maximum below 600 nm are better improved by **geminal recombination** (GR) mechanism – reduction combined with an efficient back electron transfer by the same single thiol molecule like 2-ME which is

trapped within the solvent cage of fluorescent molecules. GR works perfectly with ROXS (using 2-ME andTX/TXQ) for Alexa488, Alexa532, ATTO532 and Alexa568 (Holzmeister et al., 2014).

COT increases fluorophores brightness by operating through **triplet-triplet energy transfer**. This mechanism is efficient, when triplet energy of the donor fluorophore is higher than the triplet energy of the triplet state quencher (acceptor). In the presence of molecular oxygen, the triplet energy of the quencher should also be lower than the triplet-singlet energy gap of molecular oxygen (~94 kJ/mol) to prevent singlet oxygen generation (Zheng et al., 2014).

Acquired knowledge about fluorescence intensity stabilization mechanism triggered scientists to overcome concentration dependence and chemically attach photostabilizing compounds TROLOX, COT and NBA to organic fluorophore Cy5 linking them with bis-N-hydroxysuccinimide. Obtained Cy5-TROLOX, Cy5-COT and Cy5-NBA **self-healing fluorophores** showed little blinking and reduced photobleaching rates compared to Cy5 (Zheng et al., 2014).

1.1.5. Labelling of biomolecules

Fluorophores used for single-molecule FRET experiments have to match several chemical and photophysical requirements: 1) to ensure labelling stoichiometry for object tracking and 2) to ensure biomolecule labelling efficiency and specificity for sm FRET measurements.

1.1.5.1. Nucleic acids labelling

Four main strategies for fluorescent label incorporation into nucleic acids are known: 1) terminal or internal nucleotide modifications, which allows attachment of fluorophore derivative; 2) addition of intercalating fluorophore, which binds to nucleic acids by stacking interactions; 3) nucleotide modification with a ligand molecule, which subsequently is recognized by fluorescently

labelled protein; 4) addition of nucleic acids binding fluorescent protein (Kricka and Fortina, 2009).

1.1.5.2. Protein labelling

There are three major chemical derivatives of fluorophores: a) maleimides that react with thiols, b) N-hydroxysuccinimide esters that react with primary amines, and c) fluorophores modified with hydrazine that react with ketone groups in genetically encoded unnatural amino acids (Roy et al., 2008).

Protein modification requires mild procedures to prevent chemical or thermal denaturation. Despite sufficient fluorophores reactivity in physiological conditions, labelling with **maleimides** (Figure 2C) at specific cysteines for FRET experiments requires introduction of cysteine in the proper position and substitution of other undesired cysteines to prevent unspecific labelling. It is also very important to correctly choose labelling position and to prevent disruption of protein structure upon fluorophore's reactions with the desired amino acid (Toseland, 2013).

The labelling position and stoichiometry is not very important if purpose of the experiment is protein tracking, in this case **N-hydroxysuccinimide** (Figure 2D) fluorophore could be used for labelling of side chains of protein surface lysines (Toseland, 2013).

Labelling with **hydrazine** (Figure 2F) fluorophores does not yet have wide application, since it requires genetically encoded unnatural amino acids (Kim et al., 2013a), and even proteins with ketone groups are labelled poorly (Ryu and Schultz, 2006).

Analysis of protein dynamics and conformational changes using sm FRET is widely used to characterise protein structure and function. Nonetheless, site-specific double labelling is still a challenge. Traditional labelling with two fluorophores performing sequential labelling reactions with an intermediate

chromatographic purification (Dikić, 2009), or labelling with a mixture of fluorophores and selection of double labelled proteins during the sm experiment provides double-labelled protein, but label positions in this case are random (Comstock et al., 2015; Theissen et al., 2008; Zhao et al., 2011). Some authors suggest site-specific double-labelled protein by encoding unique unnatural amino acids and then label them with hydrazine-Cy3 and azide-Cy5. This method was used to test the conformational changes in calmodulin (Kim et al., 2013b).

1.1.6. Experimental setups for fluorescence based single-molecule measurements

The major condition for sm fluorescence detection is high signal-to-noise ratio. There are two techniques used for sm fluorescence imaging: i) fluorescence confocal microscopy and ii) total internal reflection fluorescence (TIRF).

1.1.6.1. Confocal microscopy

In confocal microscopy a laser beam is focused by a high NA microscope objective to a diffraction-limited volume of ~1 femtoliter (Figure 3A). Both the excitation and emission light is collected through the same objective ("epi-fluorescence"). A micrometer-sized pinhole positioned in the emission light path filters out-of-focus light. Diffraction-limited volume, caused by high-NA objective enhances the signal-to-noise ratio and allows the collection of a greater number of photons by avalanche photodiodes (Tian et al., 2011). Investigation of single fluorescently labelled molecule that occupies the confocal spot are possible if concentrations used are in the picomolar range. The transit of a fluorescently-labelled molecule diffusing through the confocal volume can be detected as a photon "burst". Low concentrations in these experiments are necessary because relative intensity fluctuations are reciprocal to number of molecules at the confocal volume. Autocorrelation function calculated from time trajectories of the

fluorescent signal allows to extract information about protein diffusion, stoichiometry and FRET efficiency applying fluorescence correlation spectroscopy (FCS) (Rigler and Elson, 2001) or fluorescence cross-correlation spectroscopy (FCCS) (Bacia and Schwille, 2007) methods respectively. Data can also be collected from immobilized molecules if a scanning stage is integrated (Gust et al., 2014).

1.1.6.2. TIRF microscopy

Total internal reflection fluorescence microscopy (TIRFM) is a method based on the physical property of the evanescence wave. Evanescent wave is generated when a light beam propagating through a transparent medium of a higher refraction index n_2 (e.g. a solid glass prism) encounters an interface with a medium of a lower index of refraction n_1 (e.g. sample solution), it undergoes total internal reflection for incidence angles (measured from the normal to the interface) greater than the critical angle θ_C (eq. (7)):

$$\theta_C = \sin^{-1}\left(\frac{n_2}{n_1}\right) \quad (7)$$

Although the incident light beam totally internally reflects at the interface, an electromagnetic field called the evanescent wave penetrates a small distance into the liquid medium and propagates parallel to the surface in the plane of incidence. The evanescent electric field intensity *I(z)* decays exponentially with perpendicular distance *z* from the interface (eq. (8)) (Figure 3B):

$$I(z) = I_0 e^{-\frac{z}{d}} \quad (8)$$

$$d = \frac{\lambda_0}{4\pi}[n_1^2 \sin^2\theta - n_2^2]^{-\frac{1}{2}} \quad (9)$$

where *d* (eq. (9)) is a characteristic penetration depth at which intensity of evanescent wave electric field decreases by *e*, λ_0 – light wavelength in vacuum

and θ is angle of incidence (Axelrod, 2001, 2003; Axelrod et al., 1984; Fish, 2009).

TIRF can be generated by either coupling the laser beam through the extreme edge of a high-NA objective ("objective TIRF") or by coupling it into a prism above the microscope coverslip ("prism TIRF") to achieve the angle for total internal reflection (Figure 3B). At the interface of two phases, evanescent wave penetrates into the sample only 100-200 nm. Only fluorophores situated in the evanescent field are excited, thus giving us high signal-to-noise ratio (Gust et al., 2014; Roy et al., 2008).

For FRET measurements the emission signal collected from the observation volume is separated into donor and acceptor channels. This is achieved by a dichroic mirror, optical filters and separate detectors to monitor the photon count for the two channels simultaneously (Figure 3B). FRET experiments could be performed by constantly exciting the donor fluorophore (Roy et al., 2008) or by using advanced excitation schemes called 'alternating-laser excitation' (ALEX) (Hohlbein et al., 2014; Lee et al., 2005) or 'pulsed interleaved excitation' (PIE) (Hendrix and Lamb, 2013; Müller et al., 2005), where the donor and acceptor excitation lasers alternate in order to separately excite the donor and acceptor molecules. Molecule sorting for donor- and acceptor-labelled species via alternating laser excitation (ALEX) are possible for confocal fluorescence spectroscopy method in solution and the TIRF setup (Gust et al., 2014).

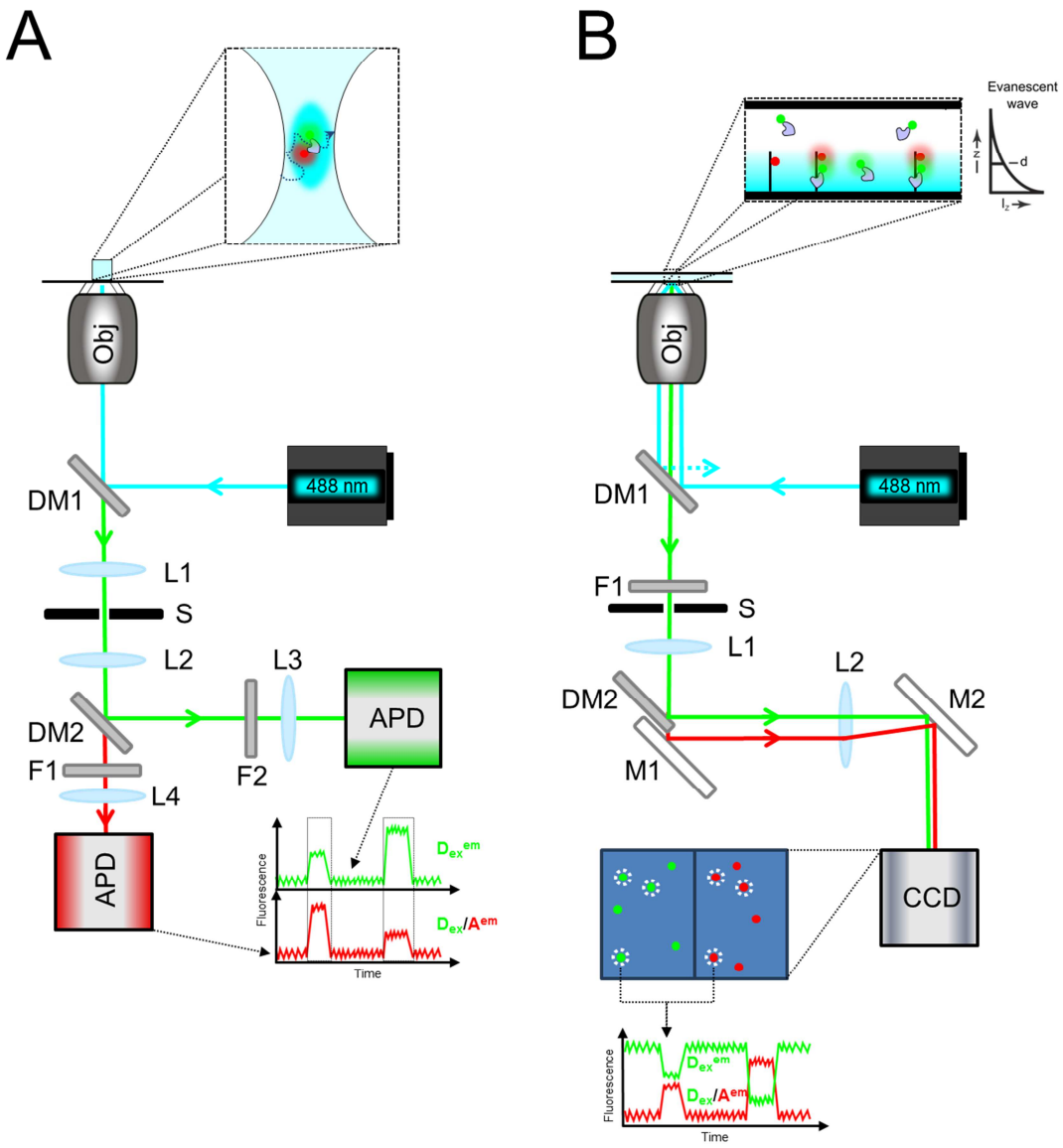

Figure 3. *See next page.*

Figure 3. FCS and TIRF FRET setups. (A) In the FCS (fluorescence correlation spectroscopy) setup fluorescent molecules are freely diffusing through the confocal volume (vivid cyan elipse, inset) of the focused 488 nm parallel laser beam (cyan), excited fluorescent donor transfers energy to fluorescent acceptor. Both signals travel through a sophisticated optical system, it is splited by dichroic mirror (DM2) (green line – donor signal, red line – acceptor signal) and separately detected by avalanche photodiodes (APDs). Recorded donor and acceptor intensity data allow to determine the diffusion time of fluorescent molecules through the confocal volume and FRET efficiency from correlated signals. Size of the confocal volume (1 femtoliter) and specificity of excitation enable excitation of single molecules and detection of the signal with high signal-to-noise ratio. Figure adopted from (Gust et al., 2014). **(B)** FRET experiments with TIRF (total internal reflection fluorescence) setup are performed by immobilizing on the glass surface DNA oligonucleotide labelled with fluorescent acceptor within R_0 distance from the specific site (see 1.1.2.) (black stick with red circle, inset) and applying fluorescent donor-labelled protein (blue shape with green dot, inset) to the experimental cell. High NA (numerical aperture) objective (Obj) directs 488 nm laser light to the flow cell in total internal reflection (TIR) manner. The intensity of the evanescent wave (gradient cyan rectangle) drops exponentially (evanescent wave intensity (I_z) from penetration depth (z) graph depicted near inset), therefore it excites donor fluorophores that are close to the surface (up to 200 nm). The DNA-bound site-specific protein transfers energy from an excited donor to an acceptor. The donor and acceptor emission signals are splited by a dichroic mirror (DM2) and imaged side by side on a charge-coupled device (CCD) camera. Only signals that overlap in donor and acceptor emmision chanels (red and green dots with white dotted rings) are analysed. The lower graph depicts donor and acceptor anticorrelating intensities during FRET between a donor-labelled protein and an acceptor-labelled DNA. Excitation with evanescent wave avoids donor excitation, resulting in high signal-to-noise ratio. Figure adapted from (Roy et al., 2008). F – filter, S – slit, L – lens, M – mirror.

1.1.7. FRET techniques

1.1.7.1. Single-color FRET

In this technique FRET efficiency is determined from the fluorescence intensity of the donor. Fluorescent donor Alexa-546 and a non-fluorescent Dabsyl acceptor were selected to measure conformational changes of human apoptosis protein Bax, which exists in cytosol and translocates to the mitochondria outer membrane upon induction of apoptosis. Internal label Alexa-633 was introduced for normalization of donor intensity from fluorescence intensity fluctuations in different environments (Gahl et al., 2014).

1.1.7.2. PIFE

Protein induced fluorescence enhancement (PIFE) is the method based on the phenomenon whereby the intensity of a fluorophore increases upon proximal binding of a protein. This method can detect single base-pair steps in the extreme vicinity of the fluorophore. This method does not require protein labelling and is extremely sensitive to the distance changes in the range of 0-4 nm. This makes it a good complement to FRET (Hwang et al., 2011).

1.1.7.3. 2-color FRET (fluorophore-fluorophore, fluorophore-QD, QD-QD)

2-color FRET between two fluorophores is a classical and the most common FRET technique, commonly used for the studies of protein conformational changes and protein-ligand interactions. The basic theory explaining the Förster resonance energy transfer phenomenon is also based on the fluorescent donor and acceptor interaction (Figure 1A) (see 1.1.2.) (Lakowicz, 2006; Roy et al., 2008).

Alternative 2-color quantum dot-fluorophore FRET technique was used for measuring FRET between quantum dot (QD) and attached Alexa594-labelled duplex (Zhou et al., 2005). FRET was also measured between a QD QS585 and an acceptor Cy5 on the Holliday junction. Analysed low- and high-FRET dwell times were almost identical to those obtained from the same experiment with the Cy3/Cy5 fluorophores. Narrow emission spectra of the QD (see 1.1.3.1) decreases the overlap integral $J(\lambda)$, but it is compensated by higher quantum efficiency of the QD (eq. (6)). Reduction of direct excitation prolongs Cy5 lifetime, and high QD brightness allows to detect signal with higher signal-to-noise ratio. Major drawback of QD is its size (~20 nm), which is comparable to the size of the protein, making it useless for the investigation of protein conformational changes;

even Holliday junction FRET detection was sensitive to the streptavidin layer thickness on the QD (Hohng and Ha, 2005).

FRET experiments employing donor and acceptor QDs are attractive due to QD brightness and photostability, making them promising candidates for device-on-chip applications and for various sensors designed for an outside-laboratory applications (Chou and Dennis, 2015).

1.1.7.4. 3- and 4-color FRET

3-color FRET technique was employed to monitor dynamics in single molecules between three points of interest. More sophisticated setup and complex data analysis are necessary to extract signals from three possible FRET pairs. (Figure 4A). A 3-color FRET experiment was performed with Holliday junction with one end attached to the glass surface and three ends labelled with Cy3, Cy5 and Cy5.5 fluorophores. During Cy3 excitation anticorrelated Cy5 and Cy5.5 intensity fluctuations consistent with two Holliday junction conformations, where the Cy3 end is closer either to the Cy5 or to the Cy5.5 labelled ends. FRET efficiencies between Cy3 and Cy5 (E_{12}) were calculated from events with Cy5.5 in the dark state, after reactivation FRET efficiency between Cy3 and Cy5.5 (E_{13}) was calculated from events with bleached Cy5, FRET between Cy5 and Cy5.5 was calculated between states with active and inactive Cy5.5 (Hohng et al., 2004). Alternatively, FRET between Cy5 and Cy5.5 could be evaluated by exciting Cy5 with a 633 nm laser (Figure 4A). The same scheme was applied for RNA polymerase (RNAP) translocation experiment on terminally double-labelled DNA fragment.. Experiments confirmed downstream translocation of RNAP (Lee et al., 2007).

The 4-color FRET technique (Figure 4B) was tested in a confocal microscopy setup (see 1.1.6.1) on the Holliday junction with all four ends labelled with Cy2, Cy3, Cy5 and Cy7. All possible six FRET efficiencies were obtained by

exciting fluorophores in succession of three lasers (633 nm, 532 nm and 488 nm). Using this setup, immobilized, partially ds DNA with Cy5 (at ss and ds DNA junction) and Cy7 (at the terminal part of ss DNA) labels was preassembled with RecA protein; subsequently a homologous DNA duplex with terminal labels Alexa488 and Cy3 on the strand complementary to the ss part of immobilized DNA was injected. Two strong different FRET signals were detected from Alexa488-Cy5 and Cy3-Cy7 fluorophore pairs upon strand exchange (DeRocco et al., 2010; Lee et al., 2010).

Multi-color FRET approaches that monitor multiple distances are technically challenging. To reduce technical and analytical complexity and to enable multiple distance monitoring, **switchable FRET** that sequentially probes FRET between single donor and switchable acceptors is used. Switchable acceptors can be turned into dark state in the absence of oxygen and presence of thiols and reactivated with laser excitation below 540 nm (Cy5, see 1.1.3.3.3) or may switch reversibly in the presence of reducing agent and molecular oxygen (ATTO655) (Uphoff et al., 2010).

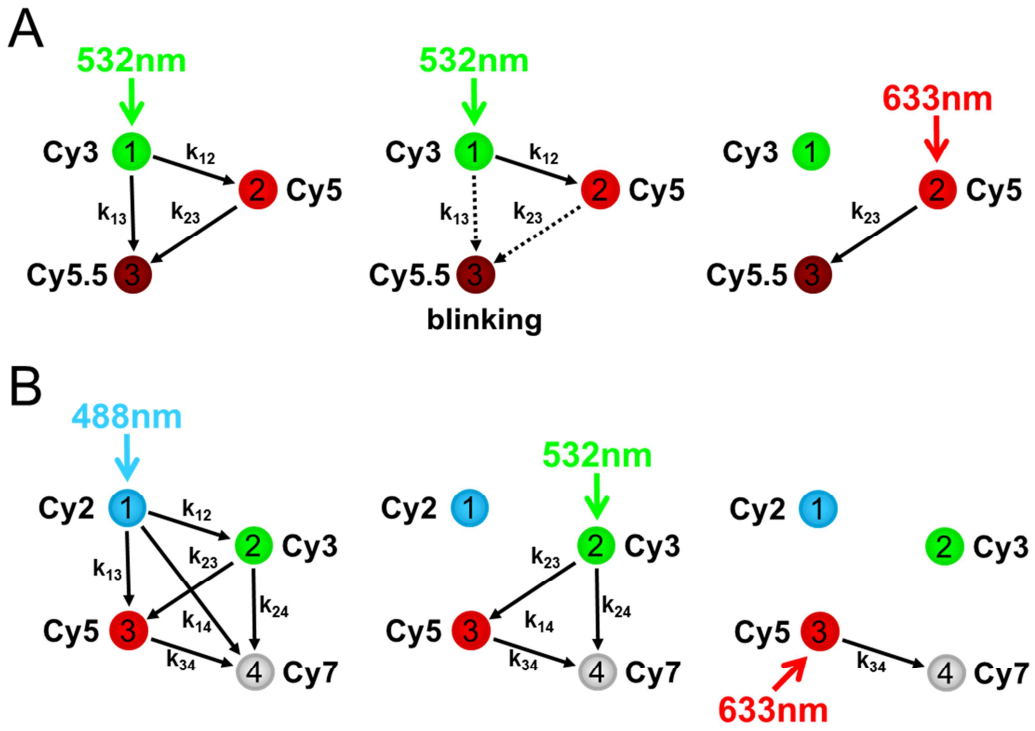

Figure 4. Multi-color FRET techniques. (A) 3-color FRET. 3 FRET pairs are possible between 3 compatible fuorophores (J(λ), see 1.1.2., Figure 1B). FRET values between all FRET pairs could be determined by exciting a certain donor fluorophore with a laser of specific wavelength (Cy3 with 532 nm, Cy5 with 633 nm) or by continuously exciting the highest energy donor (Cy3) and using one blinking acceptor (Cy5.5). **(B)** 4-color FRET. 6 FRET pairs are possible between 4 compatible fuorophores (J(λ), see 1.1.2., Figure 1B). FRET values between all FRET pairs could be determined by in turn exciting different fluorophores with lasers of specific wavelength (488 nm, 532 nm and 633 nm).

1.1.8. FRET applications in the studies of large molecular machines

The FRET-based methods were applied in the studies of complex molecular machines. Ribosome is the protein synthesis machine that exists in every living cell. In prokaryotes it is comprised of two 30S and 50S subunits, which upon assembly form the 70S ribosome. FRET measurements were performed between 13 FRET pairs on different positions of the head, tail and platform domains of the 30S subunit in the free state or complexed with the 50S

subunit. Obtained data were used as distance constraints for structure modelling. Obtained models revealed that upon formation of the 70S ribosome, the head of the 30S subunit tilts towards the subunit interface, and the platform rotates in a clockwise fashion (Hickerson et al., 2005). FRET experiments with Cy3-Met-tRNA^{fMet}, Cy5-Phe-tRNA^{Phe} and a mutated ribosome (rRNA G2252C, which disrupts a contact with tRNA C74) helped to detect the hybrid state 2, where one tRNA stays in aminoacyl (A) site and the other tumbles between the peptidyl (P) and exit (E) sites (Munro et al., 2007). 3-color FRET experiments were performed to define 16S rRNA conformation changes upon association with one of the first ribosomal proteins S4, which defines the protein assembly hierarchy during formation of 30S ribosomal subunit (Kim et al., 2014).

Spliceosome is another object for sm experiments with FRET. Fluorescent labels were incorporated into pre-mRNA or on spliceosome proteins and mRNA formation or arrival of spliceosome proteins on pre-mRNA was analysed (Hoskins et al., 2011). Fluorescently double-labelled unfolded protein VHL was examined with a GroEL/ES chaperone. After VHF incubation with GroEL, compaction between all examined labels was detected, after addition of GroES and ATP, even higher FRET values were detected between the hydrophobic regions, and lower FRET values between N- and C-terminal regions of the VHL (Kim et al., 2010). Single molecule examination of F_0F_1-ATP synthase with fluorophores on F_0 static subunit and fluorophores on the rotating subunit ε and c, helped detect elastic deformation within the ε and c subunits of the rotor (Ernst et al., 2012).

FRET method was also applied to investigate various channels and transporters. Luminescent resonance energy transfer (LRET) method that uses lanthanide donor complex and conventional acceptor, was applied to detect distance change on S4 transmembrane segment on voltage-sensitive domain of voltage gated potassium channel as a result of scorpion toxin binding (Posson et al., 2005). Neurotransmitter sodium symporter (NSS) removes the

neurotransmitter from the synapse in the reuptake process. Conformational changes (modulation of intracellular gating) at the single molecule level were investigated for prokaryotic NSS homologue LeuT by changing substrates, inhibitors or introducing mutations that alter binding, transmission or both (Zhao et al., 2011). FRET experiments revealed that 3 subunits of the trimeric sodium-coupled aspartate transporter changes conformation asynchronously when transports aspartate and 3 Na^+ ions (Erkens et al., 2013). Single molecule patch-clamp FRET microscopy study on the N-methyl-D-aspartate (NMDA) receptor revealed that the ion channel electric "off" state is associated with multiple conformational states, and the "on" state is associated with a narrower distribution of conformational states (Sasmal and Lu, 2014).

Among other popular objects analysed with FRET-based methods were LacY, tested for a conformational change upon binding of a galactopyranoside (Majumdar et al., 2007), and kinesin, which under saturating concentration of ATP spends most of the time bound to the microtubule with both heads (Mori et al., 2007). Multiple conformational dynamics of the N-terminal domain (NTD) of the p53 were investigated in isolation and in the context of tetrameric full-length p53 (Huang et al., 2009).

An elegant sm FRET study performed on RNA polymerase (RNAP) revealed that abortive initiation of transcription initiation complex proceeds through a "scrunching" mechanism, in which polymerase remains fixed on a DNA promoter and pulls DNA downstream into itself. By placing fluorophores on different parts of polymerase and on DNA, experimenters were able to exclude all the other possible abortive initiation mechanisms (Kapanidis et al., 2006). FRET experiments also revealed that the HIV reverse transcriptase (RT) slides on the DNA/RNA hybrid and flips to polymerisation orientation upon arrival to the terminal end of the primer. DNA- and RNA-dependent DNA synthesis was detected as a gradual increase in FRET efficiency (Liu et al., 2008). FRET

experiments with DEAD Box Helicase YxiN (which consumes ATP and unwinds RNA) revealed that the closed conformation of the RecA-like domain could be “opened“ by simultaneous binding of RNA and ATP, and helicase maintains closed conformation during ATP hydrolysis. Additional kinetic experiment revealed that YxiN binds ATP in the presence of RNA with higher affinity and suggests that RNA unwinding begins upon the closure of helicase domains (Aregger and Klostermeier, 2009; Theissen et al., 2008). Negative supercoiling reaction performed by gyrase was studied by following multiple distance changes on different gyrase subunits (Gubaev et al., 2009; Lanz and Klostermeier, 2011). FRET experiments also revealed that DNA polymerase I (Klenow fragment) exists in two conformations – “open“ and “closed“. Upon binding to the DNA template, polymerase is always in an “open“ conformation, and upon formation of the ternary complex with the correct dNTP, it adopts the fully closed conformation. Partially closed conformation was detected with incorrect dNTPs and with all dNTP in polymerase variants with mutated conserved fidelity control positions E710 and Y766 (Hohlbein et al., 2013).

The monomeric UvrD helicase translocates ss DNA. Experiments with optical tweezers and a confocal microscope allowed to detect a change in the DNA construct length and protein conformation. Investigation of the dimeric UvrD helicase revealed that in the open conformation, the helicase unwinds DNA and re-anneals DNA (Comstock et al., 2015). Investigation of MutHLS mismatch-repair (MMR) system employing FRET revealed that MutS adopts multiple conformations when it is in the free state or while it is scanning mismatch-free DNA, but MutS adopts a single defined conformation upon recognition of a mismatch. Additional experiments revealed that MutL traps MutS at a mismatch before MutS undergoes a conformational change to the mobile state (Qiu et al., 2012, 2015).

1.2. Single molecule force spectroscopy

Since the elucidation of the DNA structure, it has become increasingly clear that many fundamental biological processes, such as DNA replication or DNA transcription depend on the unwinding or melting of the DNA sequences. These processes are controlled by enzymes that convert chemical energy into mechanical force (Strick et al., 2003). One of the possible ways to investigate the biological functions of DNA, RNA and proteins, and various aspects of their mechanical behaviour, is to apply external force to the molecule of choice. Optical and magnetic tweezers are the most common single-molecule force-applying techniques used as stand-alone experimental setups or in combination with fluorescence-based single-molecule techniques. The basic principle of the force spectroscopy is to control the molecules of interest using various external forces (Ha, 2014; Neuman and Nagy, 2008).

1.2.1. Single molecule force spectroscopy techniques

1.2.1.1. Optical tweezers

Optical tweezers enabling trapping and manipulation of small beads. The optical trap is created by focusing the laser to a diffraction limited spot with a high numerical aperture (NA) microscope objective. Dielectric particle in the vicinity of the focus experiences a restoring force directed towards the focus. Induced dipole of the polarized particle by optical field interacts with the steep gradient of the optical field near the focus of the laser, which results in a force along the gradient. Along the beam direction propogates scattering force which shifts the trap position slightly off the focus. Stable trap is achieved with very high NA, when force created by the steep gradient overcomes the scattering force. In the range of small displacements of the trapped object, displacement is proportional to

the gradient force, and the optical trap acts as linear spring (Figure 5A) (Heller et al., 2014; Neuman and Nagy, 2008). Optical tweezers can be used in the setups with static or dynamic configurations (position-clamp, force-clamp, dynamic force spectroscopy) (Capitanio and Pavone, 2013).

Using the dumbbell assay, where bead-attached DNA end is trapped with strong gradient and the RNA transcribing polymerase attached to the bead, trapped to weak gradient which allows to keep constant force, individual base-pair steps of RNA polymerase translocation was observed (Sierra et al., 2015), and torque produced by RNAP before stalling was measured (Ma et al., 2013). An elegant study was performed using optical tweezers and a micropipette to investigate the process of dsDNA packaging into φ29 capsid by the multimeric ring-shaped motor proteins. The study revealed the coupling between ATP hydrolysis and DNA bp packing (9 or 10 bp/5 ATP for each packaging cycle), the packaging rate and the dependence of packaging rotation per base pair on the capsid fill level. It was also calculated that the pressure inside the capsid reaches ~20 atmospheres upon completion of viral DNA packaging (Liu et al., 2014).

1.2.1.2. Magnetic tweezers

Magnetic tweezers are the most straightforward, non-damaging single molecule force technique that allows high-throughput experiments (De Vlaminck and Dekker, 2012; De Vlaminck et al., 2011). The basic magnetic tweezers consist of two permanent magnets placed above a sample holder of an inverted microscope (Figure 5B) connected to a CCD camera and a frame grabber. The main principle of the magnetic tweezers is that magnetic particles experience force proportional to the gradient of the square of the magnetic field. Steep gradients of magnetic fields can be created with small permanent magnets or electromagnets. For single molecule experiments neodymium iron boron ($Nd_2Fe_{14}B$) magnets are usually used because they have the strongest permanent

magnetic field. One end of single DNA or protein molecules is typically attached to the surface of the flow-cell and the other end is bound to a super-paramagnetic bead. Super-paramagnetic beads consist of 10-20 nm magnetic particles covered with a porous matrix, and is protected with a polymer layer. On the surface of this layer specific chemicals or proteins can be attached enabling attachment of the investigated molecule. In the absence of magnetic field, beads have no residual magnetization, which prevents aggregation. Application of the magnetic field to the super-paramagnetic beads aligns magnetic domains with the magnetic field (Neuman and Nagy, 2008).This feature allows not only pull molecules, but also to rotate the (Strick et al., 1996). In addition to pulling and rotation, more complex setups allow to stretch molecules in parallel to the surface and to observe diffusion of single molecules (Schwarz et al., 2013).

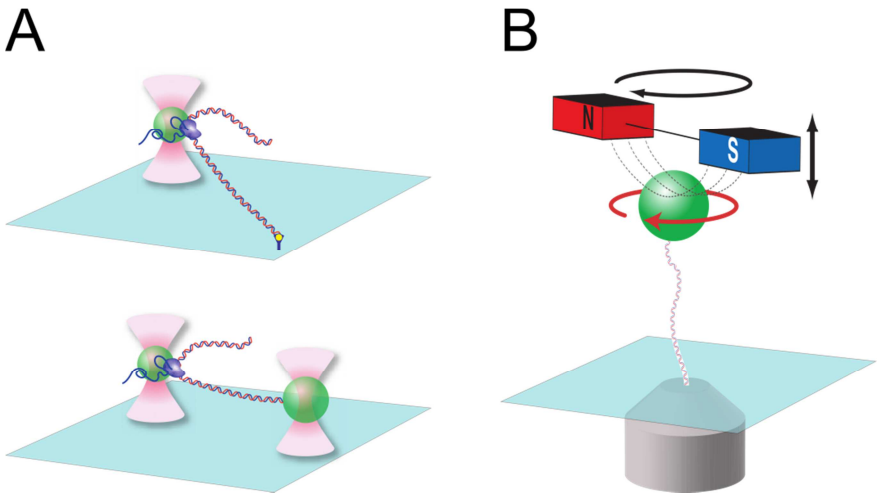

Figure 5. Optical and magnetic tweezers. (A) Optical tweezers. In tethered assay RNA polymerase (purple) is attached to an optically trapped bead (green) and the free DNA end is attached to the surface of the flow-cell. During transcription by RNA polymerase, the bead is pulled from the optical trap, but the moving stage compensates the bead position in the optical trap. In this way, position of the bead at a constant force is recorded (upper panel). The dumbbell assay is similar to the tethered assay, but the free end of the DNA is attached to the second optically trapped bead. The force on the bead is kept constant by moving one of the traps (lower panel). **(B)** Magnetic tweezers. The DNA molecule is attached to the surface and the super-paramagnetic bead (green). Two permanent magnets (red and blue) create a magnetic field gradient along the axial direction, which results in a force directed towards the magnets. The bead stretching force is controlled by moving the magnets in the axial direction (black arrow). Rotation of the magnets (black circular arrow) produces rotation of the super-paramagnetic bead with DNA in one-to-one correspondence (red circular arrow). Figure adopted from (Neuman and Nagy, 2008).

1.2.2. Experiments with magnetic tweezers

Linear shape of DNA, RNA and some proteins is perfectly suited for their investigation in the magnetic tweezers setup. One end of the molecule must be attached to the surface of the experimental cell, and another end bound to a magnetic bead. Applied forces to the single molecules are high enough to induce structural deformations and to investigate the behaviour of single molecules at different forces. Several control experiments must be performed to define the type

of the molecule, length of the molecule and to calibrate the magnets (Manosas et al., 2010; Strick et al., 2001, 2003; De Vlaminck and Dekker, 2012).

1.2.2.1. Magnetic tweezers calibration

The DNA molecule attached between the surface and the magnetic bead is stretched by applying a constant magnetic force. A look-up table of images of the bead, which links the vertical position of the bead and its diffraction pattern is then created. During the actual experiments, the diffraction patterns of the bead are compared to look-up table and the position of the magnetic bead (corresponding to DNA length) is detected in real time (Huhle et al., 2015a; Otto et al., 2010). The force acting on the DNA molecule is obtained by power-spectral density analysis of the magnetic bead fluctuations perpendicular to the force direction (or in parallel direction to the flow-cell surface) (Daldrop et al., 2015). Obtained parameters allow to fit the worm-like chain (WLC) model and calculate the persistence length, the measure that describes the elasticity of the polymer chain (Bouchiat et al., 1999; Strick et al., 2003).

1.2.2.2. Magnetic tweezers application

Since its invention, magnetic tweezers were used to investigate various mechanical properties of nucleic acids, including stretching (Smith et al., 1992), rotation of stretched DNA for torque measurements, DNA buckling, DNA supercoiling at low stretching forces, and DNA denaturation at high stretching forces (P-DNA) (Allemand et al., 1998; Strick et al., 2003). This technique has even wider applications in the studies of DNA-acting proteins.

Type I restriction-modification (R-M) enzymes perform DNA modification and cleavage. The protein is comprised of one recognition subunit (HsdS), two methyltransferase (MTase) subunits (HsdM) and two translocation-restriction endonuclease subunits (HsdR). Upon cognate DNA binding, the HsdR subunits

start DNA translocation in opposite directions in ATP-dependent manner, and hydrolyses DNA upon collision with another DNA-bound protein. During translocation two DNA loops are formed, resulting in DNA shortening, which can be readily detected using magnetic tweezers. Experiments with EcoR124I allowed to determine the translocation rate of the complex, its processivity, the dependence of the translocation rate on force and ATP concentration, also revealed that two HsdR subunits work independently and follow a helical pitch of the DNA (Seidel et al., 2004). Experiments also demonstrated that DNA translocation is initiated when the HsdS/HsdM subunits load HsdR subunits onto adjacent DNA and stops upon HsdR dissociation (Seidel et al., 2005). Phosphate detection and triplex displacement assays were employed to calculate ATP consumption and translocation rate dependency on ATP concentrations. It was shown that the complex on average uses ~1.26 ATP molecules per 1 bp of translocated DNA. Translocation step size of 1 bp was extracted from the translocation noise by Fourier analysis (Seidel et al., 2008).

Experiments employing magnetic tweezers also revealed that upon promoter binding, RNA polymerase unwinds DNA approximately by one turn (Revyakin et al., 2004), thereby forming an open RNAP-DNA complex. The subsequent transcription initiation complex repetitively pulls and releases DNA into RNAP without polymerase translocation and synthesizes 9-11 bp abortive RNA molecules. This mechanism (“scrunching“) was discovered in parallel using two different single-molecule techniques – magnetic tweezers (Revyakin et al., 2006) and confocal microscope with ALEX (Kapanidis et al., 2006) (see 1.3.8.).

RecA is prokaryotic protein that mediates homologous recombination. It assembles into a filament along one DNA strand and catalyses stand exchange with another dsDNA. The strand rearrangement, which is central to homologous recombination, was examined with magnetic tweezers. It was demonstrated that a change in writhe (ΔW) of supercoiled molecule correlates with the length of

invaded RecA-ssDNA fragment (van der Heijden et al., 2008). Experiments with magnetic tweezers also revealed that in the presence of ATP and Mg^{2+} the eukaryotic RecA homologue Rad51 binds the dsDNA in two interchangeable patterns on unwound DNA (18.6 bp/turn) and on native DNA. Changing DNA twist of Rad51-dsDNA complex from 10.5 bp/turn to 18.6 bp/turn increases DNA length 1.5 times, in contrast free DNA hardly increases its length at the same unwinding helicity. In the presence of ATP and Ca^{2+}, Rad51-dsDNA locks irreversibly upon DNA unwinding to 18.6 bp/turn in the increased length state (Atwell et al., 2012). Using magnetic tweezers, bending persistence length (Lp) and torsional persistence length (C) values were determined for Rad51-dsDNA and Rad51-dsDNA filaments, which revealed that complexes are much stiffer than free dsDNA (Lee et al., 2013).

Magnetic tweezers also helped to investigate nucleosome assembly, when nucleosome assembly protein 1 (NAP-1) and core histones were applied on dsDNA and complete nucleosome formation was revealed by detecting change in linking number (ΔL_k is externally applied rotation by magnets that equals to DNA rotations introduced by nucleosome formation and supercoils formed on free DNA). Experiments revealed that each assembled nucleosome shortens DNA molecule by 56 nm (Vlijm et al., 2012). Experiments revealed that the tetrasome of H3-H4 histones wraps DNA in a left-handed or right-handed fashion, but addition of H2A/H2B stabilizes the left-handed nucleosome (Vlijm et al., 2015).

Magnetic tweezers are used extensively to investigate objects like helicases (Hodeib et al., 2016; Kemmerich et al., 2016), gyrases (Basu et al., 2016), F1-ATPase (Watanabe and Noji, 2015; Watanabe et al., 2010), Holliday junction (Dawid et al., 2004), UvrABC repair system (Fan et al., 2016) or on Tn5 system (Adams et al., 2007), prooves that single molecule magnetic tweezers are on high demand.

1.3. Facilitated diffusion of proteins on DNA

Recognition and binding of specific sites on DNA by proteins is central for many cellular functions, such as transcription, replication and recombination. During the search for the target site, the site-specific DNA binding proteins are facing two types of challenges: (i) thermodynamic, i.e. recognition and tight binding of the specific site in the presence of the billions of non-specific DNA sequences and (ii) kinetic, i. e. rapid location of the specific site in the crowded cellular environment that is filled with nonspeicific DNA and proteins (Tafvizi et al., 2011a).

1.3.1. Diffusion-limited reaction rate

A typical macromolecule is usualy 10-100 kDa in size and has a diameter of about 5 nm. Assuming that protein travels through the solution by Brownian motion its trajectory can be described as a random walk (Berg, 1993). The major feature of Brownian motion is that the average of the distance squared covered by a diffusing particle grows linearly with time (eq. (10)):

$$x^2 = 2nDt \quad (10)$$

where x is distance covered by the diffusing particle from the starting point, n – number of dimensions of diffusion environment, D – diffusion constant, t – time.

The value of diffusion constant can be calculated from the Stokes-Einstein relation for spherical particles (eq. (11)):

$$D = \frac{k_B T}{6\pi\eta r} \quad (11)$$

where η is the viscosity of the medium, k_BT is the energy of diffusing particle at temperature T. According to Smoluchowski relation (eq. (12)), the rates of chemical or biological reactions are limited by the rates of three-dimensional (3D) diffusion that brings the reactants together (von Hippel and Berg, 1989).

$$k_{encounter} = n(D_A + D_B)(r_A + r_B) \quad (12)$$

where D_A and D_B is the diffusion constants and r_A and r_B are radii of particles A and B and n is constant $4\pi N_0/1000$. The real molecular association rate (k_{assoc}) deviates from the Smoluchowski encounter rate for a number of reasons: a) the surface of the molecules is not uniformly reactive, b) possible electrostatic attractive or repulsive forces could modulate the diffusion-driven association rate, c) the reactive particles may not be spherical, d) the interacting distance may differ from the sum of the hydrodynamic radii of the interacting particles. Based on these reasons, corrected k_{assoc} expression (eq. (13)) includes κ – multiplied surface fractions of interacting molecules, f – unitless factor of electrostatic modulation and a – interacting distance. According to the corrected formula (eq. (13)), the 3D diffusion limit value for DNA and repressor was calculated, where κ=0.05 (0.2 (repressor)×0.25 (DNA)), a=50 Å (40 Å(repressor)+10 Å(DNA)), f=1 (both molecules negatively charged and repel one another, but at close-range they attract each other since the DNA binding cleft of the repressor is positively charged), Diffusion constant of the repressor (D_A) was set to 5×10^{-7} cm^2/s and the low diffusion constant of the large DNA (D_B) was ignored.

$$k_{assoc} = n\kappa af(D_A + D_B) \quad (13)$$

Using the above parameters, k_{assoc} (eq. (13)) for *lac* repressor and a large fragment of DNA approximately equals 10^8 $M^{-1}s^{-1}$. Thus, no 3D diffusion-driven chemical reaction can exceed this rate (von Hippel and Berg, 1989).

1.3.2. Overcoming the diffusion limit

There are two ways for to overcome the diffusion limit: a) by electrostatic attraction, or b) via ‘facilitated diffusion’.

1.3.2.1. Overcoming the diffusion limit by an electrostatic effect

Due to slow diffusion and van der Waals force, collided macromolecules are too slow to drift apart and can include reiterated minicollisions, which results to appreciable rotational rearrangements that overcome surface parameter of interacting molecules κ (eq. (13)). Nature of non-elastic collisions between macromolecules, approaches the association reaction rate to essentially diffusion-controlled, which according to classical Smoluchowski theory forms complex upon every encounter between macromolecules (eq. (12)) (von Hippel and Berg, 1989).

Some macromolecular reactions can exceed so-called essential diffusion limit. Computer simulations revealed that reactions between enzymes and highly charged small molecules like superoxide dismutase and superoxide anion (Sharp et al., 1987) or cytochrome c peroxidase and cytochrome c (Northrup et al., 1988) exceeds diffusion limit, because enzymes set up large electrostatic field about themselves that guide the substrate into the active site. This effect increases steric factor κ and in some directions increases reaction distance *a* (eq. (13)) (von Hippel and Berg, 1989). Electrostatic effect for protein-protein interaction was observed for colicin E3 RNase and its inhibitor Im3. Increased salt concentration reduced association constant of these reactions back to diffusion limit and proved that measured constants exceeded the diffusion limit due to electrostatic interactions (Walker et al., 2003).

There are just three DNA interacting proteins significantly exceeding diffusion limit repressors Gal, Lac and integration host factor (reviewed in (Halford, 2004)). At least for Lac repressor the electrostatic interaction between positively charged protein and negatively charged backbone of the DNA is probably an important factor in increasing the protein-DNA apparent association rate (Halford, 2009). The fact that the majority of DNA interacting proteins

(Halford, 2004), associates at rates close to the diffusion limit, implies that the rate limiting step in binding to the specific DNA site is the proteins encounter to non-specific DNA and then subsequent transfer to specific DNA site (Halford, 2009).

1.3.2.2. Overcoming the diffusion limit by facilitated diffusion

3D diffusion is insufficient as a search mechanism in molecular biology. It was recognized on theoretical ground by Adam and Delbruck, who suggested that bimolecular interaction could be significantly increased by reducing the search dimension, by nonspecific adsorption on a one-dimensional (1D) macromolecule or two-dimensional (2D) membrane and then diffusing in this smaller space (Adam and Delbruck, 1968). Following this hypothesis, the association rate of the *lac* repressor protein to its binding site was measured and the obtained value of 10^{10} $M^{-1}s^{-1}$ was shown to be 100 times higher than the maximal theoretical rate of protein-DNA association achievable by diffusion in solution (Riggs et al., 1970). To resolve this inadequacy, the mechanism was suggested that includes both 3D and 1D diffusion. This mechanism was first proposed by Riggs (Riggs et al., 1970) and then studied and developed by other scientists (Berg and Blomberg, 1976; Berg et al., 1981; Richter and Eigen, 1974).

1.3.3. Facilitated diffusion: Sliding, hopping, jumping, intersegmental transfer

Following the hypothesis of 1D/3D mechanism, different modes can be envisioned to facilitate diffusional target location of protein on DNA. One-dimensional (1D) diffusion or **'sliding'**, during which the protein moves from its initial nonspecific site to its target site along the DNA and remains in contact with the DNA for long enough periods so that significant diffusive motion occurs in either direction along the chain contour (Figure 6A)(Berg et al., 1981). **'Hopping'** has two definitions, it is 1D protein movements along the DNA via a series of

microscopic dissociation and reassociation events to nearby location or it is short rounds of 3D diffusion where the protein dissociates from the DNA and rebinds at a site very nearby (Figure 6B) (Kolesov et al., 2007). **'Jumping'** or diffusion in 3D is the dissociation-association event of protein moving over longer distances or even between different DNA molecules (Figure 6C). There are several definitions which describe differences between 3D hops and 3D jumps: a) by reassociation location hops reassociates at nearby site (correlated) and jumps reassociates at distant sites (uncorrelated) (Kolesov et al., 2007), these definitions correspondingly meet intradomain and interdomain association-dissociation events, where **'**domains**'** are distant volumes occupied by random-coiled DNA molecules (von Hippel and Berg, 1989); b) by distance protein travelled between dissociation and association hops travels <10 bp and jumps >100 bp (Halford, 2009). **'Intersegmental transfer'** is the type of translocation, when protein moves between two sites via an intermediate 'loop', formed by the protein binding both sites concurrently. Such transfers have a mean step size of ~400 bp which is a consequence of the 150 bp "bending persistence length" of DNA, the length over which thermally excited bending occurs. Intersegmental transfer is relevant only to proteins with two DNA binding surfaces (Halford, 2004). Direct intersegment transfer does not favour target location for sites located close along the contour of the DNA (Figure 6D) (von Hippel and Berg, 1989).

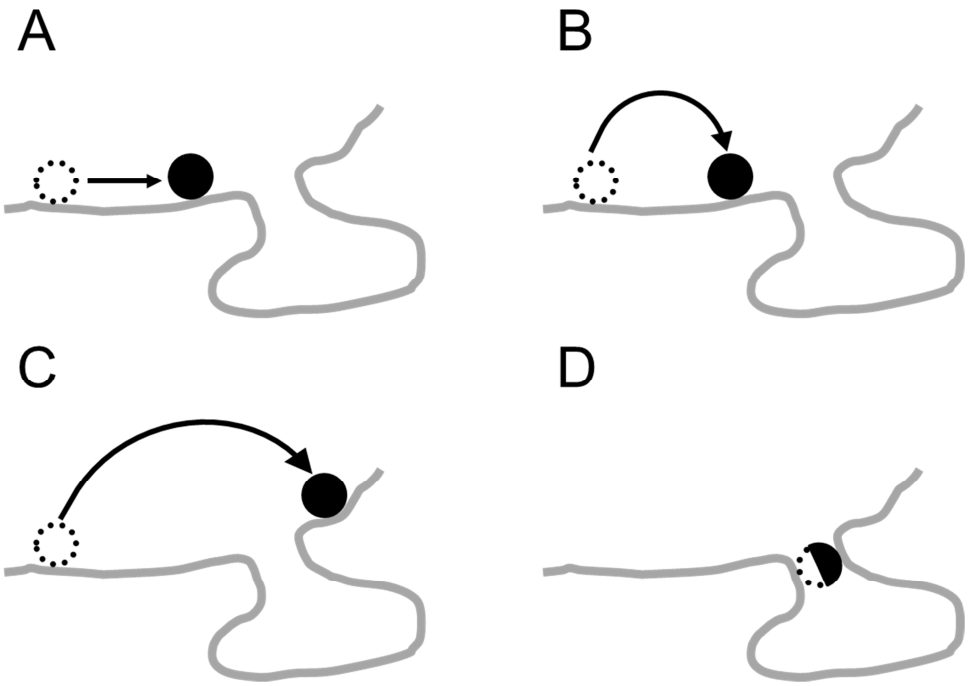

Figure 6. Types of facilitated diffusion. (A) Sliding. **(B)** Hopping. **(C)** Jumping. **(D)** Intersegmental transfer. Figure adopted from (Halford, 2004).

1.3.4. A Theoretical Model for the Protein-DNA Search Process

1.3.4.1 Key parameter: sliding length

Halford and Marko (Halford, 2004) modelled the 1D diffusion of protein on DNA by a random walk in one dimension. The mean position of the protein on the DNA is always at the origin where it initially bound and started to slide. The distribution of $N^{1/2}$ visited base pairs around the mean broaden with N steps.

Authors calculated proteins probability of finding nearby target of size *a* from the distances *r* by diffusion. They divided region of size *r* between the target and protein into $(r/a)^3$ volumetric pixels (‘*voxels*‘) of width *a*. According to mean square distance law for diffusion (eq. (10)) each voxel is visited for a time a^2/D and the region of size *r* visited for a time r^2/D. Traveling distance *r*, after time r^2/D protein visits $(r/a)^2$ ‘*voxels*‘ and binds to target site with probability *a/r* or diffuse away with probability *1-a/r*. Waiting of *r/a* times longer pushes the

probability of protein association to target site up to near certainty, giving a total association time of $r/a \times r^2/D = 1/(Dac)$ (where concentration is in units of number of molecules per volume, then $V = 1/c$ and in the case of single-molecule distance between protein and target equals $r = 1/(c^{1/3})$) and association rate is inverse of this (eq. (14)):

$$k_{assoc} = Dac \quad (14)$$

The main idea of theoretical study is that non-specific association of proteins with DNA can reduce the time required for proteins to find their specific target site, essentially by restricting their motion to along the DNA contour. Facilitated diffusion provides accelerated targeting essentially by increasing the target size *a*, without decreasing the diffusion constant of the protein. To prove how facilitated diffusion modes 'sliding' and 'hopping' (see 1.3.3.) accelerates target site location by protein, 'sliding length' and 'search time' must be determined.

When protein performs random walks along DNA, the number of hydrogen bonds between protein and DNA must be broken and after that two scenarios are possible: a) protein performs 1 bp step along the DNA with rate k_S and form hydrogen bonds with adjacent bp or b) protein will dissociate from DNA with dissociation rate k_{off}. The probability (P_N) that protein will stay on the DNA after N steps is given by equation (15):

$$P_N = [(k_S)/(k_S) + (k_{off})]^N \quad (15)$$

Even with the ratio of 10000:1 for k_S/k_{off} , 99.8 % of the protein molecules will dissociate from the DNA before traveling 250 bp. It is doubtful, that ratio k_S/k_{off} can be large, because the transition state of the protein for 1bp or dissociation requires to break the same number of hydrogen bonds with DNA.

If $P<<1$, then $N=1/P$. Since the 'sliding' is diffusive, after N steps, protein will explore the region of $N^{1/2}=1/(P^{1/2})$ base pairs, giving the characteristic 'sliding length' (l_{sl}) in nanometres by equation (16):

$$l_{sl} = \frac{h}{\sqrt{(P)^N}} \quad (16)$$

where h is pair pair step equals 0.34 nm (Halford, 2004, 2009).

To evaluate the search time, assume that DNA are homogeneously distributed identical coils (Hu et al., 2006) of size $R=\rho(L)$ and a contour length L with one target site in it ($c=1/V$) under isolated coil conditions ($R<<V^{1/3}$). Target search process are divided in two stages. In the first stage protein must travel through the volume V in time $\tau_V=V^{2/3}/D$ with $R/V^{1/3}$ probability to enter the coil. Reciprocal of the probability $n_V=V^{1/3}/R$ equals the number of times protein need to diffuse volume V to find the coil. In the second stage, inside the coil, protein diffuse in the targeting radius $\xi=l_{sl}$, region where protein has 50 % probability to find its target site. If protein diffuse in the region larger than targeting radius, the probability to find specific site equals ξ/R, so protein must visit coil $n_c=R/\xi$. DNA coil has n_ξ regions of size ξ ($n_\xi=\xi L/(Rl)$, where l is contour length of ξ) giving a total DNA visitation time $n_\xi\tau_\xi$. Total search time (eq. (17)) consists of diffusions through total volume $\tau_V n_V$ times and total DNA visitation time $n_\xi\tau_\xi$ multiplied by n_C explorations inside the coil:

$$\tau = n_C n_V \tau_V + n_C n_\xi \tau_\xi \quad (17)$$

After some rearrangements we obtain total search time in terms of the 'sliding length' (eq. (18)):

$$\tau = \frac{V}{D l_{sl}} + \frac{L l_{sl}}{D_1} \quad (18)$$

The first term of the equation is the 3D diffusion time required to come within the targeting radius of the target, the second term is the total sliding time

needed to explore the whole DNA chain (D_1 – 1D diffusion constant, D - 3D diffusion constant). The equation can be rewritten in the form of the reaction rate per unit protein concentration (eq. (19)):

$$k = \left(\frac{1}{D l_{sl}} + \frac{L l_{sl}}{D_1 V}\right)^{-1} = Da\left(\frac{a}{l_{sl}} + \frac{D}{D_1} a L l_{sl} c\right)^{-1} \quad (19)$$

The equation consists of 3-D diffusion-limited rate (Da) and acceleration factor. Equation analysis revealed that at fixed sliding length (l_{sl}) to 100 bp, the reaction accelerates to about 30 times above 3-D diffusion limit when target site (a) concentration is reduced to low concentration limit of l_{sl}/a. According to equation (19), acceleration factor (equals to theoretical association rate normalized to the diffusion limiting rate $k/(Da)$) plot to sliding length normalised to binding site size (l_{sl}/a) revealed no acceleration at $l_{sl}=a$ when sliding and 3-D diffusion constants were kept equal. In the presence of sliding ($l_{sl}>a$), the association rate is increased to acceleration maximum at certain l_{sl} value and after this value is exceeded, association rate starts to decelerate. Deceleration occurs, because too long sliding length results in oversampling of DNA contour symmetrically from the association point. To obtain the acceleration, after sampling optimal sliding length, preferably to periodically jump and associate to new region.

Similar facilitated diffusion analysis of DNA-binding proteins was performed by Klenin (Klenin et al., 2006).

1.3.4.2 Key parameter: sliding time

Mirny and Slutsky (Slutsky and Mirny, 2004) describes searching process of specific DNA target site by protein as following rounds of diffusion in 3D and 1D. Consider a single protein searching for a single target site on a M bp long DNA and on average scans n base pairs in each round of 1D diffusion, then the total search time is given by equation (20):

$$t_S = \frac{M}{\bar{n}}\left(\tau_{1D,i} + \tau_{3D,i}\right) \quad (20)$$

where $\tau_{1D,i}$ and $\tau_{3D,i}$ are the durations of 1D and 3D diffusion, in the *i*th round of searching

During 1D diffusion time interval $\tau_{1D,i}$, protein on average scans n=($16\ D_{1D}\ \tau_{1D}/\pi$) bps. Combining n expression with t_S expression and setting $dt_S/d\tau_{1D}$=0 to find the minimum search time, authors obtained optimal searching time (eq. (21)) and optimal number of bp scanned per single 1D search (eq. (22)).

$$t_S\left(n_{opt}\right) = \frac{M}{2}\sqrt{\frac{\pi\overline{\tau_{3D}}}{D_{1D}}} \quad (21)$$

$$\bar{n}_{opt} = \sqrt{\frac{16}{\pi}D_{1D}\tau_{3D}} \quad (22)$$

The optimal search regime was obtained at $\tau_{1D}(n_{opt})=\tau_{3D}$, this means that protein spends equal amount of time diffusing along nonspecific DNA and diffusing in the solution, this result is irrespective to D_{1D} or D_{3D}, or genome size M. Analysis revealed that optimal 1D/3D search is n_{opt} times faster than 3D diffusion alone and M/n_{opt} times faster than 1D diffusion alone. If n_{opt}=100 bp and protein acts in optimal regime, the binding time to specific target site is 100 times faster than rate achievable by 3D diffusion.

The maximal n_{opt}=500 bp could be reached at an optimal regime when diffusion coefficients is set to the limit $D_{1D}=D_{3D}=10^{-7}$ cm^2/s and shortest possible search time of the target at M=10^6 is about 5 s.

1.3.5. The two-state model: Speed-stability and speed-selectivity paradox

Since the energy of protein binding to DNA depends on the DNA sequence, the protein experiences different energies at different positions while

sliding along the DNA. To model the energy of binding of protein-DNA interactions, the position weight matrix approximation was applied, which assumes that base pairs in any fragment of DNA contributes independently and additively to the total binding energy.

Authors (Slutsky and Mirny, 2004) assumed a sequence-dependent energy landscape as a random field with energies independently and normally distributed. By averaging the mean first-passage time for a 1D random walk over the normally distributed energies they obtained equation (23):

$$D_{1D} = \exp[-\gamma \left(\frac{\sigma}{k_B T}\right)^2] \quad (23)$$

where $\gamma=1$, and σ^2 is the variance of the protein-DNA binding energy distribution. Based on the rapid decay of the diffusion coefficient as a function of the ruggedness of the energy landscape, authors suggested that fast sliding is possible to explain just for small variance of the sequence-dependent energy landscape $\sigma \leq 1\text{-}2\ k_B T$. Assuming 1D/3D searching model ($\tau_1=\tau_3$), conditions necessary for fast searching (sliding) ($\sigma \leq 1\text{-}2\ k_B T$) are very different from the recognition conditions, when protein must bind its cognate site with great thermodynamic and kinetic stability to support its biological function and it requires the lowest binding energy at the target site. The variance of the sequence – dependent binding energy determines not only the rate of sliding, but also the energy of the target site E_0, and then equilibrium of the occupancy of the target site P_{eq} equals the fraction of time protein spends at the target site (eq. (24)):

$$P_{eq} = \frac{\exp(-E_0/k_B T)}{\sum_{i=1}^{M} \exp(-E_i/k_B T)} \quad (24)$$

where energies E_i of individual sites are drawn from a normal distribution with the variance σ^2 and the target site with the lowest energy in the genome. It was calculated that recognition conditions $P_{eq} \geq 0.25$ requires $\sigma \geq 5\ k_B T$ which is

energetically inconsistent with searching mode ($\sigma \leq 2\ k_B T$) and lead to speed - stability paradox.

The authors proposed that presence of two distinct searching (S) and recognition (R) conformational states of the protein could resolve this paradox. The system must be defined by the difference between the mean energy in the two states ΔG_{RS} and the rate of transitions between the two states S→R (k_{SR}) and R→S (k_{RS}), which ratio gives equilibrium constant (eq. (25)):

$$K_{eq} = \frac{k_{SR}}{k_{RS}} = \exp(-\Delta G_{RS}) \quad (25)$$

Fast search state S has two opposite effects on the search: it helps to accelerate the search by fast 1D sliding in the S state, but it can make search prohibitively slow if the target site is visited only in the S state and not recognized in R state. The two states model requires: a) to undergo fast conformational transition, faster than $n/\tau_{1D}=10^3–10^4$ s, b) R state should be favourable on the target site, but unfavourable elsewhere. This means that mean binding energy of R state must be much higher than in S state, in these conditions protein spends most of the time in the S state and changes state to R mainly at the target site. If sliding and recognition energy profiles are correlated, the lowest lying energy levels in the search mode are likely to correspond to the strongest sites in the recognition mode, transitions mainly happen at these sites (Slutsky and Mirny, 2004). This model is correct when scanning length of the DNA is significantly larger than protein recognition site (Veksler and Kolomeisky, 2013).

1.3.6. Experimental observation of protein diffusion along DNA

1.3.6.1. Ensemble averaging experiments

Theory, that proteins employ facilitated diffusion for target site location, became clear, when ensemble averaging experiments have been started to

perform. First examined restriction enzyme EcoRI on 34 bp to 6200 bp DNA substrates with centrally located EcoRI site revealed that external DNA sequences in the range of 34-4000 bp enhance the EcoRI – specific site association and dissociation rates, and equilibrium constant remained independent from the DNA contour length with all tested substrates (Jack et al., 1982). It was also observed that external sequences enhance cleavage rate of the specific DNA substrates by restriction enzymes EcoRI, BamHI and HindIII (Ehbrecht et al., 1985). Kinetic experiments performed with EcoRI and linear or circular two targets site DNA substrates separated by 51 bp revealed that processivity factor on 388 bp circular substrate were twice higher (0.77) than determined on linear substrates (0.38 for 1027 bp and 0.46 for 388 bp). On linear substrate it is explained that EcoRI generates two DNA products and roughly half of the enzymes could slide to the second target site, while cleavage of the circular DNA substrate produces one DNA product and after that protein can successfully search second target from both ends of DNA. Most rapid cleavage of the substrates was observed by EcoRI when target sites are centrally positioned. Upon association with unspecific DNA, EcoRI consumes equal amount of time to scan DNA and find specific site, starting from each side of the substrate (Terry et al., 1985). Kinetic experiments performed in competitive manner with two 30 bp and 912 bp DNA substrates, each of them possess two EcoRI recognition sequences at position 5 and 13. Both recognition sites on 30 bp DNA substrate were cleaved with comparable rates, but on the 912 bp DNA substrate, rate enhancement of 3 times was observed for second target site in 894 bp distance and no cleavage rate enhancement was observed for the first target site with 4 bp arm. Long DNA arm acts as antenna, and enhances the cleavage of the second target site by linear diffusion. Experiment with 912 bp DNA substrate which possesses single EcoRV target site at 13 position and different “star” sites (DNA sequences which differs from recognition sequence by 1 nt) adjacent to the target site on the longer arm,

revealed that “star” sites slows down cleavage rate of the recognition sequence. These experiments revealed, that only translocation type on DNA employed by EcoRI is sliding, because enzyme does not “overlook” any cleavage site and linear diffusion is slowed down by sites which is resemble to target site (Jeltsch et al., 1994). Sliding, as the only mechanism for target site location is also employed by restriction endonuclease BssHII. Kinetic experiments on DNA substrate with three overlapping BssHII target sites revealed that only external targets are cleaved (Berkhout and van Wamel, 1996).

Restriction enzyme EcoRV investigation reveals that enzyme binds all DNA sequences with equal affinity (Taylor et al., 1991) are in agreement with 1D/3D facilitated mechanism, which consists of repetitive cycles of 3D diffusion, which brings protein from solution to non-specific DNA contour, and then protein slides along the DNA contour (1D) to its specific site (see 1.3.2.2.) (Berg et al., 1981). Kinetic experiments on linear DNA substrates with free or blocked ends revealed that EcoRV have very little probability to fall from substrate and after “reflection” from the end it continues to diffuse on the DNA (Jeltsch and Pingoud, 1998). EcoRV kinetic analysis on two target sites substrates with intersite distance of 54 bp, 200 bp, 387 bp and 764 bp revealed that processivity factors (eq. (26)) of substrates with increasing intersite distances declines by factors of 1.5-, 2-, or 3-fold in comparison with 54bp substrate. Obtained results are far from 15-, 50- and 200-fold processivity reduction predicted by random walks theory of 1D diffusion. Absence of k_S/k_{off} value (eq. (15)) that fits to f_P values (eq. (26)) for all tested substrates proves that transfer mechanism between target sites just by 1D diffusion is not sufficient and successive rounds of 1D/3D diffusion must occur. Calculations revealed that during single 1D excursion, EcoRV scans 56 bp before dissociation, it follows that transfer efficiency is unprocessive when intersite distance is far bigger than 56 bp, and it becomes processive and independent of the spacing when it approaches 56 bp (Stanford, 2000). Further EcoRV kinetic

experiments revealed specific site location on the supercoiled (SC) 346 bp DNA circle catenated to the larger DNA circle (3466 bp) over free 346 bp DNA minicircle. It proved existence of 3D steps during target search and protein-DNA binding rate enhancement by large non-specific DNA. SC plasmid (3466 bp) preference over SC catenane (3466 bp+346 bp) could be explained by higher fraction of 1D steps over 3D steps or higher degree of specific site confinement in SC catenane. Statement that supercoiling compresses the volume of the DNA and shortens the searching distance by 1D/3D mechanism from any DNA point to the target site plasmid was proven by SC plasmid preference over relaxed plasmid (Gowers and Halford, 2003). Summary and comparison of EcoRI and EcoRV target searching modes are described in paper of Norbert Reich group (Pollak et al., 2014).

$$f_P = 0.5 \times P_N \quad (26)$$

The fact that restriction endonuclease BbvCI recognizes asymmetric sequence CCTCAGC, triggered authors to perform kinetic experiments with DNA substrates containing two target sites in the repeated (R) (same) or inverted (I) orientations. Varying distances between target sites (30 bp, 40 bp, 45 bp 75 bp) and NaCl concentration (0 mM, 30 mM, 60 mM, 150 mM), set of kinetic experiments was performed and the ratios of processivity factors were calculated. Steady-state kinetic experiments revealed that BbvCI acts with equal almost maximum processivity on R substrates with small intersite distances (30 bp, 40 bp, 45 bp) in the absence of additional salt. In the same conditions BbvCI acts more processively on substrates with R target sites than on substrates with I target sites. Increase of NaCl concentration (30 mM, 60 mM) decreased processivity factors itself and ratios of processivity factors (R/I) which is equalized at 150 mM NaCl. Kinetic experiments on R and I DNA substrates with 75 bp intersite distance revealed equal processivity factors in all salt concentrations. If BbvCI would employ just 1D diffusion for target search, processivity factor for substrates

with inverted target sites would be zero, thus 3D steps must be also involved in the searching process. Additional experiments revealed, that increasing concentration of salt weakens BbvCI binding to DNA. In other words high salt concentration should increase the ratio of 3D/1D steps and decrease the probability to reassociate at the local sites after dissociation. These experiments proved that at low salt concentration protein travels by 1D diffusion between target sites up to 50 bp apart. Transfers of >30 bp at in vivo salt, and over distances of >50 bp at any salt, always included at least one dissociation step (Gowers et al., 2005).

DNA repair enzymes as the REases are also employs facilitated diffusion when acts on DNA. This fact was proved by testing DNA repair enzymes on DNA substrates with two damaged nucleotides on the same or different DNA strands. Uracil DNA glycosylase (UNG) is the enzyme which captures and excises extrahelical uracil bases which emerged from DNA base stack by spontaneous base pair breathing motions. Kinetic experiments on the two site substrate revealed that intramolecular transfer efficiency (processivity factor) decreases from 41 % to 0 % when intersite distance increases from 20 bp to 800 bp and revealed that UNG slides along DNA over short distances. Equal intramolecular transfer efficiencies obtained on substrates with short intersite distances (20 bp, 56 bp) regardless of the damaged nucleotide locations on the same or on the different strands, supports the prediction that UNG also employs hopping for target site location. Employing the theory of the probability of finding the nearby target (Halford, 2004; Stanford, 2000), calculated size of the effective target appeared to be ≈10 bp. Taking into account UNG binding time ($\tau=1/k_{esc}=1/K_D\times k_{on}$) of 5 ms and T/A and U/A opening rate 8 ms^{-1} (determined by NMR), four opening events will be sampled if one U/A base-pair would appear in the region of ≈10 bp (Porecha and Stivers, 2008). Using the same strategy, the

ability of sliding between two target sites was demonstrated for alkyl-adenine DNA glycosylase (AAG) (Hedglin and O'Brien, 2008).

Investigation of target search by human 8-oxoguanine DNA glycosylase 1 (hOGG1) was also performed using set of two target sites DNA substrates with intersite distance (5-156 bp). Processivity factors anticorrelated with intersite distances between target sites. Trap experiments with 8-oxoguanine analogue were performed to determine processive action of protein from only by 1D pathway with trap or by 1D/3D pathway and calculate transfer efficiency input by only 3D. Reduction of processivity factor was observed because fractions of hOGG1 molecules was irreversibly trapped during 3D steps. These experiments proved that hOGG1 employs both sliding and hopping for target search. Kinetic experiments with trap on substrate with two target sites on different strands (10 bp intersite distance) and substrate with internal block between targets (15 bp intersite distance) revealed that hOGG1 acts less but still processively despite dissociative search pathway is excluded under these conditions. This experiment revealed that hOGG1 can slide not only along phosphate backbone and can overcome blocks without dissociation step (Rowland et al., 2014).

Ensemble studies made huge impact on our understanding of target-search mechanism and remain valuable tool for assessing how proteins move on DNA. However most experimental studies could only address whether or not a protein might travel by facilitated diffusion. Types of facilitated diffusion could be distinguished relying on the properties of protein target recognition (Gowers et al., 2005; Porecha and Stivers, 2008) or on type of kinetic experiment performed (Rowland et al., 2014). These and all the other ensemble averaging experiments relies on endonucleolytic properties of examined proteins and cannot be applied to proteins which do not cleave nucleic acids (Gorman and Greene, 2008).

1.3.6.2. Single-Molecule Experiments to Visualize Protein-DNA Interactions

Investigation of target site searching paths by proteins that do not hydrolize nucleic acids requires to detect completely different signal and employ different method.

TIRFM (total internal reflection fluorescence microscopy) is the method based on the evanescent wave. Because of the exponential decay, it penetrates into solution about 100 nm and capable of exciting fluorescent molecules (see 1.1.6.2.) that might be present near the interface of two phases, but does not excite fluorescent molecules that diffuses deeper in solution, giving us high signal-to-noise ratio of excited fluorescently labelled molecule of interest and allows us to detect single molecules. For this reason TIRFM are used in combination with other setups and became widely applied in explorations of proteins that acts on DNA.

Investigation of proteins that act on DNA, requires stretching of DNA molecules along the contact area of solution and glass by immobilizing one end of DNA molecule on the prepared glass surface and employing biotin-streptavidin (Diamandis and Christopoulos, 1991) or digoxigenin - antidigoxigenin (Kessler, 1991) strong interactions. Another end of DNA molecule could be stretched using TIRF setup in combination with magnetic tweezers (Schwarz et al., 2013) (see 1.2.1.2.,2.2.11.3., Figure 19), optical tweezers (Harada et al., 1999) (see 1.2.1.1.) or applying laminar flow (Kim and Larson, 2007) through experimental cell (see 2.2.9.).

When the DNA are already stretched, fluorescently labelled proteins (see 1.1.5.2.) are applied to the experimental flow-cell in the range of pico- to nanomolar concentration. Excitation are performed with laser and emission of the fluorophore, which comes through the sophisticated optical system, are detected

with EMCCD camera and recorded as the set of frames (Schwarz et al., 2013). The biggest challenge is to analyse and extract valuable information from the data. For determination of the proteins 1D diffusion coefficient, each single fluorescent particle must be localized with point spread-function (PSF) and the coordinates of them must be tracked over the recorded set of frames (Michalet, 2010; Ruhnow et al., 2011; Saxton and Jacobson, 1997; Thompson et al., 2002). Obtained data are used to calculate 1D diffusion coefficient from particles mean-squared displacement (MSD) over time graphs fit. If 1D diffusion coefficient provides information about particles diffusion rate, MSD shape provides information about type of diffusion. There are three main types of diffusional motion: a) pure diffusion, b) diffusion with flow or c) confined diffusion (Qian et al., 1991; Saxton and Jacobson, 1997).

1.3.6.3. Type of single protein motion along DNA.

Shape of the double helix DNA and a comparable size of the DNA interacting proteins, suggests that during the 1D diffusion, proteins must follow the helical path of the DNA. The first theoretical model suggested that protein's translational diffusion along DNA is accompanied by rotation along DNA helical path. In this model the protein is approximated as a sphere of radius R and the centre of the protein's mass are always on the DNA axis (Schurr, 1979). According to Stokes-Einstein relation (eq. (27), where k_B is Boltzman's constant, T is absolute temperature and ζ is drag coefficient), diffusion coefficient inversely depends on the drag coefficient. Total translational drag coefficient (eq. (28)) for symmetrically bound protein (Figure 7A) reveals that rotational friction with dependence of R^3 (second term of the equation (28)) is by two orders of magnitude larger than translational friction with dependence of R (first term of the equation (28)).

$$D = \frac{k_B T}{\zeta} \quad (27)$$

$$\zeta_{Trans}^{Symm} = 6\pi\eta R + \left(\frac{2\pi}{10BP}\right)^2 8\pi\eta R^3 \quad (28)$$

where η is the viscosity of the medium and ($2\pi/10BP$) means 2π radians rotation after translation of 10 bp (BP=0.34 nm).

If protein binds to DNA asymmetrically and the distance between DNA symmetry axis and protein centre of mass is R_{OC} (Figure 7B), then equation (29) describes the drag coefficient where third term shows the contribution to the total drag from the asymmetricity (Bagchi et al., 2008).

$$\zeta_{Trans}^{Asymm} = 6\pi\eta R + \left(\frac{2\pi}{10BP}\right)^2 8\pi\eta R^3 + \left(\frac{2\pi}{10BP}\right)^2 6\pi\eta (R_{OC})^2 R \quad (29)$$

Diffusion of the single molecules on DNA appears as exclusively translational, because of the spatiotemporal resolution limitations of the single-molecule setups. Nevertheless, limitations might be overcome and type of the diffusion determined by varying size (R) of the attached fluorescent probes to the protein of interest and then plot D_1 values vs. $1/R$, $1/R^3$ or $1/(R^3+¾R(R_{OC})^2$ (Blainey et al., 2009).

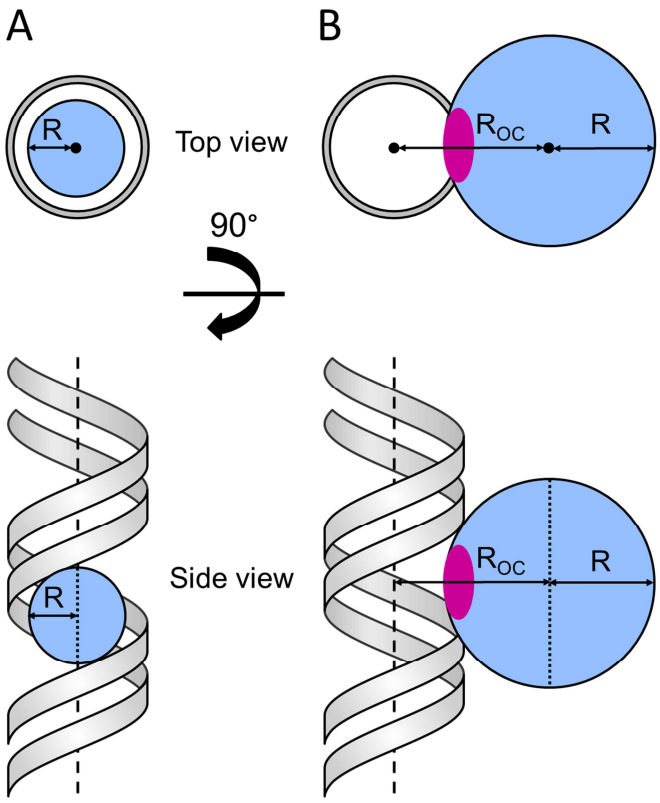

Figure 7. Types of curvilinear motions. According to **(A)** symmetric curvilinear type motion, protein follows the path of the DNA double helix and it experiences hydrodynamic drags of linear motion and rotation aruond its axis (see eq. (28)). In this type of motion DNA symmetry axis and protein center of mass overlaps. In the case of **(B)** asymmetric curvilinear motion, DNA symmetry axis and protein center of mass are separated by distance R_{OC}. During motion protein experiences hydrodynamic drags of linear motion, rotation aruond its axis and circular translation with R_{OC} radius (see eq. (29)) where DNA binding site (purple elipse) always faces DNA symmetry axis. R – protein radius.

1.3.6.4. Proteins that employ facilitated diffusion

The theoretical method described above (see 1.3.6.3.) was applied for single molecule experiments and asymmetrical rotation-coupled translation (eq. (29)) was determined for human oxoguanine DNA glycosylase 1 (hOgg1). Cy3B or fluorescent streptavidin labelled protein was tested on flow stretched linear DNA templates (see 1.3.6.2.) on TIRF setup (see 1.1.6.2.) and obtained D_1

values perfectly fitted in the D_1 vs. $1/(R_3+¾R(R_{OC})^2)$ linear plot (Blainey et al., 2009). Asymmetrical rotation-coupled translational diffusion was proved for another seven proteins that R differs significantly from R_O in the complex with DNA: *E. coli* LacI-YFP dimer diffusing in the living cell (Elf et al., 2007), *B. stearothermophilus* MutY, *E. Coli* MutM M74A, the adenoviral AVP-pVIc complex, the BamHI restriction endonuclease dimer, and the Klenow fragment of *E. coli* DNA polymerase I (Blainey et al., 2009).

Complex and detailed analysis of EcoRV diffusion along DNA was performed using D1 diffusion coefficients of EcoRV labelled with Cy3B (Bonnet et al., 2008), Cy3-labelled streptavidin tetramer (Bonnet and Desbiolles, 2011), quantum dots 655 (Biebricher et al., 2009), EO6, 605 and dimeric protein scRM6-Cy3B (Dikic et al., 2012). Four different theoretical diffusion friction models were discussed, where translational and rotation-coupled diffusion were combined with flexible or rigid linker of the protein label. Analysis revealed that EcoRV diffuses along DNA in rotation-coupled manner and linker of the labels are flexible (Dikic et al., 2012). EcoRV is the first DNA-interacting protein which ability to perform jumps was demonstrated employing single molecule methods. The small value of measured EcoRV-Cy3B 1D diffusion constant in comparison with 3D diffusion value is explained as effect of hydrodynamic drag and modulation of the DNA-protein interaction potential (Bonnet et al., 2008).

Gene alterations and mutations of tumour suppressor p53 are responsible for more than 50 % of all human tumours. 1D diffusion experiments on the flow stretched DNA molecules revealed that unlike full-length p53 or core domain of p53, C-terminal domain translocates on DNA rapidly (Table 1). These results suggest two-state p53 mechanism (see 1.3.5.). In the search mode, p53 is bound to DNA just with C-terminal domain, resulting fast sliding along DNA, in the recognition mode the protein is bound to DNA with both C-terminal and core domain resulting in a slower translocation along DNA (Tafvizi et al., 2011b).

Single molecule experiments on the flow-stretched DNA revealed that *S. Cerevisiae* heterodimeric mismatch repair (MMR) complex Msh2-Msh6 (MutS homolog of *E. Coli* MutHLS mismatch repair system) rapidly diffuses along the DNA while searches mismatches but never hops. No trapping and constant diffusion rate was observed at different salt concentration or competitor DNA. Absence of 3D steps was directly proved by labelling Msh2-Msh6 complex with different quantum dots and observing that diffusion paths or differently labelled complexes never crossing on DNA (Gorman et al., 2007). During MMR Msh2-Msh6 must locate lesions and differentiate parental and nascent DNA strands from nearby signals, Mlh1-Pms1 must locate lesion-bound Msh2-Msh6 and coordinate downstream steps in the MMR. Absence of punctures in Mlh1-Pms1 1D diffusion kymographs on doubly-stretched DNA curtains revealed that no jumps occurs during Mlh1-Pms1 DNA translocation, but increased 1D diffusion constant (Table 1) using elevated salt concentration (200 mM vs. 25 mM NaCl) argued that hopping mechanism should occur. Diffusion detection of Mlh1-Pms1 complexes labelled with different quantum dots revealed that complexes could bypass each other. Experiments on stretched DNA with nucleosomes and labelled Mlh1-Pms1 complex was performed and after it nucleosomes were labelled with quantum dots, comparison of QD positions with kymographs revealed that Mlh1-Pms1 complexes can overcome nucleosomes and proved hopping mechanism of Mlh1-Pms1 complex. Although Msh2-Msh6 and Mlh1-Pms1 are both ATPases, neither uses ATP for generating chemomechanical force (Gorman et al., 2010). Single molecule experiments on the flow-stretched DNA “curtains“ by applying different flow rates, revealed that C-domain of E.coli repair protein Ada (C-Ada) searches alkylated guanines and thymines employing 1D sliding along DNA without hops (Lin et al., 2009).

Rad51 is the primary eukaryotic recombinase responsible for initiating DNA strand exchange during homologous recombination. Single molecule

experiments revealed that Rad51 slides along DNA in 1D diffusion manner and becomes immobile when reaches free end of ds DNA. Authors suggested that lateral diffusion may enable recombinase to scan damaged DNA regions or facilitate delivery of other repair proteins (Granéli et al., 2006).

Homotrimeric ring-shaped proliferating cell nuclear agent (PCNA) loaded by replication factor C onto primer-template junction serves as processivity factor for eukaryotic replicative polymerases δ and ε and interacts with large number of signalling, replication and repair proteins to coordinate replication and repair. Molecular dynamics simulation suggests that conservative positively charged residues of the PCNA channel make dynamic contacts with DNA backbone phosphates usually disrupted by ions from solution and weak PCNA-DNA interaction allows linear PCNA diffusion on the DNA. Single molecule experiments were performed on the doubly-stretched λ-DNA molecules with Alexa555 or Qdot605 labelled PCNA. Addition of low molecular weight (glycerol), and high molecular weight (PEG 6000) viscogens, which respectively alters total (translational + rotation-coupled diffusion) or just translational diffusion, revealed that Alexa555-PCNA tracks helical pitch when sliding along DNA because diffusion coefficient was decreased just by addition of glycerol and PEG6000 had no effect. For QDot605-PCNA, 62 times decrease of diffusion constant for helically tracking model was expected in the buffer without viscogens, but just 2-fold smaller diffusion coefficient was obtained (Table 1) This result inconsistent with rotation-coupled diffusion theory (see 1.3.6.3.) and suggests that increasing hydrodynamic radius of PCNA also increases probability of switch to non-helical diffusion path (Kochaniak et al., 2009).

Unlike PCNA, its structural homolog, processivity factor of herpes simplex virus UL42 binds to DNA as a monomer. UL42 diffusion on tethered DNA were tested in different salt concentrations. Diffusion coefficients of UL42 correlates with salt concentration and supports UL42 hopping ability (Komazin-Meredith et

al., 2008) (Table 1). According to Berg theory, at the higher ionic force, counter ions of DNA phosphates lower the binding affinity and increase the fraction of time the protein electrostatically not interacting with DNA, this allows to diffuse further before rebinding to DNA and increase diffusion coefficient. In the sliding mode, electrostatic contacts are maintained constantly, so diffusion coefficient are independent from ionic force (Berg et al., 1981).

Type III restriction endonuclease EcoP15I (Res_2Mod_2, Mod – responsible for target methylation, Res – responsible for ATPase and endonuclease activities) can cleave DNA substrates with two recognition sites in the head-to-head (HtH) or tail-to-tail (TtT) orientation. EcoP15I associates with its recognition site and after hydrolysis of ~30 ATP molecules, conformational changes in the protein undergoes and EcoP15I starts to diffuse along DNA until collides to another specific site bound EcoP15I with Res_2 ends and hydrolyses DNA near recognition site (van Aelst et al., 2010; Ramanathan et al., 2009). Single molecule experiments on magnetic tweezers stretched DNA helped to determine reaction mechanism and diffusion coefficient of EcoP15I (Schwarz et al., 2013) (Table 1.).

First enzyme to perform 1D diffusion determined with single molecule methods was *E.coli* RNA polymerase. On optical tweezers stretched On λ-phage DNA stretched with optical tweezers, 1D diffusion undergoing polymerases were observed. Authors also mention that polymerase molecules better associates to relaxed DNA than to stretched (Harada et al., 1999) (Table 1.). 1D diffusion were also determined for T7 RNA polymerase on the flow stretched DNA (Table 1.). On the single stretched DNA molecules, polymerisation was observed in real time due to incorporation of AlexaFluor 488-UTP or AlexaFluor 546-UTP (Kim and Larson, 2007).

Table 1. Proteins that employ facilitated diffusion.

Protein	Label	D_1, 10^{-2} μm^2/s	Method	Reference
C-Ada	Cy3	130±0.2	TIRFM+DNA curtains	(Lin et al., 2009)
EcoP15I	QD 625	92±6	TIRFM+magnetic tweezer	(Schwarz et al., 2013)
EcoRV	Cy3B	0.9-1.2±0.2	TIRFM+both-ends bound DNA molecules	(Bonnet et al., 2008)
EcoRV	QD655	0.32±0.02	TIRFM+Optical tweezer	(Biebricher et al., 2009)
EcoRV	QD655	0.32±0.04	TIRFM+both-ends bound DNA molecules	(Biebricher et al., 2009)
EcoRV	savCy3	1.2±0.1	TIRFM+both-ends bound DNA molecules	(Bonnet and Desbiolles, 2011)
EcoRV	QDEO6	1.1±0.2	TIRFM+both-ends bound DNA molecules	(Dikic et al., 2012)
EcoRV	QD605PEG 2	0.48±0.07	TIRFM+both-ends bound DNA molecules	(Dikic et al., 2012)
EcoRV	QD605PEG 11	0.63±0.07	TIRFM+both-ends bound DNA molecules	(Dikic et al., 2012)
EcoRV-scRM6	Cy3B	0.24±0.04	TIRFM+both-ends bound DNA molecules	(Dikic et al., 2012)
GFP-LacI	GFP	2.1(0.023-13)	TIRFM, two LacI-lacO256 of DNA dimer sites stuck to surface	(Wang et al., 2006)
hOgg1	Cy3B	56±13	TIRFM+one-end bound DNA molecule+flow	(Blainey et al., 2009)
hOgg1	streptavidin-Alexa546	26±1	TIRFM+one-end bound DNA molecule+flow	(Blainey et al., 2009)
Mlh1-Pms1	Qdot585 Qdot705	2.6±1.7 (25mM NaCl)	TIRFM+DNA curtains	(Gorman et al., 2010)
Mlh1-Pms1	Qdot585 Qdot705	99±41 (200 mM NaCl)	TIRFM+DNA curtains	(Gorman et al., 2010)
Msh2-Msh6	Qdot565, Qdot705	1.2±1.8	TIRFM+both-ends bound DNA molecules	(Gorman et al., 2007)
p53	Alexa555	16.2±1.7	TIRFM+one-end bound DNA molecule+flow	(Tafvizi et al., 2011b)

See next page for Table 1 extension

Extension of the Table 1

p53 core domain	Alexa555	2.4±0.5	TIRFM+one-end bound DNA molecule+flow	(Tafvizi et al., 2011b)
p53 C-terminal domain	Alexa555	77.6±9.8	TIRFM+one-end bound DNA molecule+flow	(Tafvizi et al., 2011b)
PCNA	Alexa555	116±7	TIRFM+both-ends bound DNA molecules	(Kochaniak et al., 2009)
PCNA	QD605	55±4	TIRFM+both-ends bound DNA molecules	(Kochaniak et al., 2009)
Rad51	Alexa555	4.2±5.4(0.1-21)	TIRFM+both-ends bound DNA molecules	(Granéli et al., 2006)
RNAP	Cy3	1	TIRFM+Optical Trap	(Harada et al., 1999)
T7 RNA pol	Rhodamine	0.61-43	TIRFM+DNA curtains	(Kim and Larson, 2007)
UL42	Cy3B	2.08	TIRFM+both-ends bound DNA molecules	(Komazin-Meredith et al., 2008)

2. MATERIALS AND METHODS

2.1. Materials

2.1.1. Chemicals

All chemicals used in this study were of the highest quality available.

2.1.2. Enzymes

DNA modifying enzymes (T4 polynucleotide kinase, T4 DNA ligase, restriction enzymes and polymerases) were purchased from Thermo Fisher Scientific and New England Biolabs were used according to the manufacturer's recommendations.

2.1.3. Buffers and solutions

Buffer A+0.1: 10 mM potassium phosphate (pH 7.0 at 25 °C), 0.1 M NaCl, 1 mM EDTA;

Buffer A+0.2: 10 mM potassium phosphate (pH 7.0 at 25 °C), 0.2 M NaCl, 1 mM EDTA;

Buffer A+1: 10 mM potassium phosphate (pH 7.0 at 25 °C), 1 M NaCl, 1 mM EDTA;

Storage buffer: 10 mM Tris-HCl (pH 7.4 at 25 °C), 0.2 M NaCl, 1 mM EDTA, 1 mM DTT, 50 % (v/v) glycerol);

Labelling buffer: 100 mM K-Pi, 100 mM NaCl (pH 6.9 at 25 °C), 1 mM TCEP;

Measurement buffer 33 mM Tris-acetate, 66 mM CH_3COOK, (pH 7.9 at 25 °C), 0.1 mM EDTA, 0.02 mg/ml glucose oxidase, 0.008 mg/ml catalase, 20 mM glucose, 0.1 mg/ml BSA, saturated TROLOX solution;

Reaction buffer: 33 mM Tris-acetate, 66 mM CH_3COOK (pH 7.9 at 25 °C), 0.1 mM EDTA;

Binding buffer: 40 mM Tris-acetate (pH 8.3 at 25 °C), 5 mM $Ca(OAc)_2$, 0.1 mg/ml BSA, 10 % (v/v) glycerol;

EMSA running buffer: 40 mM Tris-acetate (pH 8.3 at 25 °C), 5 mM $Ca(OAc)_2$;

NBE buffer: 0.1 M H_3BO_3, 0.1 M NaOH, 0.2 mM EDTA, 15 mM sodium acetate, pH 8.0 at 25 °C;

PBS buffer: 2.7 mM KCl, 137 mM NaCl, 10 mM phosphate, pH 7.4 at 25 °C, (Sigma);

TAE buffer: 40 mM Tris-acetate, 1 mM EDTA, pH 7.9 at 25 °C;

TBE buffer: 0.1 M Tris-H_3BO_3, 2 mM EDTA, pH 8.3 at 25 °C;

Non-denaturing loading dye solution: 75 mM EDTA (pH 8.0 at 25 °C), 0.01 % bromphenol blue (w/v), 0.1 % SDS, 50 % (v/v) glycerol;

Denaturing loading dye solution: 95 % (v/v) formamide, 25 mM EDTA (pH 8.0 at 25 °C), 0.01 % bromphenol blue (w/v);

SDS loading solution: 100 mM Tris-HCl (pH 6.8 at 25 °C), 4 % SDS (w/v), 200 mM DTT, 20 % (v/v) glycerol;

PE1 buffer: 125 mM Tris-HCl (pH 6.8 at 25 °C), 0.1 % SDS (w/v);

PE2 buffer: 375 mM Tris-HCl (pH 8.8 at 25 °C), 0.1 % SDS (w/v);

PE3 buffer: 25 mM Tris, 190 mM glycine (pH 8.3 at 25°C), 0.1 % SDS (w/v);

“Acrylamide” solution I: acrylamide/N,N′-methylenebisacrylamide (37.5:1 (w/w)) solution;

“Acrylamide” solution II: acrylamide/N,N′-methylenebisacrylamide (29:1 (w/w)) solution.

2.1.4. DNA oligonucleotides

Annealing of the appropriate oligonucleotide strands (Substrates for BcnI – DNA orientation FRET experiment, Substrates for BcnI - DNA conformation FRET experiment (Table 2)) was achieved by placing the tubes with the DNA solution into a thermocycler and cooling down from 95 °C to 20 °C with -1 °C/min rate. Equimolar amounts of complementary DNA strands were used for oligoduplex annealing; the final concentration of annealed DNA substrates was 1-2 μM.

^{33}P-phosphate radiolabel at the 5'-ends were introduced using [γ–^{33}P]ATP (Hartmann Analytic, Braunschweig, Germany) and T4 polynucleotide kinase. Pre-nicked oligonucleotide substrates (C-nick, and G-nick, Table 2), were made of three oligonucleotides: the 30 nt strand with a radiolabel at the 5′-terminus for the intact DNA strand, and two shorter (14-16 nt) unlabelled oligonucleotides for the nicked strand.

Table 2. Oligonucleotides and primers used in this study.

Sequence (5′ -> 3′)	Oligo's description	Purpose
5′-cttcgcagtacg**CCG**--**GG**caataacgcacgt-3′ 3′-gaagcgtcatgc**GGC**p **CC**gttattgcgtgca-5′	C-nick: 30 bp BcnI substrate with the pre-nicked C-strand. “p” marks 5′-terminal phosphate at the position of the nick	Preassembled nicked substrates
5′-cttcgcagtacg**CC** p**GGG**caataacgcacgt-3′ 3′-gaagcgtcatgc**GG**--**CCC**gttattgcgtgca-5′	G-nick: 30 bp BcnI substrate with the pre-nicked G-strand. “p” marks 5′-terminal phosphate at the position of the nick	
5′-cttcgcagtacg**CCGGG**caataacgcacgt-3′ 3′-gaagcgtcatgc**GGCCC**gttattgcgtgca-5′	DNA TRAP 30/30 oligoduplex: 30 bp cognate BcnI substrate used in DNA-trap experiments	Substrate for DNA trap experiment
5′-cgcacgactt**CCCGG**aagagcacgc-3′ 3′-gcgtgctgaa**GGGCC**ttctcgtgcgttg-5′	Specific oligoduplex	Substrates for EMSA experiments
5′-cgcacgacttgtcacaagagcacgc-3′ 3′-gcgtgctgaacagtgttctcgtgcgttg-5′	Unspecific oligoduplex	
5′-ggt**M**ttcagcgttattg**CCCGG**cgtactgcgagaaaagg-3′ 3′-ccaaaagtcgcaataac**GGGCC**gcatgacgctcttttcc-5′	C-DNA-Alexa546, M=dT-Alexa546	Substrates for BcnI – DNA orientation FRET experiment
5′-ggttttcagcgttattg**CCCGG**cgtactgcgagaaaagg-3′ 3′-ccaaaagtcgcaataac**GGGCC**gcatgacgctctt**M**tcc-5′	G-DNA-Alexa546, M=dT-Alexa546	
5′-ggttttcagcgttattgCCCGGcgtactgcgagaaaagg-3′ 3′-ccaaaagtcgcaataacGGGCCgcatgacgctcttttcc-5′	SP DNA	Specific oligoduplex for quantum yield and anisotropy measurements
5′-gctgacgcggagtatttggtat**CCCGG**ctctgctgaagccagttaccttcggaaacg-3′ 3′-cgactgcgcctcataaaccata**GGGCC**gagacgacttcggtcaatggaagcctttgc-5′	sp BcnI oligoduplex	Substrates for BcnI – DNA conformation FRET experiment
5′-ggtgacgcggagtatttggtatgattcctctgctgaagccagttaccttcggaaacg-3′ 3′-ccactgcgcctcataaaccatactaaggagacgacttcggtcaatggaagcctttgc-5′	nsp BcnI oligoduplex	
5′-**M**ttcagcgttattg**CCCGG**cgtactgcgagaaaagg-3′ 3′-aaagtcgcaataac**GGGCC**gcatgacgctcttttcc**B**-5′	C-DNA-Cy5, M=dT-Cy5, B=biotin	Oligoduplex for TIRF-based single-molecule FRET experiments
5′-**B**ggttttcagcgttattg**CCCGG**cgtactgcgagaaa-3′ 3′- ccaaaagtcgcaataac**GGGCC**gcatgacgctctt**M**-5′	G-DNA-Cy5, M=dT-Cy5, B=biotin	

See next page for Table 2 extension

Extension of the Table 2

ggt***gtT***cttgttatggattta**GCt**attgacc	C202A (TGT(Cys) -> **GCT**(Ser)) mutation direct primer, silent mutation V196V (GTC -> ***GTT***) removes PsyI target site	BcnI mutagenesis primers
cttaagtcttggtcaat**aGC**taaatccataac	C202A mutation reverse primer	
ggt***gtT***cttgttatggattta**tCt**attgacc	C202S (TGT(Cys) -> **TCT**(Ser)) mutation direct primer, silent mutation V196V (GTC -> ***GTT***) removes PsyI target site	
cttaagtcttggtcaat**aGa**taaatccataac	C202S mutation reverse primer	
acatgaaattaaa**TGt**aaagggtatctttca***gtG***ccgactgatatg	N18C (AAT(Gln) -> **TGT**(Cys)) mutation direct primer, silent mutation V24V (GTA -> ***GTG***) removes RsaI target site.	
gtcggCactgaaagatacccttt**aCA**tttaatttcatgtaatttattaac	N18C mutation reverse primer	
aaaccctgaa**TGC**atgaaaaaaaagtt***Att***tacaaccattaag	V105C (GTA(Val) -> **TGC**(Cys)) mutation direct primer, silent mutation L110L (TTG -> ***TTA***) removes Hpy8I target site.	
gtaaaTaacttttttttcat**GCA**ttcagggtttcgtgatg	V105C mutation reverse primer	
caagac***ttG***agt**TGC**agtaaaggaccacatg	K209C (AAA(Lys) -> **TGC**(Cys)) mutation direct primer, silent mutation L207L (TTA -> ***TTG)*** removes BspTI target site.	
ctttact**GCA**act***Caa***gtcttggtcaatac	K209C mutation reverse primer	
ggattacctcagcagaaagacggtggcgcat	PCR1 for primer	Oligonucleotides for 22.8 kb non-specific (PCR1+PCR2+Dig Handle PCR) DNA construct for single molecule translocation experiments
attgacgcgaccagcttcatgaatt	PCR1 rev primer (biotin)	
ggtaatcctcagcagaaagacggtggcgcat	PCR2 for primer	
cttcgcggccgcgaccagcttcatgaatt	PCR2 rev primer	
tgatatcgaattcctgcagcc	Dig Handle PCR for primer	
cagggtcggaacaggagagc	Dig Handle PCR rev primer	

See next page for Table 2 extension

Extension of the Table 2

Ggcctcagctcatgtcatcctcagcacacttgaccctcagct- cagctagcctcagcctacaatcacctcagcg	76 bp “replace” DNA fragment with 5 BbvCI sites.	Oligonucleotides for DNA construct for single DNA molecule hydrolysis experiments
Gatccgctgaggtgattgtaggctgaggctagctgagctgag- ggtcaagtgtgctgaggatgacatgagctga		
gaacgtcccgagaaaggaagggaagaaagc	pBluescript II SK+ “replace“ for primer with AvaI site	
aaaagctggagctccaccgcggtggcggcc	pBluescript II SK+ “replace“ rev primer with SacI site	
ttcatcctcgggttcctctatggtgctggt	T7 for primer with AvaI site	
ggaatcgccggcagcagccatagcctcagg	T7 rev primer with NgoMIV site	
ctcttccttttcaatattattg	Biotin Handle PCR pBluescript II SK+ for primer	
gctcactggccgtcgttttacaa	Biotin Handle PCR pBluescript II SK+ rev primer	
tgatatcgaattcctgcagcc	Digoxigenin Handle PCR pBluescript II SK+ for primer	
tttgtgatgctcgtcagggg	Digoxigenin Handle PCR pBluescript II SK+ rev primer	
tcagc**M**catgtcatcctcagcacacttgaccctcagctcagctagcctcagcctacaatcacc	Cy5 oligonucleotide (with M=T-Cy5)	
gaagtgCCCGGcaatacgtactgcgttagcagtacgtattg**CCGGG**ca	dhp 2xCCSGG substrate hp part with BcnI site.	BcnI substrates with two target sites.
ggcggtctcgcttctgctcttgctgg	dhp 2xCCSGG substrate universal dir primer	
gtattggtctcgcttccaagcacatcaccttgaatg	135 bp dhp 2xCCSGG substrate rev primer	
caaggtctctcttcgtctcattttgcatctcggc	535 bp dhp 2xCCSGG substrate rev primer	
tagcagtacgtattg**CCGGG**cacttctgctcttgctgg	ds 2xCCSGG substrate universal dir primer	
tagcagtacgtattg**CCGGG**cacttccaagcacatcaccttgaatg	135bp ds 2xCCSGG substrate rev primer	
tagcagtacgtattg**CCGGG**cacttcgtctcattttgcatctcggc	535bp ds 2xCCSGG substrate rev primer	

2.1.5. DNA plasmids

pBAD24-R.BcnI: ApR; araC promotor; pBAD24 cloning vector with cloned R.BcnI RE gene.

pACYC184-M.BcnIB: CmR; p15A replicon; pACYC184 cloning vector with cloned M.BcnIB methyltransferase gene.

T7 DNA

pBluescript SK+

pBluescript II SK+

2.1.6. Bacterial strains

BcnI mutant selection and over-expression experiments were done in Escherichia coli strain E. coli K12 ER2267: F´ proA+B+ lacIq Δ(lacZ)M15 zzf::mini-Tn10 (KanR)/ Δ(argF-lacZ)U169 glnV44 e14-(McrA-) rfbD1? recA1 relA1? endA1 spoT1? thi-1 Δ(mcrC-mrr)114::IS10

2.2. Methods

2.2.1. Electrophoresis

2.2.1.1. Denaturing (SDS) polyacrylamide gel electrophoresis of proteins

Denaturing SDS-PAGE of proteins was employed to verify homogeneity of BcnI proteins. Protein samples were mixed at 1:1 (v/v) ratios with the SDS loading solution and denatured at 95°C for 5 min. Polyacrylamide gels comprised of stacking and separation gel layers were used for protein electrophoresis (Sambrook et al., 1989). The stacking gel consisted of 4% “Acrylamide” solution I in PE1 buffer, while separating gel was 12-15% “Acrylamide” solution I in PE2

buffer (see 2.1.3.). Electrophoresis was run in PE3 buffer at room temperature for 1-1.5 hours at ~30 V/cm. Gels were stained with Page Blue protein staining solution (Thermo Fisher Scientific).

2.2.1.2. Non-denaturing electrophoresis through agarose

Separation of different DNA fragments or different forms of plasmid DNA was performed in 0.7-1.5 % agarose gels in the NBE buffer (see 2.1.3) supplemented with 0.5 μg/ml ethidium bromide. DNA samples were mixed with 1/3 volume of Non-denaturing loading dye solution (see 2.1.3) and electrophoresed at 3 V/cm until the bromphenol blue dye migrated for 3 cm. Digital images of the gels were taken with the BioDocAnalyze gel documenting system (Biometra, Goettingen, Germany).

2.2.1.3. Non-denaturing polyacrylamide gel electrophoresis

Non-denaturing polyacrylamide gel electrophoresis (PAGE) was employed in gel-shift experiments (see 2.2.4). The gels consisted of 8 % “Acrylamide” solution II in the EMSA running buffer (see 2.1.3), polymerisation was initiated by adding TEMED and ammonium persulfate. The gel dimensions (length×width×thickness) were 20×15×0.1 cm. Prior to gel casting, one of the glass plates forming the gel chamber was processed with “bind silane” (3-methacryloxypropyltrimethoxysilane) and the other with “repeal silane” (5 % (v/v) dichlorodimethylsilane in $CHCl_3$).

Equal volumes of radiolabelled DNA samples and Non-denaturing loading dye solution (see 2.1.3.) loaded on the gel. Electrophoresis was run at room temperature for 2-3 hours at ~6 V/cm. After electrophoresis the glass plate treated with “repeal silane” was removed and the gel was dried on the other glass plate under a hot air flow. Radiolabelled DNA was detected in the dried gels using BAS-MS image plates (FujiFilm) and Cyclone phosphorimager (Perkin Elmer,

Wellesley, MA, USA). The amounts of various DNA fragments were quantified with OptiQuant 3.0 software (Perkin Elmer, Wellesley, MA, USA).

2.2.1.4. Denaturing polyacrylamide gel electrophoresis

Denaturing PAGE was used to separate oligonucleotide DNA cleavage products (see 2.5). Electrophoresis was performed in TBE buffer (see 2.1.3.). The standard 20×15×0.1 cm gels consisted of 20 % “Acrylamide” solution II (see 2.1.3.) supplemented with 8.5 M urea in the same buffer.

Samples of radiolabelled DNA were mixed 1:1 (v/v) with Non-denaturing loading dye solution (see 2.1.3), placed for 4 min into a hot (95°C) water bath and then placed on ice. Electrophoresis was run for ~1 hour at 30 V/cm without the samples and for another 3-4 h with the DNA samples.

Some samples were analysed on high resolution denaturing polyacrylamide gels (gel dimensions, length × width × thickness, 50×20×0.02 cm). Gel composition was the same as described above. Electrophoresis was run for 30 min at 50 V/cm without the samples and for another 2 hours with the DNA samples. During electrophoresis, the gel was thermostated at 60°C. Radiolabelled DNA was detected as described in 2.2.1.3.

2.2.2. Design, preparation and purification of BcnI mutants for fluorescent labelling

2.2.2.1. Labelling position and introduction of Cys mutations

Labelling positions on BcnI where determined by measuring distances between two residues on different subdomains. Results where compared between apo BcnI (PDB ID 2ODH) and BcnI-DNA complex (PDB ID 2ODI). Position pairs which encompass theoretical Alexa488-Alexa546 R_0 and has biggest distance differences were chosen (see 3.2.2., Table 3). N18C+C202S,

V105C+C202S, C202S+K209C and N18C+V105C+C202S mutants of BcnI were obtained by modified QuickChange mutagenesis protocol (Zheng, 2004). Fifteen cycles of inverse PCR were performed using pBAD24_R.BcnI plasmid (Kostiuk et al., 2011) as a template, a pair of inverse primers with the designed mutation (Table 2) in the overlapping region, and Pfu DNA polymerase. Following DpnI digestion of the template DNA, the amplified DNA was used for transformation of Escherichia coli host by $CaCl_2$ method (Sambrook et al., 1989). Sequencing of the entire *bcnIR* gene of each mutant confirmed that only the designed mutation had been introduced.

2.2.2.2. Overexpression of BcnI Cys mutants

To express BcnI REase, the *E. coli* K12 ER2267 strain containing the pACYC184_MB.BcnI was transformed with pBAD24_R.BcnI. Cells were grown in LB medium with appropriate antibiotics at 37 °C to A_{600} 0.7 and protein expression induced by addition of arabinose to the final concentration of 0.2 %. After 4 h of induction, the cells were harvested by centrifugation and the pellet was stored at −20 °C.

2.2.2.3. Purification wt BcnI and mutants

Frozen cells expressing BcnI REase were thawed and resuspended in Buffer A+0.1 (see 2.1.3.) supplemented with 7 mM 2-ME. The cell suspension was disrupted by sonication and the cell debris was removed by centrifugation at 35000 g for 1 h. BcnI was purified by subsequent chromatography on phosphocellulose P11 column (Whatman), Blue Sepharose and Heparin Sepharose (Amersham Biosciences) columns using linear NaCl gradients (Buffer A+0.2 and Buffer A+1 supplemented with 7 mM 2-ME (see 2.1.3.)) for protein elution. All purification steps were monitored by SDS-PAGE (see 2.2.1.3.). Fractions

containing BcnI REase activity were pooled and dialyzed against Storage buffer (see 2.1.3.) and stored at −20 °C.

2.2.3. Fluorescent protein labelling

2.2.3.1. Single labelling

To remove glycerol and DTT, solution of the selected BcnI cysteine mutant (BcnI(N18C+C202S), BcnI(V105C+C202S) or BcnI(C202S+K209C)) in the Storage buffer was diluted 2-fold with the Labelling buffer (see 2.1.3.). BcnI proteins where concentrated in Amicon Ultra 10 k centrifugal filters (10000 MWCO) 5 times from 500 µl to 50 µl, between concentrations 450 µl of the Labelling buffer was added. Labelling was performed in the Labelling buffer using 20 µM BcnI and 10 or 20 times molar excess of AlexaFluor488-C_5-maleimide (ThermoFisher Scientific), AlexaFluor546-C_5-maleimide (ThermoFisher Scientific) or Cy3MonoMaleimide (GE Healthcare) fluorescent dyes, reaction mixture was incubated 2 h at 25 °C and stopped adding 40 µM of 2-ME. Conjugates where purified applying the reaction mix on Heparin HP (GE Healthcare) column. Free dye was eluted with Buffer A+0.2 and conjugate was eluted with Buffer A+1. Conjugate was concentrated against BcnI Storage buffer and labelling efficiencies were calculated as described in 2.2.3.3. A similar procedure was performed to obtain biotinylated BcnI using BcnI(V105C+C202S) and maleimide-PEG_2-biotin (Thermo Fisher Scientific).

2.2.3.2. Double labelling

For double labelling, glycerol and DTT from BcnI(N18C+V105C+C202S) protein stock was removed similarly as for single labelling (see 2.2.3.1.). First labelling was performed mixing 20 µM BcnI(N18C+V105C+C202S) with 40 µM of AlexaFluor488-C_5-maleimide (ThermoFisher Scientific), reaction mixture was

incubated 2 h at 25 °C and stopped adding 40 µM of 2-ME. Unlabelled protein, single-labelled protein, and double-labelled protein were separately eluted from a Mono-S ion exchange chromatography column (GE Healthcare) using a long (40 column volumes) 250-550 mM NaCl gradient. The single-labelled protein was used in the second labelling reaction with a 10-fold molar excess of AlexaFluor546-C_5-maleimide (ThermoFisher Scientific). The protein concentration and the labelling efficiency (see 2.2.3.3.) were measured by UV-VIS absorption spectroscopy. After the reaction was stopped with 2-ME, double-labelled conjugate was purified and stored as described in 2.2.3.1.

2.2.3.3. Determination of the labelling efficiency

Labelling efficiencies were determined from absorption measurements employing Lambert-Beer law. Concentrations of dyes ($c_{488,s}$ – c(Alexa488 on single-labelled BcnI proteins), $c_{488,d}$ – c(Alexa488 on double-labelled protein), $c_{546,d}$ – c(Alexa546 on double-labelled protein)) and proteins ($c_{BcnI,s}$ – single-labelled BcnI, $c_{BcnI,d}$ – double-labelled BcnI) were calculated using equations (30) to (34). Labelling efficiencies were calculated as the ratio of the dye and the corresponding protein concentrations (e.g., $c_{488,s}/c_{BcnI,s}$ for the single-labelled protein, $c_{488,d}/c_{BcnI,d}$ and $c_{546,d}/c_{BcnI,d}$ for the double-labelled protein):

$$c_{488,s} = \frac{A_{495}}{\varepsilon_{495} * d} \quad (30)$$

$$c_{BcnI,s} = \frac{A_{280} - 0.11 * A_{495}}{\varepsilon_{BcnI} * d} \quad (31)$$

$$c_{488,d} = \frac{A_{495} - 0.11 * A_{556}}{\varepsilon_{495} * d} \quad (32)$$

$$c_{546,d} = \frac{A_{556}}{\varepsilon_{556} * d} \quad (33)$$

$$c_{BcnI,d} = \frac{A_{280} - 0.11 * A_{495} - 0.12 * A_{556}}{\varepsilon_{BcnI} * d} \quad (34)$$

where A_x and ε_x is absorption and extinction coefficient ($M^{-1} \times cm^{-1}$) at x nm wavelength, d=1 cm. All labelled proteins are listed in Table 6 and Figure 17.

2.2.4. Preparation and purification of DNA substrates

2.2.4.1. DNA construct for the observation of BcnI sliding and jumping

The unspecific DNA construct for single molecule diffusion experiments was made by ligating two PCR fragments amplified from T7 phage DNA and digoxigenin-modified handle (Dig-handle) to form a 22.8 kbp nonspecific construct (no recognition sites for BcnI) as depicted in Figure 8A. One of the PCR products was modified at the 5′ end with biotin using a biotinylated primer. The ligation of two PCR products was done using overhangs from Nt.BbvCI digestion. The overhangs from NotI digestion were used for ligation of the Dig-handles (Table 2).

2.2.4.2. DNA construct for single molecule DNA hydrolysis experiments

A 7.4 kb DNA construct suitable for direct observation of DNA cleavage using magnetic tweezers was made by ligating a 5.9 kb PCR product (template – T7 DNA), a 450 bp PCR product (template – pBluescriptIISK+) and two PCR products modified with either biotin or digoxigenin (template – pBluescriptIISK+), serving as Biotin- and Dig-handles, respectively (Figure 8B, Table 2).

2.2.4.3. Construction of BcnI substrates with two target sites

The two-site DNA substrates “135” (100 bp between BcnI sites) and “535” (500 bp between BcnI sites) were made by ligation of Eco31I-digested and gel-purified PCR products (using φX174 phage DNA as template) with [γ-^{33}P]-ATP-phosphorylated hairpin oligonucleotides (Figure 8C, Table 2). The non-ligated fragments were removed by incubating the reaction mixtures with T7 polymerase. T7 polymerase has strong 3′=>5′ exonuclease activity, which degrades all DNA fragments with free 3′-ends. Only the ligated di-hairpin DNA substrates with 2 BcnI recognition sites remain. The final substrates were gel-purified from 1 % agarose gel (see 2.2.1.2.) in TAE buffer (see 2.1.3.).

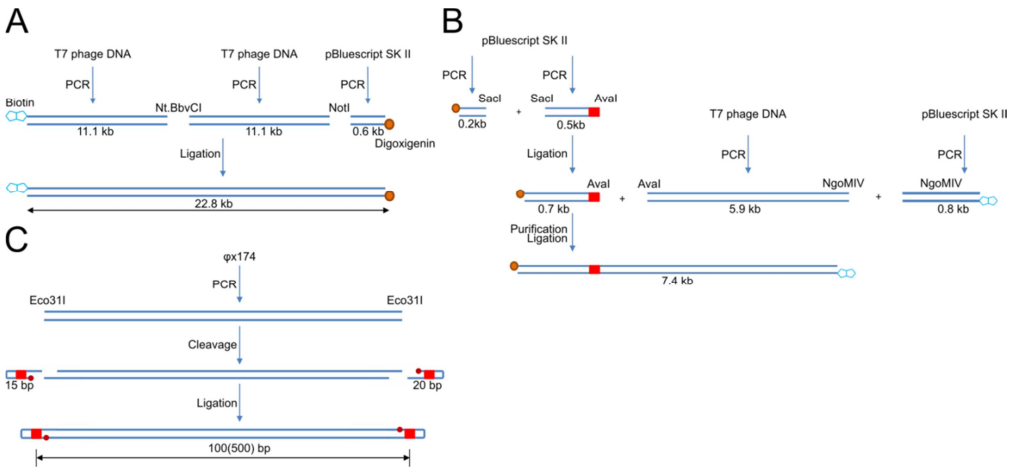

Figure 8. DNA constructs. (A) 22.8 kbp nonspecific DNA construct used in the study of BcnI sliding and jumping on the DNA. (B) 7.4 kbp DNA construct used in the single molecule DNA cleavage experiments. (C) Radiolabelled 135 and 535 bp 2×CCSGG di-hairpin DNA substrates used in the BcnI processivity measurements, 33P-phosphate is depicted as a dark red circle. The BcnI specific site is depicted as a red rectangle (A-C).

2.2.5. DNA binding studies

DNA binding by BcnI Cys mutants was analysed by the gel mobility-shift assay, using natural SP (specific) ^{33}P-labelled DNA substrates (Table 2). Oligonucleotide duplexes (0.1 nM) were incubated with different amounts of

proteins in the Binding buffer (see 2.1.3) in a total volume of 20 µl for 15 min at room temperature. Free DNA and protein-DNA complexes were separated by non-denaturing polyacrylamide gel electrophoresis as described in 2.2.1.3.

K_D values for cognate oligonucleotide binding by BcnI enzymes were calculated by fitting binding data to equation (35) (Tamulaitis et al., 2006):

$$y = \frac{\{s_o - x - K_D + [(s_o + x + K_D)^2 - 4 * s_o * x]^{0.5}\}}{2} \quad (35)$$

where y is the free DNA concentration (in terms of nM) at each protein concentration x, s_0 is the DNA concentration in binding mixture, and K_D is the dissociation constant of protein-DNA complex. Data were analysed using the KYPLOT 2.0 software.

2.2.6. BcnI kinetic experiments

2.2.6.1. Reactions with supercoiled DNA

Rapid single turnover reactions on the supercoiled phiX174 DNA were carried out at 25°C in a Kin-Tek RQF-3 quench-flow device. For pre-mix reactions, which were started by adding Mg^{2+} to a solution containing both enzyme and DNA, enzyme was preincubated with the phiX174 DNA substrate in the Reaction buffer (see 2.1.3.) supplemented with 0.1 mg/ml BSA before mixing with an equal volume (16 µl) of 20 mM $Mg(OAc)_2$ in the same buffer. For post-mix reactions starting with enzyme and DNA in separate solutions, 16 µl of BcnI with 20 mM $Mg(OAc)_2$ were mixed with an equal volume of DNA substrate. After a chosen time delay, the reactions were quenched by mixing with 6 M guanidinium chloride. The recovered samples (approximately 100 µl) were mixed with 60 µl of Non-denaturing loading dye solution (see 2.1.3) and electrophoresed through agarose (see 2.2.1.2.).The final pre-mix and post-mix reactions contained 2 nM phiX174 DNA, 200 nM enzyme and 10 mM magnesium acetate.

Alternatively, the magnesium acetate solution used for the pre-mix reactions was supplemented with 4 μM of DNA trap (30/30) (Table 2) or 16 μM of protein trap (BcnI mutant D55A). DNA was recovered by alcohol precipitation and analysed by electrophoresis through agarose as described (see 2.2.1.2.).

Cleavage of phiX174 RFL double-stranded DNA follows the first-order consecutive reaction equation (36). The expressions for the time courses of SC (initial supercoiled substrate), OC (open circular reaction intermediate) and FLL (full-length linear product) forms (equations (37)-(39)) were simultaneously fitted to the corresponding experimental data giving the optimal values for the rate constants k_1 and k_2:

$$SC \xrightarrow{k_1} OC \xrightarrow{k_2} FLL \quad (36)$$

$$[SC] = [SC]_0 \times exp(-k_1 \times t) \quad (37)$$

$$[OC] = [OC]_0 \cdot \left(\frac{k_1}{k_1 - k_2}\right) \cdot \{exp(-k_2 \cdot t) - exp(-k_1 \cdot t)\} \quad (38)$$

$$[FLL] = [SC]_0 - [SC] - [OC] \quad (39)$$

Multiple-turnover cleavage reactions were performed at 25°C with 2 nM phiX174 DNA and 0.1 nM wt BcnI in the Reaction buffer (see 2.1.3.) supplemented with 0.1 mg/ml BSA. Reactions were started with 20 mM $Mg(OAc)_2$ and aliquots (25 μl) were removed at timed intervals, quenched by adding 8 μl of Non-denaturing loading dye solution (see 2.1.3) and electrophoresed through agarose (see 2.2.1.2.).

The amounts of supercoiled, open-circular and linear forms of the plasmid were quantified using 1D Main software (Advanced American Biotechnology, Fullerton, CA, USA). Multiple-turnover cleavage data sets were fitted to linear equation. Regression analysis used KyPlot 2.0 software (Yoshioka, 2002).

2.2.6.2. Kinetics experiments with oligonucleotide substrates

Single turnover reactions on preassembled nicked oligonucleotide substrates were performed in the pre-mix experimental conditions. 4 nM of radiolabelled 30 bp G-nick or 30 bp C-nick DNA substrates (see 3.1.2., Table 2) were preincubated with 200 nM or 400 nM BcnI(wt) in the Reaction buffer (see 2.1.3.) supplemented with 0.1 mg/ml BSA and reaction was initiated by adding $Mg(OAc)_2$ (final concentration 10 mM). Reactions were carried out at 25°C in a Kin-Tek RQF-3 quench-flow device. After a chosen time delay, the reactions were quenched by mixing with 2 M HCl. The recovered samples (approximately 100 µl) were mixed with 45 µl of Neutralization solution (3.5 M Tris and 3 % SDS) and 60 µl of Denaturing loading dye solution (see 2.1.3.). Reaction products were separated by high resolution denaturing PAGE (see 2.2.1.4.). Radiolabelled DNA was detected and quantified by phosphorimager (see 2.2.1.3.).

The amounts of various DNA fragments were quantified using OptiQuant 3.0 software (Perkin Elmer, Wellesley, USA). Single-turnover cleavage data sets were fitted to single exponential equations, respectively. Regression analysis used KyPlot 2.0 software (Yoshioka, 2002).

2.2.6.3.Steady-state kinetic experiments with double-site substrates

Steady state reactions were performed by manually mixing 1 nM BcnI(wt) with the solution of 100 nM unlabelled 135 or 535 bp 2xCCSGG DNA duplex in Reaction buffer (see 2.1.3.) supplemented with 0.1 mg/ml BSA and 10 mM $Mg(OAc)_2$, the reaction mixture contained 1/5 volume of purposive 5′-[γ-^{33}P]-ATP labelled 135 or 535 bp 2xCCSGG DNA di-hairpin. Samples (8 µl) were collected at timed intervals, quenched by mixing with 14 µl Non-denaturing

loading dye solution (see 2.1.3.) and electrophoresed through 6 % “Acrylamide” solution II (see 2.1.3.) gel 20 h at 110 V. Radiolabelled DNA was detected as described in 2.2.1.3. Rate constants of substrate cleavage (SS), accumulation of single cleaved product (PS) and doubly cleaved product (PP) were evaluated by linear fitting. Using these constants we also calculated processivity or fraction of BcnI molecules that cut both targets during single binding event: $k(PP_{accumulation})/(k(PS_{accumulation})+k(PP_{accumulation}))$. The given expression equals to $k(PP_{accumulation})/k(SS_{cleavage})=|v_{PP}/v_{SS}|$.

2.2.7. Fluorescence anisotropy measurements

Anisotropies of fluorescently labelled BcnI proteins (see 2.2.3.1.) were measured at constant wavelength analysis mode (λ_{ex}=480 nm, λ_{em}=515 nm) with integration time of 5s with fluorimeter Fluoromax3. We used 0.5 μM of labelled BcnI or labelled DNA oligoduplex, measurements were performed in Reaction buffer (see 2.1.3.). The fluorescence anisotropy (r) was calculated according to equations (40)-(41):

$$r = \frac{I_{VV} - GI_{VH}}{I_{VV} + 2GI_{VH}} \quad (40)$$

$$G = \frac{I_{HV}}{I_{HH}} \quad (41)$$

where I_{VV} is the vertically polarized fluorescence intensity excited with vertically polarized light, I_{VH} is the horizontally polarized fluorescence intensity excited with vertically polarized light. I_{HV} is the vertically polarized fluorescence intensity excited with horizontally polarized light, and I_{HH} is the horizontally polarized fluorescence intensity excited with horizontally polarized light (Lakowicz, 2006). Anisotropy values are listed in Table 6.

2.2.8. Determination of the Förster radius (R_0)

2.2.8.1. Fluorescence quantum yield φ_D

Quantum Yield of labelled BcnI proteins were measured in the Reaction buffer (see 2.1.3.) using fluorimeter Fluoromax3 and spectrophotometer Nicolet Evolution 300 as described in instruments manual. Fluorescein (0.1 M NaOH) and Rhodamin6G (H_20) solutions were used as standards for QY measurements for Alexa488 (λ_{ex}=480nm, λ_{em}=495-600 nm) and Alexa546 (λ_{ex}=510 nm, λ_{em}=525-630 nm) labelled BcnI proteins. Gradients from integrated fluorescence intensity vs. absorbance were calculated and quantum yields were calculated using (42) equation:

$$\phi_X = \phi_{ST}\left(\frac{Grad_X * n_X^2}{Grad_{ST} * n_{ST}^2}\right) \quad (42)$$

where the subscripts *ST* and *X* denote standard and test respectively, Φ is the fluorescence quantum yield, *Grad* the gradient from the plot of integrated fluorescence intensity *vs* absorbance, and n the refractive index of the solvent.

2.2.8.2. J overlap integral calculation

The overlap integral ($J(\lambda)$) expresses the degree of spectral overlap between the donor emission and the acceptor absorption (see eq. (43)):

$$J(\lambda) = \frac{\sum_{i=495}^{700} F_D * F_D(\lambda_i) * \varepsilon_A(\lambda_i) * \lambda_i^4}{\sum_{i=495}^{700} F_D(\lambda_i)} \quad (43)$$

where $F_D(\lambda)$ is the fluorescence intensity of the donor at the wavelength λ. $\varepsilon_A(\lambda)$ is the extinction coefficient of the acceptor at λ.

2.2.8.3. Förster radius (R_0) calculation

FRET efficiency strongly depends on the distance between donor and acceptor (see eq. (44)). Förster radius (R_0) is the distance between fluorophore

donor and acceptor at which FRET efficiency is 0.5 half the donor molecules decay by energy transfer and half decay by the usual radiative and non-radiative rates. R_0 values were calculated by equation (45).

$$E = \frac{r^6}{r^6 + R_0^6} \quad (44)$$

$$R_0 = \sqrt[6]{\frac{9000 * ln10}{128\pi * N_A} * \phi_D * \kappa^2 * n^{-4} * J} \quad (45)$$

where N_A is the Avogadro's number, φ_D - the donor quantum yield, κ^2 - the dipole orientation factor, n the refractive index of the medium, and J the overlap integral of the fluorescence and absorption spectra of donor and acceptor dyes. The dipole orientation factor was assumed to be 2/3 (equivalent to free rotation of the fluorophores (Stryer, 1978)). The refractive index of the media (n=1.34) was measured experimentally. The determined φ_D and R_0 values are listed in Table 6.

2.2.9. Preparation of experimental cells

2.2.9.1. Preparation of capillary for BcnI facilitated diffusion experiments.

Cleaning, etching and activation of the glass surface. Capillaries (ViroCom) put in the teflon holder and placed in the glass box (heated 2 h at 200 °C before use), then covered with 80 % EtOH, sonicated for 3 min and sediment for 3 min at RT. Transferred into acetone bath teflon holder with capillaries were soaked for 30 min, sonicated for 10 min and rinsed for 1 min in the bath with ddH_2O. Then in the bath with 2 % Hellmanex solution (Hellma Analytics) capillaries were sonicated for 20 min at 50 °C, rinsed with ddH_2O for 2 min and incubated in Pirahna solution (9 % H_2O_2 + 49 % H_2SO_4) for 1 h at 60 °C. After washing with ddH2O, glass surface of capillaries were activated in

0.1 M KOH for 10 min. After this step, capillaries can be stored in water, when they are to be used, they need to be activated in KOH again.

Coating of the glass surface with polystyrene. Two capillaries were dried from residual water with N_2 and mounted in the homebuilt spin coater. Capillaries were filled with 1 % 35 kDa polystyrene solution in toluene (immediately made from 10 % solution in THF) and spinned for 30 s at 3000 rpm/min, then capillaries were exposed to UV on transilluminator for 5 min at full power.

Assembly of the flow cell. To assemby the flow cell the ends of the each capillary are connected to microlader pipet tips (Eppendorf), which are inserted into the capillary. The connection point between the capillary and the pipet tip is sealed with a flexible silicon-glue (Elastosil E41, Wacker Chemie AG). The inlets of the microloader pipet tips are locked with silicon-glue sealed 10 µl pipet tips. After curing of the silicon-glue the capillary flow cell should rest 2 days at 4 °C before it is used.

2.2.9.2. Preparation of sample chamber for single DNA molecules hydrolysis assay

Cleaning, etching and activation of the glass surface. Put the glass slides (Thermo Fisher Scientific Gerhard Menzel) into the teflon holder, fill in half slides with holes and half without holes. Rinse glass slides with deionized water for 2 min, and then treat slides with Helmanex, Pirahna and KOH as in 2.2.9.1.

Coating of the glass surface with polystyrene. Spin clean cover slides (without holes) at 6000 rpm. Take 50 µl of 1 % 35 kDa polystyrene solution (see 2.2.9.1.) in the glass Pasteur pipette, pipette very fast on the spinning glass and immediately take away the pipette to prevent additional drops from the tip, continue to spin 60 s. Bake the polystyrene layer at 150 °C for 1 h.

Assembly of the flow cell. Put the layer of Parafilm between the glass with holes and the coated glass. Put a thicker glass on a heat plate at 150 °C. Put the

flow cell with holes downside to prevent break during working. Heat the flow cell, beginning at one end until the Parafilm becomes transparent. Carefully press with q-tip on the flow cell to prevent encapsulated air bubbles.

2.2.9.3. Preparation of PEGylated sample chamber for TIRF-based single-molecule FRET experiments.

Cleaning slides. Fill the glass containers with acetone and sonicate for 15 min, dispose of acetone and rinse the container 4-5 times with ddH_2O. Place the teflon holder with glass slides (Thermo Fisher Scientific Gerhard Menzel) (with and without holes) into the glass container, fill with 5 M KOH and sonicate for 20 min. Rinse the glass slides 3 times with ddH_2O, 2 times with methanol to remove KOH and dry them with N_2. Burn the cover slips with propane each side for a few seconds, and put them back in the new glass container (sonicated with methanol for 10 min).

Aminosilanization and PEGylation. Pour 150 ml of methanol into the 200 ml flask (sonicated with methanol for 10 min). Add 7.5 ml of acetic acid with glass pipette and 1.5 ml of N-(2-Aminoethyl)-3-aminopropyltrimethoxysilane (Sigma-Aldrich) with a glass pipette with low speed into the flask and mix well. Pour the mixture into the container with glass slides without holes, incubate for 10 min, sonicate for 1 min and incubate for additional 10 min. Then rinse the glass slides with methanol, water, methanol and dry them with N_2. Place the cover slips inside the tip box, on top of the tips arranged to be on four corners of the slides. Fill in the bottom part of the box with distilled water. Dilute 1-2 mg of biotin-PEG (α-Biotinyl-ω-NHS esther PEG (Mw(PEG)=5000 Da, RAPP Polymere)) and 120 mg of mPEG (α-Methoxy-ω-NHS esther PEG (Mw(PEG)=5000 Da, RAPP Polymere)) in the 480 µl of 100 mM $NaHCO_3$ (pH=8.5) in 1.5 ml Eppendorf tube, spin solution 1 min at 10000 rpm. Put 70 µl of PEG solution on

one cover slip. Place second cover slip gently on top of it. Incubate for 2-3 h or overnight. After incubation period, disassemble the slides, rinse them with plenty of H_2O and dry completely with N_2. Store the slides in the freezer.

Assembly of the flow cell. Flow cells were assembled as described in 2.2.9.2.

2.2.10. FRET data analysis

The FRET efficiency is defined as the rate of energy transfer from the donor to the acceptor divided by the rates of all processes that bring an excited donor back to the ground state. In confocal FRET measurements the donor fluorophore is excited, and two fluorescence intensities are measured simultaneously: (i) the donor intensity I_{DD} (for donor excitation) and (ii) the acceptor intensity I_{DA} (for donor excitation). In order to obtain a real FRET efficiency (according to its definition) from the measured acceptor and donor intensities, one has to consider the non-specific fluorescent background (e.g. dark count rate, autofluorescence of sample cell, etc), the 'cross talk' between the donor and acceptor channels (correction factors α, β, see below), direct acceptor excitation (correction factor δ), and the different quantum yields of donor and acceptor fluorophores as well as different detection efficiencies (both combined in the correction factor γ) (Gust et al., 2014; Hohlbein et al., 2014; Theissen et al., 2008).

2.2.10.1. Background correction:

All measured intensities where corrected for fluorescent background. The background was determined by measuring for a given excitation-emission configuration a sample that contained buffer only (e.g. no labelled DNAs nor proteins). The obtained intensities I_{DD}^{buffer}, I_{DA}^{buffer} and in case of acceptor excitation

I_{AD}^{buffer} as well as I_{AA}^{buffer} (for donor and acceptor detection, respectively) were subtracted from the measured intensities of a particular protein/DNA sample at the same excitation/detection conditions. In the following, intensities without background correction are denoted as I^* and intensities with background correction as I.

2.2.10.2. Fluorescence cross-detection factors α and β.

Photons emitted from the donor and from the acceptor fluorophore and collected by the objective are separated by a dichroic beam splitter and are assigned to either donor or acceptor signal. This discrimination is however not perfect due to an overlap of the emission spectra of the two dyes and non-ideal separation of emitted photons into the detection channels by the beam splitter. This leads to cross-detection (cross-talk), i.e. that photons that were emitted by the donor are detected in the acceptor channel and *vice versa*.

The relative amount of cross-detection α of donor emission in the acceptor channel was determined by exciting a donor-only sample at the donor wavelength and measuring the intensities in both detection channels. α is then provided by eq. (46):

$$\alpha = \frac{I_{DA}^{*Donly} - I_{DA}^{buffer}}{I_{DD}^{*Donly} - I_{DD}^{buffer}} \quad (46)$$

Similarly, the relative amount of cross-detection β of the acceptor emission seen in the acceptor channel was determined by exciting an acceptor-only sample at the acceptor wavelength and measuring the intensities in both detection channels. β is then provided by eq. (47):

$$\beta = \frac{I_{AD}^{*Aonly} - I_{AD}^{buffer}}{I_{AA}^{*Aonly} - I_{AA}^{buffer}} \quad (47)$$

2.2.10.3. Correction for direct excitation of the acceptor: correction factor δ.

The correction for direct excitation is defined as the ratio of the acceptor excitation rate and the donor excitation rate when using the donor excitation wavelength. It is thus the ratio of the extinction coefficients ε_D^{Aonly} and ε_D^{Donly} of the acceptor only and the donor only sample at the donor excitation wavelength. It can be obtained from the absorbance spectra of the acceptor- and donor-only samples and equals the ratio of the absorbance values A_D^{Aonly} and A_D^{Donly} of the acceptor only and the donor only sample at the donor excitation wavelength normalized by the respective fluorophore concentrations (eq. (48)):

$$\delta = \frac{\varepsilon_D^{Aonly}}{\varepsilon_D^{Donly}} = \frac{A_D^{Aonly}/c_{Aonly}}{A_D^{Donly}/c_{Donly}} \quad (48)$$

2.2.10.4. Correction for differences in quantum yield and detection efficiency: correction factor γ.

The parameter γ corrects for different quantum efficiencies of donor and acceptor fluorophores and different detection efficiencies of emitted fluorescence (eq. 49). It can be determined by exciting an acceptor only and a donor only sample at the donor wavelength and measuring the corresponding acceptor I_{DA}^{*Aonly} and donor I_{DD}^{*Donly} emission intensity, respectively. γ is then the ratio of both intensities corrected for the different excitation rates of the two dyes at the donor wavelength:

$$\gamma = \frac{I_{DA}^{*Aonly} - I_{DA}^{buffer}}{I_{DD}^{*Donly} - I_{DD}^{buffer}} * \delta^{-1} \quad (49)$$

The correction factors were determined by measuring the required samples at the conditions indicated above and using the provided formulas.

With these correction factors, the FRET efficiency of a dual labelled sample (containing both acceptor and donor) can be calculated from the background corrected intensities of acceptor and donor emission upon donor excitation I_{DA} and I_{DD} according to eq. (50):

$$E_{FRET} = \frac{(I_{DA} - \alpha * I_{DD}) - \gamma\delta(I_{DD} - \beta * I_{DA})}{(I_{DA} - \alpha * I_{DD}) + \gamma(I_{DD} - \beta * I_{DA})} \quad (50)$$

2.2.11. BcnI single-molecule FRET experiments

2.2.11.1. Confocal single-molecule FRET experiments

The studies of the binding orientation at the target site were performed using the single-labelled BcnI variants BcnI(N18C+C202S)-Alexa488, BcnI(V105C+C202S)-Alexa488, and BcnI(C202S-K209C)-Alexa488, as well as the single-labelled oligonucleotide duplexes Alexa546-C-DNA and Alexa546-G-DNA (Supplementary Table S1). 50 µl reactions contained 50 pM protein together with 50 pM oligoduplex in the Reaction buffer (see 2.1.3.) supplemented with 10 mM $Ca(OAc)_2$. The conformational states of BcnI were measured using 25-50 pM of double-labelled BcnI(N18C+V105C+C202S)-Alexa488-Alexa546 and 1-10 nM of specific (SP) and non-specific (NSP) DNA (Table 2) in the Reaction buffer (see 2.1.3.) with or without 10mM $Ca(OAc)_2$. FRET measurements were performed using an inverted Zeiss LSM 780 confocal microscope equipped with a Confocor 3 unit allowing simultaneous dual-color fluorescence detection. Single BcnI-DNA complexes freely diffusing in solution were excited with a 488 nm laser (using the built in beam splitter MBS 488/561). The emission signal was simultaneously separated on a ‘donor’ and an ‘acceptor’ channel using a 565 nm dichroic mirror. The signals of the donor and the acceptor channels were additionally cleaned up using a 525±30 nm band-pass filter and a 580 nm long-pass filter, respectively. Raw data sets were corrected as described in 2.2.10.

Obtained FRET values were plotted as histograms and multiple Gaussian distributions were fitted to the data (Figure 18, Figure 22, Table 7).

2.2.11.2 TIRF-based single-molecule FRET experiments

TIRF-based single-molecule FRET experiments were performed in the flow cells coated with biotinylated-polyethylene-glycol (Roy et al., 2008) with a combined magnetic tweezers-FRET instrument (Kemmerich et al., 2015). Flow cell was incubated with 1 mg/ml streptavidin for 30 min, then washed with 1 ml of PBS buffer (see 2.1.3.) and with 200 µl of the Measurement buffer (see 2.1.3.) with 10 mM $Ca(OAc)_2$. 50 µl of 0.1 nM Cy5-labelled biotinylated DNA oligoduplexes (Table 2) were incubated in the flow cell for 20 min to allow DNA attachment to the flow cell surface. Detached DNA was washed from the flow cell with 1 ml of PBS buffer and 200 µl of the Measurement buffer. Positions of attached Cy5-labelled DNA molecules were determined by illuminating the flow cell with 43 mW 642 nm laser, then the flow cell was illuminated with 50 mW 532 nm laser and 0.1-0.2 nM of BcnI(N18C+C202S)-Cy3-maleimide were injected. The emissions of the Cy3 and Cy5 fluorophores were spectrally separated using a 635 nm dichroic mirror and were projected on either half of the chip of an iXon 897-D EMCCD camera (Andor, Belfast, Ireland). Data collection was controlled using custom software written in LabView (National Instruments, Austin, United States). Single-molecule FRET traces were extracted from the fluorescence images with MATLAB (MathWorks, Natick, United States). 2-D Gaussian distributions were fitted to Cy3 and Cy5 fluorescence signals that co-localize with the initially detected positions of DNA molecules and the obtained single-molecule FRET traces were corrected for the background and for α, β, γ, δ correction factors (see 2.2.10.).

2.2.11.3. Single-molecule observation of BcnI binding on stretched DNA

Single-molecule binding experiments on stretched DNA, including the flow cell preparation, the combined TIRF-magnetic tweezers setup and the data analysis have been previously described in detail (Schwarz et al., 2013). To enable prolonged observation of fluorescent enzyme molecules, experiments were performed using the BcnI(V105C+C202S)-Maleimide-PEG2-Biotin conjugate labelled with streptavidin-coated quantum dots (Qdot®625 Streptavidin Conjugate, diameter 20 nm, Molecular Probes, Life Technologies) and a 22.8 kbp DNA construct devoid of BcnI sites (Figure 8A). The DNA construct was preincubated with streptavidin-coated 1 µm magnetic beads (Dynabeads MyOne Streptavidin C1, ThermoFisher Scientific) and immobilized on the antidigoxigenin-covered bottom surface of the flow cell consisting of a capillary with a quadratic cross section (VitroCom). Subsequently, the DNA was stretched with a magnet in almost parallel orientation to the glass surface (Figure 19 A). The small tilt angle arising from the attached magnetic bead was approximately 5°, such that its influence on the measured enzyme displacement can be neglected. The sample was excited with a 10 mW 488 nm laser in total internal reflection geometry. After injection of 0.1-0.2 nM Qdot-labelled BcnI the binding and diffusion events of single BcnI molecules on DNA were recorded. The measurements were carried out in the Reaction buffer supplemented with 0.02 mg/ml glucose oxidase, 0.008 mg/ml catalase, 20 mM glucose, 0.1 mg/ml BSA and 14 mM 2-ME. The positions of individual BcnI molecules bound to DNA were obtained from raw image data using the FIESTA software (Ruhnow et al., 2011). 1D diffusion coefficients were calculated from the mean square displacement of the enzyme position *vs* time plots (Figure 20 A). Kymographs (Figure 19 B) were generated using ImageJ (Schneider et al., 2012).

2.2.11.4. Single molecule DNA hydrolysis assay

The single-molecule DNA nicking and cleavage assay was carried out using magnetic tweezers as previously described (van Aelst et al., 2010; Ramanathan et al., 2009). Flow cells were incubated for 1 h with 50 µg/ml antidigoxigenin in PBS buffer (see 2.1.3.) followed by a 1 h incubation with 20 mg/ml BSA. After rinsing the flow cell with the PBS buffer, non-magnetic 3 µm polystyrene beads serving as reference (Huhle et al., 2015) were applied to the flow cell and incubated for 30 min to allow their binding to the surface. Unbound reference beads were washed away using PBS. The 7.4 kb DNA construct (Figure 8B) with biotinylated and digoxigenin-labelled termini was incubated with streptavidin-coated 1 µm magnetic beads (MyOne, Invitrogen) and injected into the flow cell. Excess of unbound DNA molecules was washed out with PBS after 10 min, and DNA molecules were stretched using a pair of magnets mounted on a motorized stage above the flow cell (see Kemmerich, Kasaciunaite, & Seidel, 2016 for details on the magnetic tweezers setup). The DNA length was inferred from the position of the magnetic bead above the flow cell surface. Bead positions were obtained using videomicroscopy (Huhle et al., 2015; Otto et al., 2010). The force acting on the DNA molecule was obtained by power-spectral density analysis of the magnetic bead fluctuations perpendicular to the force (Daldrop et al., 2015). Individual DNA molecules held at a tension of 2 pN were positively supercoiled by applying 25 turns of the magnets. 0.2-1 nM BcnI(N18C+C202S) in the Measurement buffer supplemented with 10 mM $Mg(OAc)_2$ was injected into the flow cell and the DNA length was monitored. DNA nicking by BcnI resulted in an increase in DNA length due to its torsional relaxation. Upon cleavage of the second strand the bead was released (Figure 24 A).

3. RESULTS AND DISCUSSION

3.1. The mechanism of double-stranded DNA cleavage by the monomeric restriction endonuclease BcnI

Orthodox restriction endonucleases (REases) are homodimers that bind palindromic 4-8 bp DNA sequences to form complexes in which the DNA and the protein share a dyad symmetry. Such an arrangement places the active site and sequence recognition elements from one subunit against the scissile phosphodiester bond and DNA bases in one half of the recognition site and the other subunit against the symmetry related half-site, thereby enabling concerted cleavage of phosphodiester bonds in both DNA strands (Kelly and Smith, 1970). In sharp contrast, Type II restriction endonuclease BcnI is a monomeric protein, which forms an asymmetric BcnI-DNA complex with the recognition sequence 5′-CCSGG-3′, making base-specific contacts with the entire target sequence and placing the sole catalytic center in the vicinity of DNA strand with the central C (5′-CCCGG-3′, C-strand), as observed in the co-crystal structure PDB ID 2ODI (Figure 15B) (Sokolowska et al., 2007), or to the strand with the central G (5′-CCGGG-3′, G-strand), as observed in the alternative structure (Figure 15C, PDB ID 3IMB).

Several possible mechanisms for cleavage of double-stranded DNA by the monomeric restriction endonucleases BcnI were proposed (Figure 9). Since the structures of DNA-bound BcnI are inconsistent with transient dimerisation of enzyme on the target sequence (Figure 9A, “dimerisation” mechanism; in such case two protein monomers would compete for interactions with the same bases and clash in various other places (Sokolowska et al., 2007a)), it was suggested that BcnI generates a double-strand break in two separate nicking reactions: after hydrolysis of the first DNA strand enzyme switches its orientation on the nicked

intermediate and then cleaves the second DNA strand (Figure 9B). Presumably, the two alternative BcnI-DNA structures mentioned above (Figure 15B,C) represent the two types of BcnI-DNA complexes that are formed during sequential cleavage of the DNA strands. In addition, several alternative reaction mechanisms, including recruitment of another monomer from the solution, which binds in the opposite orientation and displaces the originally bound monomer (Figure 9A, "recruitment" mechanism), or cleavage via a hairpin intermediate (Figure 9C), could not be ruled out (Sokolowska et al., 2007a). To distinguish these possibilities, we have performed detailed single-turnover and steady-state kinetics studies of BcnI reactions on double-stranded DNA.

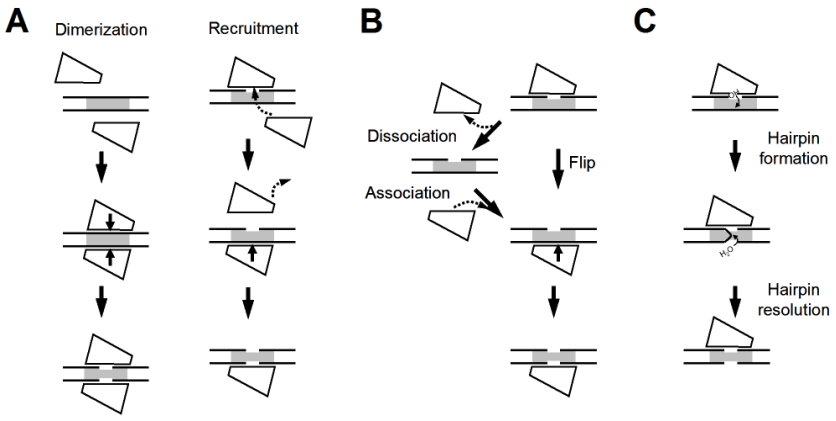

Figure 9. Possible mechanisms for cleavage of double-stranded DNA by monomeric restriction endonucleases specific for palindromic DNA sequences. Protein monomer is designated by a quadrangle shape, DNA is depicted as two parallel black lines, and the recognition site is represented by a grey rectangle. (A) The enzyme may either form a transient dimer, or recruit a second monomer from solution that displaces the first monomer and binds in the opposite orientation. (B) Sequential mechanism; after hydrolysis of the first DNA strand, the enzyme switches its orientation on DNA and then cleaves the second DNA strand. The switch may be achieved either by dissociation-reassociation of the enzyme with the target site, or by a flip in orientation without being physically separated from DNA. (C) Both strands are cleaved in the single active site via a hairpin intermediate.

3.1.1. Single-turnovers of BcnI on supercoiled DNA substrate

Characterization of double-stranded DNA cleavage by BcnI was performed on supercoiled phage phiX174 DNA that carries a single BcnI site 5′-CCSGG-3′. Incision of a single DNA strand converts the supercoiled substrate SC into the nicked open circular intermediate OC, and cleavage of the second DNA strand results in the final full length linear product FLL (Figure 10A); supercoiled, open circular and linear forms of the substrate can be separated and quantified using agarose gel electrophoresis (see 2.2.3). Single-turnover experiments, with the enzyme in molar excess of the substrate, can reveal directly the state of the enzyme-bound DNA throughout the course of the reaction. Single turnovers of BcnI were performed in two modes: the pre-mix mode, where the supercoiled substrate was preincubated with large excess of enzyme prior to initiation of the reaction with Mg^{2+} ions (diagram in Figure 10B), and post-mix mode, where the reaction is initiated by mixing enzyme and DNA in the presence of Mg^{2+} (diagram in Figure 10C). Pre-mix setup eliminates the stage of enzyme-DNA association (Figure 10B), allowing measurement of the actual DNA cleavage rates. Reaction profiles determined with 100 nM and 200 nM of BcnI in the pre-mix mode were undistinguishable (combined data provided in Figure 10B), suggesting that the observed reaction rates are not affected by enzyme-DNA association but instead reflect just the conversion of enzyme-bound substrate to product. BcnI rapidly converted supercoiled DNA into the nicked intermediate ($k_1 \approx 8.3\ s^{-1}$), but cleavage of the nicked DNA was much slower ($k_2 \approx 0.3\ s^{-1}$) (Figure 10B).

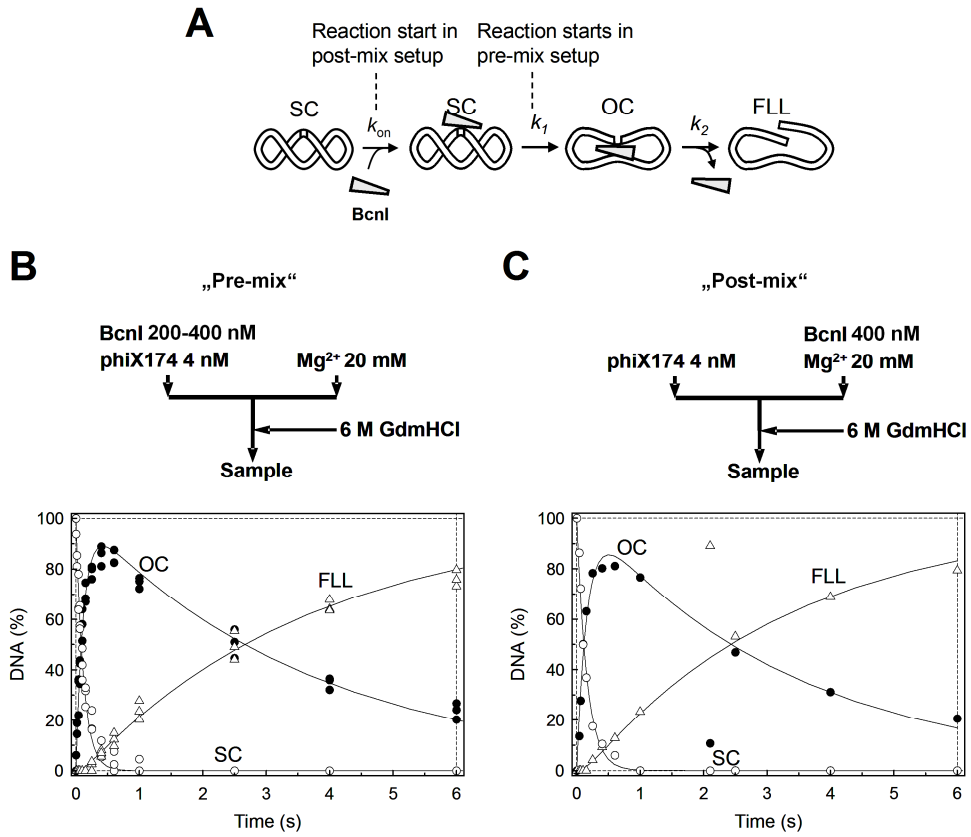

Figure 10. Single turnovers of BcnI on supercoiled phiX174 DNA. (A) Proposed mechanism for cleavage of double-stranded DNA. Upon binding to the supercoiled substrate SC (association rate constant k_{on}), the enzyme nicks the first DNA strand (rate constants k_1) converting the substrate into the nicked intermediate OC. To complete the reaction, BcnI must switch its orientation on the recognition sequence and cleave the remaining DNA strand generating the final product (FLL). All reaction steps that lead to cleavage of the second DNA strand are described by the rate constant k_2. In the pre-mix reaction, the enzyme and DNA are pre-equilibrated in the Reaction buffer (see 2.1.3.) devoid of the cofactor Mg^{2+}; in this case cleavage of the first DNA strand starts immediately upon addition of Mg^{2+} ions. In the post-mix setup, the reaction is initiated by mixing enzyme and DNA, therefore DNA cleavage must be preceded by the enzyme binding step. (B-C) BcnI cleavage of supercoiled phiX174 DNA in the pre-mix and the post-mix reactions, respectively. The flow diagrams schematically depict the two types of experiments performed in a quench-flow device (see 2.2.6.2. for details).The amounts of three DNA forms are shown: intact supercoiled substrate SC (unfilled circles), nicked intermediate OC (filled circles), and the linear product FLL (unfilled up-triangles). Solid lines are the fit of the scheme in panel A to experimental data, assuming that the enzyme binding steps do not contribute to the observed DNA cleavage. The fitting procedure gave k_1=8.3±0.2 s^{-1} and k_2=0.27±0.01 s^{-1} for the pre-mix reaction (panel B) and k_1=6.2±0.2 s^{-1} and k_2=0.30±0.01 s^{-1} for the post-mix reaction (panel C).

Post-mix reactions also resulted in immediate formation of DNA hydrolysis products (Figure 10C). Moreover, the determined rates for cleavage of individual DNA strands were close to the values from the pre-mix experiments (Figure 10B-C). Similar DNA cleavage rates observed from pre-mix and post-mix reactions imply that at the BcnI concentration examined here (200 nM), the bimolecular step of enzyme binding to its recognition site in the phiX174 substrate (k_{on}×[BcnI], Figure 10A) is faster than the subsequent DNA nicking (k_1≈6 s^{-1}). This establishes a lower limit of 3×10^7 $M^{-1}s^{-1}$ (6 s^{-1}/2×10^{-7} M) for the BcnI-DNA association rate constant k_{on}: constants of $\leq3\times10^7$ $M^{-1}s^{-1}$ would lead to the association process limiting the subsequent rate of DNA cleavage.

High yield of nicked DNA (up to 90%), and the ratio of the rate constants k_1/k_2 (>20), observed in the single turnovers of BcnI (Figure 10B-C) also indicate that BcnI reactions on the first and on the second DNA strands are not equivalent. This is in agreement with the reaction mechanism that requires the enzyme to switch the orientation prior to cleavage of the second DNA strand (sequential mechanism in Figure 9B); alternatively, the second strand may be cleaved via a different catalytic mechanism than the first strand (reaction via hairpin intermediate, Figure 9C). Unfortunately, the hairpin intermediate, had it been formed during the reaction, would have remained undetected in the supercoiled DNA cleavage experiments, as its electrophoretic mobility would coincide with the final linear DNA. However, no hairpin intermediate was detected in the kinetic experiments performed on radiolabelled DNA duplexes, suggesting that the reaction involving hairpin DNA is an unlikely possibility. Experiments on oligonucleotides also indicated that during the first reaction step BcnI predominantly nicks the G strand (the strand with the central G, 5′-CCGGG-3′), though a significant amount (up to 25%) of the intermediate with the nicked C strand (the strand with the central C, 5′-CCCGG-3′) was also detected.

3.1.2. Single turnover reactions on preassembled nicked substrates.

As pointed out above, BcnI cleaves the first DNA strand more than 20-fold faster than the second strand (Figure 10B-C). Non-equivalent reactions on two strands are in agreement with the proposed BcnI reaction mechanism (Figure 9A): the enzyme can hydrolyse the first DNA strand immediately upon formation of the enzyme-DNA complex, but hydrolysis of the second DNA strand must be preceded by the switch in enzyme orientation. If the switch is slower than DNA hydrolysis, it may limit the rate of the second DNA strand cleavage. Alternatively, BcnI may have intrinsically lower catalytic activity against the intact DNA strand in the nicked intermediate. To distinguish these possibilities, we performed single-turnover experiments on the pre-nicked DNA substrates.

The pre-nicked substrates 30 bp G-nick and 30 bp C-nick were assembled from three DNA strands (see 2.3 and Table 2). Pre-mix experiments on the 30 bp G-nick and 30 bp C-nick oligonucleotides performed at different enzyme concentrations (200 nM and 400 nM) were undistinguishable (combined data sets are provided in Figure 11), suggesting that enzyme binding steps are fast and do not contribute to the observed rate of DNA cleavage. Fitting single exponentials to the experimental results (see 2.7.2) gave the rate constant *k(C)* for cleavage of the C strand in the G-nick DNA and the constant *k(G)* for cleavage of the G strand in C-nick DNA. BcnI hydrolyses the pre-formed nicked substrates much faster, than the nicked reaction intermediate formed *in situ* during cleavage of the supercoiled phiX174 DNA (compare $k(C) \approx k(G) \approx 8.5\ s^{-1}$, Figure 11A-B, and $k_2 \approx 0.3\ s^{-1}$, Figure 10B-C). This confirms that slow cleavage of the nicked intermediate observed in BcnI reactions on an intact substrate is not caused by the intrinsically low catalytic activity of BcnI on nicked DNA, but instead must be due to the slow switch in

enzyme orientation on DNA that brings the catalytic center to the second DNA strand (Figure 9B).

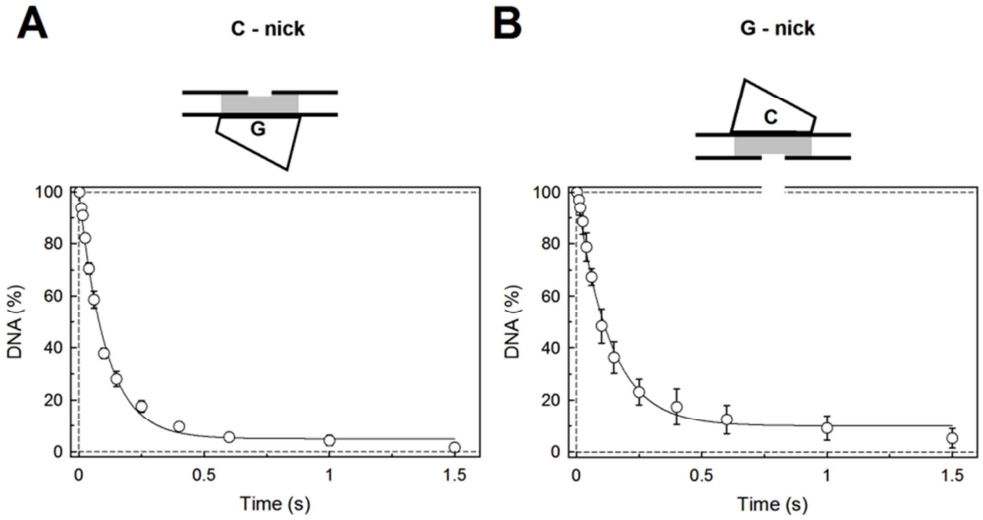

Figure 11. Single turnovers of BcnI on preassembled nicked substrates. BcnI complexes formed with nicked substrate are depicted in both panels. Reactions were performed in the pre-mix setup: the enzyme and DNA are pre-equilibrated in the Reaction buffer (see 2.1.3.) devoid of the cofactor Mg^{2+}; in this case reaction starts immediately upon addition of Mg^{2+} ions. Solid lines are the fit of a single exponential to experimental data. The fitting procedure gave $k(G)$=7.6±0.3 s^{-1} for the reaction with the C-nick substrate (panel A) and $k(C)$=9.3±0.3 s^{-1} for the reaction with the G-nick substrate (panel B).

3.1.3. Steady-state BcnI reactions on supercoiled DNA substrate

Unlike the single-turnover reactions, steady-state experiments reveal the rate of the complete turnover of the enzyme, including DNA binding, cleavage and product dissociation. Reaction products that accumulate in the steady-state reactions are released by the enzyme. Thus, analysis of their composition may reveal the number of phosphodiester bonds cleaved by BcnI during a single binding event. Dissociation of enzyme into bulk solution after cleavage of the first DNA strand ("dissociation" mechanism in Figure 9B) would result in high yield (up to 50% of total DNA) of nicked intermediate; formation of the final reaction

product with a double-strand break would suggest that enzyme cleaves both DNA strands during a single binding event ("flip" model in Figure 9B).

BcnI steady-state reactions were performed with large excess of DNA (1-2 nM phiX174) over the enzyme (0.1 nM) (Figure 12). The reaction rate was independent of substrate concentration, indicating that K_M was significantly lower than 1 nM, the lowest substrate concentration in our experiments. The determined initial reaction rates v_0 therefore are equal to v_{MAX} and the ratio v_{MAX}/[BcnI]≈0.05 s^{-1} corresponds to k_{cat}. Surprisingly, the major reaction product is full length linear DNA with a double-strand break; the nicked intermediate comprises only ≈ 10% of total DNA (or ≈ 25% of all products, Figure 12). This argues against cleavage of double-stranded DNA via transient dimerisation (Figure 9A), as dimerisation is unlikely under [BcnI] << [DNA] reaction conditions, and rules out obligatory dissociation of BcnI from DNA after hydrolysis of the first DNA strand (Figure 9B, though dissociation mechanism may account for ~25% of nicked products). Efficient formation of the final reaction product, on the other hand, is consistent with the switch in BcnI orientation that occurs without physical separation of enzyme from the DNA (the "flip" mechanism in Figure 9B).

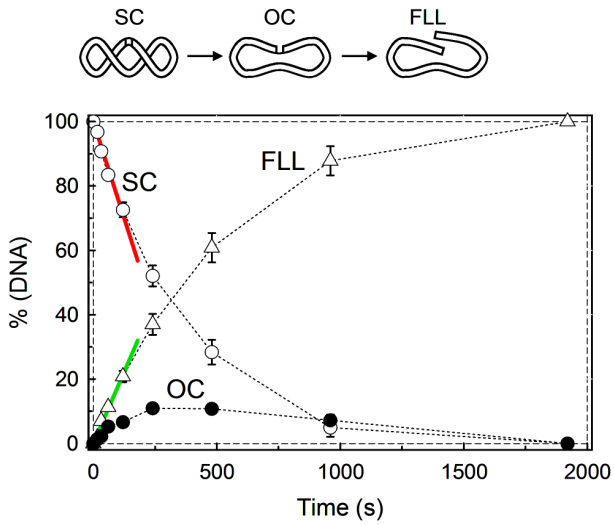

Figure 12. Steady-state reactions of BcnI on the supercoiled phiX174 DNA. The scheme above the graph illustrates the various DNA forms that can exist during BcnI reactions on supercoiled phage phiX174 DNA. The steady-state reaction contained 2 nM DNA and 0.1 nM BcnI. The continuous red line is the linear fit to SC DNA cleavage data. The determined initial reaction rate is 0.0048±0.0003 nM/s and the kcat equals 0.048±0.003 s^{-1}. The continuous green line is the linear fit to the FLL product formation data. The determined initial FLL formation rate equals 0.0036±0.0015 nM/s. Thus, BcnI converts ~75% (the ratio 0.0036/0.0048) of the initial substrate SC into the final reaction product FLL during a single binding event.

However, the underlying mechanism for this "flip" remains elusive. To cleave the second strand by the same active site, BcnI must rotate by 180° around the axis perpendicular to the DNA; as BcnI forms a clamp around the cognate duplex (Sokolowska et al., 2007a), such rotation would result in steric clashes between DNA and the protein. To evade the clashes, the protein clamp could be straightened out after cleavage of the first strand via hinge motion of BcnI subdomains (Sokolowska et al., 2007a), enabling the rotation without physical separation from the DNA. But what would be the driving force for such rotation and the attachment point of BcnI to DNA?

3.1.4. Experiments with DNA and protein trap

To directly probe the mechanism of the presumed switch in BcnI orientation occurring after cleavage of the first DNA strand, we performed single turnover experiments with DNA and protein trap (Figure 13). In the DNA-trap setup, BcnI and phiX174 plasmid DNA were preincubated as in the pre-mix reactions (Figure 10A.), but DNA cleavage was initiated by simultaneous addition of Mg^{2+} and large excess of cognate duplex DNA (final composition was 2 nM phiX174, 200 nM enzyme and 2000 nM oligoduplex TRAP, see Table 2). Any enzyme not bound to the substrate DNA at the initial reaction moment, or enzyme that dissociates from the substrate during the reaction, should be trapped on the unlabelled oligonucleotide duplex. Thus, if the switch in enzyme orientation requires dissociation of BcnI into bulk solution, cleavage of the second DNA strand should be inhibited by the trap DNA. Control reaction, iniciated by mixing BcnI and phiX174 + TRAP oligoduolex solutions, revealed significantly slower hydrolysis of phiX174 and proved trap effectiveness (Sasnauskas et al., 2011). However, the BcnI reaction is resistant to challenge with excess trap oligoduplex (Figure 13A). Like in the ordinary pre-mix experiment (Figure 10A), supercoiled phiX174 is first converted into the open-circular intermediate and then into the final product with a double-strand break. The rate constants for cleavage of the first and the second DNA strands in the pre-mix and DNA-trap experiments are also similar (Figure 10A and Figure 13A).

Taken together, DNA-trap reactions provide direct evidence that BcnI is able to cleave both DNA strands without dissociation into bulk solution. This complements the steady-state phiX174 cleavage experiments described above (see 3.2.3). Moreover, complete cleavage of phiX174 supercoiled DNA in DNA-trap setup (Figure 13A) confirms that all DNA was bound by the enzyme during the

preincubation and the rate for BcnI-DNA dissociation is much slower than the rate for the first DNA strand hydrolysis.

In the protein-trap experiment (Figure 13B), the phiX174 with pre-bound BcnI DNA was mixed with Mg^{2+} ions and a large excess of a binding proficient, but catalytically inactive BcnI mutant D55A (final composition: 2 nM phiX174 DNA, 200 nM enzyme, 8 μM D55A mutant). Since a control DNA cleavage experiment performed with a mixture of D55A and wt BcnI revealed that the mutant inhibits DNA cleavage by the wt enzyme (presumably via competition for the recognition sites), any DNA substrate (either intact plasmid or nicked intermediate) liberated from the wt enzyme during the reaction should be trapped by the D55A mutant (Sasnauskas et al., 2011). Indeed, in the protein-trap experiment, BcnI rapidly converts the majority of intact DNA into the nicked intermediate OC, but contrary to the DNA-trap experiment, the reaction nearly stops after the first nicking event, as the nicked intermediate remains uncleaved (Figure 13B). This points to dissociation of the enzyme from the target sequence after nicking of the first DNA strand. Liberation of the recognition site after cleavage of the first DNA strand is also inconsistent with the reaction involving a hairpin intermediate (Figure 9C).

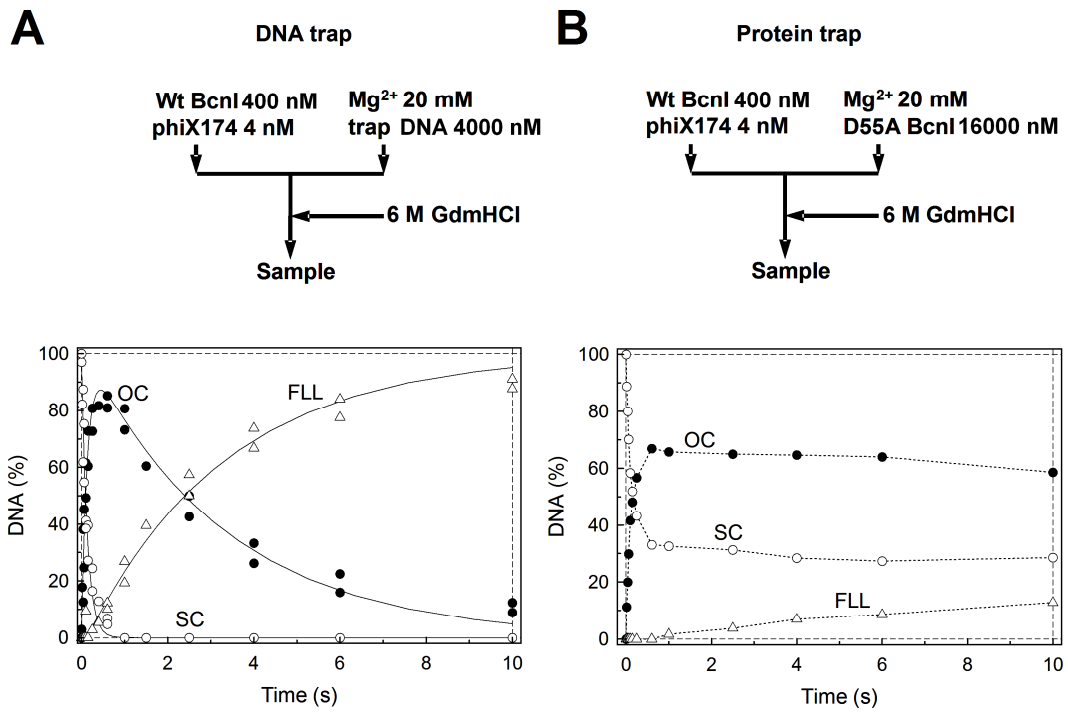

Figure 13. Trap experiments. In both panels, amounts of three phiX174 DNA forms are shown: supercoiled substrate (SC, unfilled circles), open-circular reaction intermediate (OC, filled circles) and linear product (FLL, unfilled triangles). (A) Pre-mix experiment with trap DNA. The flow diagram schematically depicts the experiment performed in a quench-flow device. A sample of enzyme preincubated with phiX174 DNA was mixed with magnesium acetate and excess of unlabelled TRAP oligoduplex (Table 2). Oligoduplex DNA has no effect on the formation and cleavage of the nicked intermediate, indicating that rearrangement of BcnI on the OC DNA, required for cleavage of the second DNA strand, does not involve dissociation of the enzyme into bulk solution. The fitting procedure gave k_1=7.5±0.3 s^{-1}, k_2=0.31±0.01 s^{-1}. (B) Post-mix experiment with trap protein. A sample of enzyme preincubated with phiX174 DNA was mixed with magnesium acetate and excess of inactive BcnI mutant D55A. The mutant protein significantly inhibits cleavage of the open circular intermediate, indicating that during the rearrangement on the nicked DNA, BcnI exposes the recognition sequence, enabling binding of the inactive mutant.

How can we reconcile the apparent dissociation of BcnI from the nicked intermediate in the protein-trap experiment (Figure 13B) with cleavage of both DNA strands during a single binding event inferred from DNA-trap and steady-state reactions (Figure 12 and Figure 13A)? We propose that after cleavage of the first DNA strand BcnI dissociates from the nicked target site, but does not diffuse

into bulk solution; instead, it reassociates with a random site on the same DNA molecule. This situation may arise because a protein at a particular position in an aqueous solution will, as a result of Brownian motion, tumble relatively rapidly around that position but only rarely escape to a new position (Gowers et al., 2005; Halford, 2004). Multiple rounds of dissociation-reassociation to the same DNA molecule (known as 'hopping' (see 1.3.3.)), interspaced with stages of thermal motion along the DNA axis (known as 'sliding' (see 1.3.3.)), may allow the same BcnI molecule to locate, bind and cleave the opposite strand of the recognition site. This would account for cleavage of both DNA strands during a single binding event observed in steady-state (Figure 12) and DNA-trap (Figure 13 A) experiments. On the other hand, during the diffusional walk on the nicked intermediate, the enzyme transiently unshields its target sequence. In the protein trap setup, this permits binding of the inactive mutant to the nicked BcnI site, thereby inhibiting its further cleavage (Figure 13 B).

The above model can also account for the incomplete cleavage of the substrate in the protein-trap experiment *versus* complete cleavage in the DNA-trap experiment (Figure 13 A-B). Complete cleavage of all substrate in the DNA-trap setup indicates that all DNA is bound by the enzyme at the moment of reaction start; however, this may be an equilibrium mixture of specific BcnI-DNA complexes and DNA molecules with nonspecifically bound BcnI. Upon initiation of the DNA-trap reaction, the nonspecifically bound enzyme may rapidly locate and cleave the target site, as excess of oligoduplex DNA, introduced into the reaction together with Mg^{2+}, does not interfere with sliding and hopping of BcnI on the substrate. In the protein-trap setup, the inactive mutant, present at a very high concentration, may locate the unoccupied BcnI sites before the Wt enzyme, and in that way inhibit their cleavage (the slowly cleaved fraction corresponds to ~20% of phiX174, Figure 13 B).

3.1.5. The overall reaction mechanism of BcnI

The biochemical studies of BcnI presented above are summarized in Figure 14. The BcnI reaction can be divided into five steps: (i) association of BcnI with the DNA substrate; (ii) cleavage of the first DNA strand; (iii) the switch in BcnI orientation on the DNA; (iv) cleavage of the second DNA strand; and (v) product release.

Almost identical DNA cleavage rates observed from reactions initiated by adding Mg^{2+} to the preincubated enzyme and DNA (pre-mix setup) or by adding enzyme to DNA (post-mix setup) (Figure 18B-C) established a lower limit of 3×10^{7} $M^{-1}s^{-1}$ for the BcnI association rate constant k_{on} (see 3.1.1); this value is close to the diffusion-limited rate of 1×10^{8} $M^{-1}s^{-1}$ (Halford and Marko, 2004) and to the enzyme-DNA association rates determined for other restriction enzymes (Laurens et al., 2009; Zaremba et al., 2010). Upon association with DNA, BcnI cleaves double-stranded DNA in two separate and non-equivalent reactions: intact DNA is rapidly converted into the nicked intermediates *via* cleavage of the first strand (rate constants k_1 is close to 8 s^{-1}), but cleavage of the second DNA strand occurs at a much lower rate (rate constant k_2 is less than 0.3 s^{-1}, Figure 10). Surprisingly, the cleavage rate of the intact strand in the pre-nicked substrates is much higher (rate constants *k(C)* and *k(G)* are close to 8.5 s^{-1}, Figure 11). Thus, hydrolysis rate of the nicked intermediate formed *in situ* ($k_2\approx0.3$ s^{-1}) must be limited by the slow switch in BcnI orientation on DNA. We propose that the switch in enzyme orientation involves a diffusional walk (or facilitated diffusion) of BcnI on the nicked intermediate, involving sliding and hopping (see 3.1.4 and 3.1.5). Studies of other restriction endonucleases demonstrated that sliding and hopping on DNA may facilitate target site location among excess of nonspecific DNA sequences (Bellamy et al., 2005; Gowers and Halford, 2003; Stanford, 2000). BcnI utilizes facilitated diffusion in an unusual way: sliding/hopping is not

only the tool for target site location, but also the integral part of the BcnI reaction on the double-stranded DNA. Efficient use of facilitated diffusion allows BcnI to locate, bind and cleave the same target sequence twice during a single binding event (only 10-25% of DNA is released by BcnI after nicking of a single DNA strand, Figure 12). Therefore, the final reaction product released by monomeric BcnI – DNA with a double-strand break – is the same as the product of the orthodox homodimeric enzymes.

The reaction cycle of many restriction endonucleases is limited by product release (Sapranauskas et al., 2000; Sasnauskas et al., 1999; Wright et al., 1999). This may also be the case for BcnI: the turnover number k_{cat} for cleavage of phiX174 DNA (k_{cat}≈0.05 s^{-1}, Figure 13) is significantly lower than the slowest step observed in the single-turnover experiments, i.e. cleavage of the second DNA strand (k_2≈0.3 s^{-1}, Figure 10 B-C), indicating that the rate-limiting step of BcnI is product release occurring after complete cleavage of the DNA substrate (rate constant k_{dis}, Figure 14).

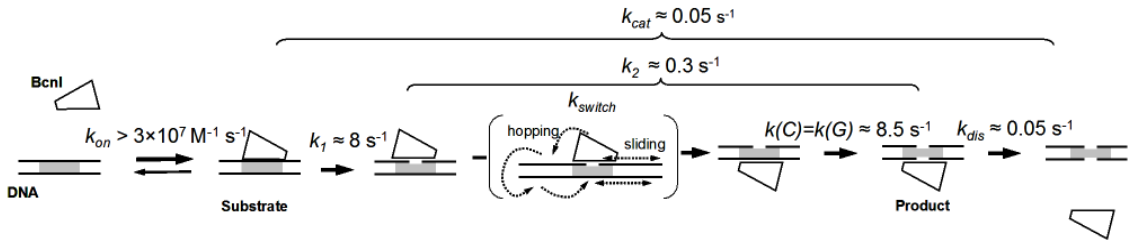

Figure 14. Mechanism of double-stranded DNA cleavage by BcnI. BcnI rapidly associates with substrate DNA (rate constant k_{on}); ensuing hydrolysis of the first DNA strand (rate constant k_1) converts the substrate into the nicked intermediate. The second strand is cleaved at a much lower rate (rate constants k_2). The latter process consists of two phases: (i) relatively slow switch of BcnI on DNA (rate constant k_{switch}) involving dissociation of BcnI and diffusional search for the opposite DNA strand; and (ii) rapid hydrolysis reaction (*k(C)* or *k(G)*). The reaction cycle is completed by the product release (rate constant k_{dis}) that limits the turnover rate of BcnI k_{cat}. Possible dissociation of BcnI into bulk solution after cleavage of the first DNA strand (may correspond to ~1/4 of all BcnI reactions on the phiX174 DNA) is not shown.

3.2. BcnI single molecule experiments

Kinetic studies in bulk solution indicated that the BcnI reaction consists of target site localisation, cleavage of the first strand, a switch in enzyme orientation via sliding and hopping, and cleavage of the second DNA strand. However, some stages of this reaction mechanism, e.g. the interaction dynamics of BcnI with cognate and non-cognate DNA remained uncharacterized, while others, e.g. the sliding and hopping of the enzyme on the DNA, remained hypothetic. To address these questions, we have characterised the conformational states of BcnI, the dynamics of specific and non-specific BcnI-DNA interactions, and facilitated diffusion of BcnI on the DNA using various single molecule techniques.

3.2.1. Comparison of apo-BcnI structure with BcnI-DNA complex structure

Several crystallographic structures are available for BcnI, including apo-BcnI (PDB ID 2ODH) and BcnI in complexes with cognate DNA, with BcnI active sites in the proximity of either ‘C’ strand (5′-CCSGG-3′, PDB ID 2ODI) of the ‘G’ strand (5′-CCGGG-3′, PDB ID 3IMB) (Sokolowska et al., 2007). Structural data also indicates that formation of the specific enzyme-DNA complex is accompanied by the transition of BcnI from the more open conformation (PDB ID 2ODH) to a more closed conformation (PDB IDs 2ODI, 3IMB). Upon formation of the ‘closed’ structure the DNA recognition and catalysis subdomains move closer to each other and lock DNA in the binding cleft (Figure 15).

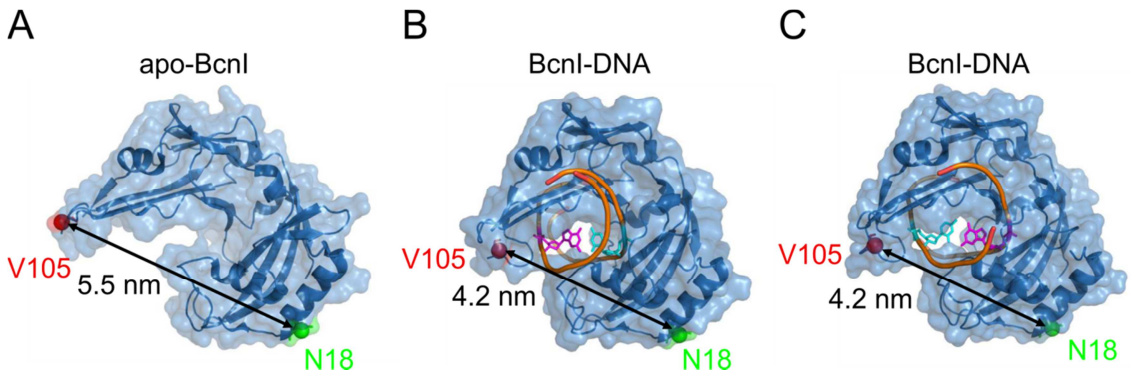

Figure 15. BcnI structures in the absence and in the presence of DNA. Structures of apo-BcnI (PDB ID 2ODH) (panel A) and two alternative BcnI-DNA complexes with the catalytic center in the proximity of either the 'C' strand (PDB ID: 2ODI) or the 'G' strand (PDB ID: 3IMB) (panels B and C, respectively). The green and red spheres indicate the Cβ atoms of N18 and V105 residues used for fluorescent labelling. The transition of BcnI from the apo- ('open') to the DNA-bound ('closed') conformation reduces the distance between the Cβ atoms from 5.5 to 4.2 nm, causing an increase in FRET efficiency. The central G and C nucleotides of the BcnI target site are depicted in magenta and cyan respectively.

3.2.2. Selection of labelling positions

To investigate the conformational states of individual BcnI molecules in solution, we have designed single molecule FRET experiments with BcnI variants carrying a pair of fluorescent labels (Alexa488 and Alexa546), one label on the recognition and one on the catalytic subdomains. Positions for both labels were selected such that the distance between the Cβ atoms of the corresponding residues (N18 and V105) is close to the theoretical R_0 value for the Alexa488-Alexa546 dye pair (6.4 nm), and the distance change upon the transition from the apo- ('open', PDB ID 2ODH) to the DNA-bound ('closed', PDB ID 2ODI), (Figure 15A-B) form results in a significant change in FRET efficiency (Table 3).

Table 3. The optimal positions for double-labelling of BcnI[1].

BcnI conformation	O	C	O	C	O	C
BcnI residue	**E104**		**V105**		**K209**	
I3	5.77	4.80	5.73	4.81	4.99	4.33
E15	5.35	4.44	5.44	4.16	4.87	4.33
N18	5.36	4.41	**5.51**	**4.20**	5.02	4.44
K19	4.91	3.93	5.05	3.72	4.53	3.93

To verify BcnI binding orientation on DNA, we have designed single molecule FRET experiments with fluorescently labelled protein and DNA. The position for DNA labelling was selected 14 bp upstream of the recognition site on either the 'C' strand (Alexa546-C-DNA, Table 2) or the 'G' strand (Alexa546-G-DNA, see Table 2). The dye positions on BcnI (N18, V105 and K209) were selected such that the flip in protein binding orientation from 'C' to 'G' strand would significantly change the distance between the C5 atom of the modified DNA pyrimidine base and the Cβ atom of the selected protein residue (Table 4). The modeling was based on the BcnI-DNA structures 2ODI and 3IMB (Figure 15).

[1] Residues from the DNA binding domain are listed in the top row (green), residues from the catalytic domain are listed in the first column (orange). The distances (in nm) between the Cβ atoms of the corresponding protein residues are measured for the 'open' ('O'), and the 'closed' ('C') BcnI conformations. The measurements are based on the X-ray structures of apo- and DNA-bound BcnI (PDB IDs 2ODI and 2ODH, respectively) using theoretical Alexa488-Alexa546 Förster (RO) radius of 6.4 nm. The positions that lead to the largest (>1 nm) change in the measured distance upon the 'open' /'closed' transition are shaded green, positions that lead to a 0.9-1.0 nm change are shaded yellow, the other position are not shaded.

Table 4. The optimal positions for DNA labelling[2].

Position	ΔE(N18)	ΔE(V105)	ΔE(K209)	ΔE(N18)	ΔE(V105)	ΔE(K209)
	'C'-strand label			**'G'**-strand label		
-10	0.21	0.02	0.22	0.25	0.06	0.25
-11	0.28	0.06	0.30	0.31	0.12	0.34
-12	0.33	0.11	0.37	0.37	0.17	0.42
-13	0.35	0.12	0.42	0.40	0.20	0.48
-14	**0.34**	**0.11**	**0.43**	**0.39**	**0.20**	**0.51**
-15	0.30	0.07	0.40	0.36	0.16	0.50
-16	0.24	0.03	0.35	0.29	0.12	0.47

The corresponding BcnI mutants carrying a single cysteine residue at the desired position, and the theoretical E_{FRET} values calculated for both protein orientations are listed in Figure 22.

3.2.3. Construction of BcnI cysteine mutants

To enable site-specific labelling of BcnI with maleimide derivatives of fluorescent dyes, it is necessary to avoid unspecific labelling of native cysteines. The sole native cysteine (C202) present in wt BcnI was replaced with either an alanine (this mutation completely removes the sulfhydryl moiety) or a serine (the sulfhydryl moiety is replaced by a hydroxyl). The mutant proteins BcnI(C202A)

[2] Optimal Alexa546 label positions on DNA for DNA – BcnI FRET experiments were defined measuring distances between Cβ atoms of BcnI selected residues (N18, V105, K209) and C5-methyl carbon atom on T nucleotide on the 'C' (DNA strand with 5′-CCCGG-3′ sequence of BcnI target site) or 'G' (DNA strand with 5′-CCGGG-3′ sequence of BcnI target site) DNA strands. Measurements were performed on BcnI – DNA models made from structures where the catalytic center of BcnI contacts the scissile phosphodiester bond either in the 'C' (PDB ID: 2ODI) or 'G' (PDB ID: 2ODI) strands with prolonged DNA in the complex. FRET efficiency differences (ΔE_{FRET}) were calculated from distances measured between BcnI bound to DNA in 'C' and DNA nucleotide on the certain DNA strand upstream to the BcnI specific site and BcnI bound to DNA in 'G' orientation and the same nucleotide (Theoretical Alexa488-Alexa546 Forster radius (R_O) 6.4 nm). DNA position -14 with largest ΔE_{FRET} values for most measurements were selected (coloured in green).

and BcnI(C202S) were expressed (see 2.2.2.2.), purified (see 2.2.2.3) and their biochemical properties were tested. Compared to wt BcnI, both BcnI mutant proteins exhibited almost equal affinity (see 2.2.5.) to specific DNA (Figure 16A, Table 5). Steady-state kinetic experiments on the 1-site circular double-stranded DNA substrate φX174 (see 2.2.6.1.) revealed that both BcnI(C202A) and BcnI(C202S) cleave substrate with comparable rates to wt BcnI (Figure 16B, Table 5), but BcnI(C202A) releases more nicked DNA intermediate (OC) (approx.. 20 %) during the reaction course, which is not characteristic to wt BcnI. Therefore the BcnI(C202S) mutant was chosen for the introduction of cysteine residues at the selected positions.

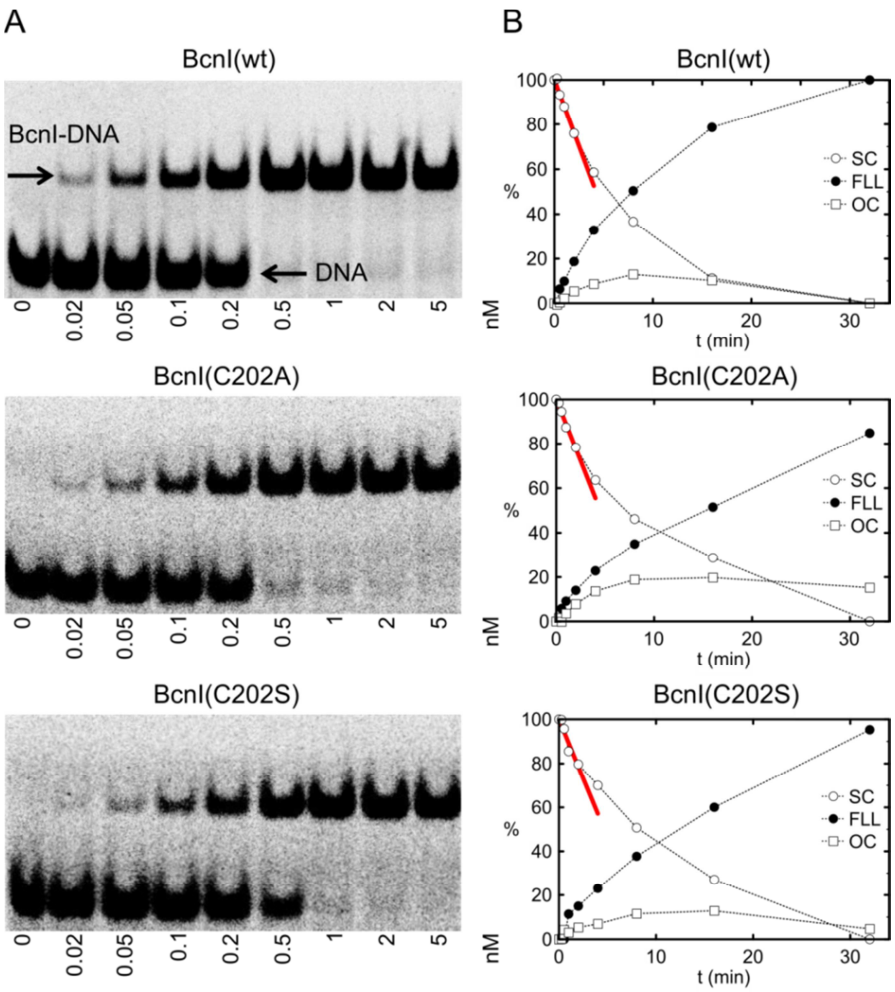

Figure 16. Comparison of biochemical properties of BcnI(wt), BcnI(C202A) and BcnI(C202S). (A) DNA binding experiments with BcnI(wt), BcnI(C202A) and BcnI(C202S). DNA binding experiments (see 2.2.6.) were performed with various BcnI concentrations (0.02-5 nM, marked under lines of the EMSA gels (2.2.1.3.)), 0.1 nM ^{33}P-labelled specific oligoduplex (see Table 2) and 10 mM Ca-acetate. Determined K_D values are provided in Table 5. (B) Activity of wt BcnI and mutants. Steady-state reactions were performed with 0.1 nM BcnI and 2 nM φX174, reactions were started with 10 mM Mg-acetate (see 2.2.6.1.). SC – supercoiled DNA (white circles), FLL – full-length linear DNA (black circles). Reaction rates are provided in Table 5.

Selected residues (N18, V105 and K209) were replaced by cysteines by site-directed mutagenesis (see 2.2.2.1). The resultant BcnI(N18+C202S), BcnI(V105C+C202S), BcnI(C202S+K209C) and BcnI(N18+V105C+C202S) mutants were expressed (see 2.2.2.2) and purified (see 2.2.2.3). Steady-state

kinetic experiments on φX174 (see 2.2.6.1.) revealed that mutants retained 52-74 % activity comparing to wt BcnI (Table 5); moreover, the mutations have little effect on the binding affinity (Table 5).

Table 5. Binding affinity to specific DNA and catalytic activity of BcnI mutants and BcnI-dye conjugates.

BcnI conjugate	k_D(nM)±*St. error*	k_{cat}(s^{-1})±*St. error*	k_{cat}, s^{-1} (BcnI protein)/ k_{cat}, s^{-1} (BcnI (wt)), %
BcnI(wt)	0.21±0.050	0.042±0.0017	100
BcnI(C202A)	0.2±0.038	0.037±0.0015	88
BcnI(C202S)	0.29±0.045	0.036±0.0035	86
BcnI(N18C+C202S)	0.29±0.065	0.022±0.0015	52
BcnI(N18C+C202S)-Alexa488	0.18±0.037	0.013±0.0012	31
BcnI(V105C+C202S)	0.15±0.041	0.026±0.0032	62
BcnI(V105C+C202S)-Alexa488	0.16±0.037	0.026±0.0013	62
BcnI(V105C+C202S)-Biotin	-	0.02±0.0015	48
BcnI(C202S+K209C)	0.18±0.049	0.029±0.0024	69
BcnI(C202S+K209C)-Alexa488	0.44±0.080	0.017±0.0011	40
BcnI(N18C+V105C+C202S)	0.3±0.094	0.031±0.0026	74
BcnI(N18C+V105C+C202S)-Alexa488-Alexa546	-	0.015±0.0012	36

3.2.4. Labelling of BcnI Cys mutants

BcnI single cysteine mutants were labelled using 10- to 20-fold molar excess of fluorescent dye and purified from the unreacted dye using a Heparin column (see 2.2.3.1.). BcnI double cysteine mutant at first was labelled with an equimolar amount of the donor fluorophore. Unlabelled, single-labelled and double-labelled BcnI variants were separated on a MonoS column by applying a linear NaCl gradient, and then the single-labelled protein was labelled with 10- to 20-fold excess of an acceptor fluorophore and purified using a Heparin column (see 2.2.3.2.). The purity of all conjugates was confirmed by analysis of SDS-PAGE gel (see 2.2.1.1.). The detected positions of fluorescent dyes colocolized with protein positions in the gel and no free dye was observed (Figure 17).

Labelling efficiencies were calculated from absorption measurements according to equations (30)-(34) (see 2.2.3.3., Table 6).

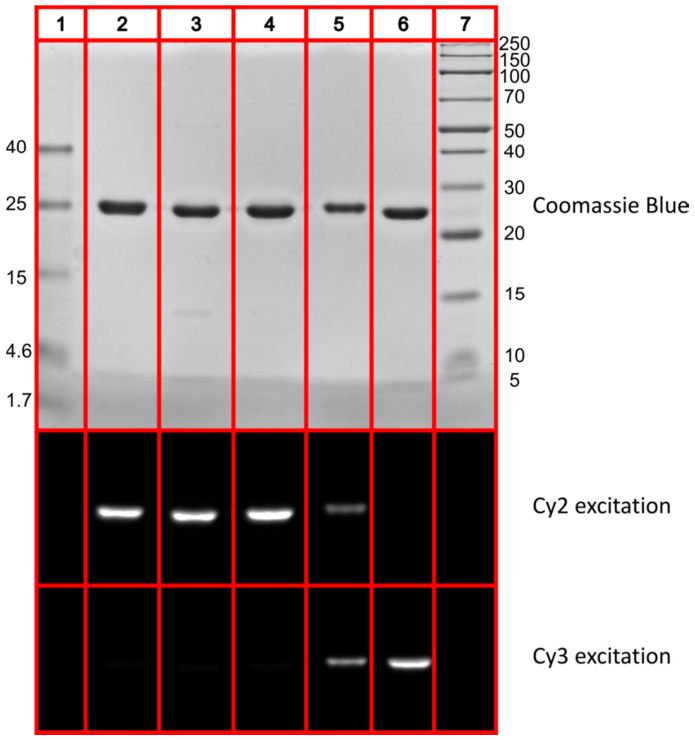

Figure 17. BcnI labelling. Fluorescently labelled BcnI variants were run on an SDS-PAGE gel (see 2.2.1.1.), scanned on a Fuji FLA-5100 fluorescence scanner using laser wavelengths for Cy2 and Cy3 detection, and then stained with Coomassie Blue. Fluorescence images (Cy2 and Cy3 excitation) revealed that protein is labelled with specific dyes and no free dyes are present. Stained page gel revealed that BcnI labelled proteins are not contaminated with other proteins. 1. Spectra Multicolor Low Range Protein Ladder(26628), 2. BcnI(N18C+C202S)-Alexa488, 3. BcnI(C202S+K209C)-Alexa488, 4. BcnI(V105C+C202S)-Alexa488, 5. BcnI(N18C+V105C+C202S)-Alexa488-Alexa546, 6. BcnI(N18C+C202S)-Cy3, 7. Page Ruler TM Broad Range (26630). 2 μg of each single-labelled and 1 μg of double-labelled BcnI protein were loaded on the gel.

3.2.5. Förster radius determination

Experimental Förster radius for a pair of fluorescent dyes differs from the theoretical value due to the fact that fluorophore attachment to the protein and its interactions with buffer solution components may change the radiative and non-radiative decay constants rates of an excited fluorophore (see 1.1.2., eq. (5)). To

calculate the experimental Förster radius, we have determined the experimental quantum yield (Φ) (see 2.2.8.1., Table 6) and the spectral overlap integral J (see 2.2.8.2.). The experimental Förster radii calculated for different experimental conditions (Table 6) allowed us to determine the theoretical E_{FRET} values from the available structures of BcnI and BcnI-DNA complexes (see 3.2.6., 3.2.8.1.).

Table 6. Labelling efficiencies, quantum yields (Φ), Förster radii (R_0) and anisotropies of fluorescently labelled BcnI proteins.

BcnI conjugate	Labelling efficiency	Conditions	Φ	R_0, nm	Anisotropy
BcnI(N18C+C202S)-Alexa488	75.9% (Alexa488)	-	0.77	6.0	0.134
		+10mM $Ca(OAc)_2$	0.75	5.98	0.135
		+10mM $Ca(OAc)_2$ + 1μM SP DNA	0.79	6.04	0.112
BcnI(V105C+C202S)-Alexa488	97% (Alexa488)	-	0.80	6.03	0.190
		+10mM $Ca(OAc)_2$	0.75	5.97	0.182
		+10mM $Ca(OAc)_2$ + 1μM SP DNA	0.77	6.01	0.087
BcnI(C202S+K209C)-Alexa488	96.5% (Alexa488)	-	0.64	5.81	0.232
		+10mM $Ca(OAc)_2$	0.70	5.90	0.223
		+10mM $Ca(OAc)_2$ + 1μM SP DNA	0.79	6.03	0.092
BcnI(N18C+C202S)-Alexa546	98.2% (Alexa546)	-	-	-	0.231
		+10mM $Ca(OAc)_2$	-	-	0.245
		+10mM $Ca(OAc)_2$ + 1μM SP DNA	-	-	0.251
BcnI(V105C+C202S)-Alexa546	100% (Alexa546)	-	-	-	0.248
		+10mM $Ca(OAc)_2$	-	-	0.249
		+10mM $Ca(OAc)_2$ + 1μM SP DNA	-	-	0.215
BcnI(N18C+V105C+C202S)-Alexa488-Alexa546	94.5% (Alexa488) 57.7% (Alexa546)	-	-	-	-

3.2.6. Conformational states of BcnI

The single molecule FRET measurements on freely diffusing BcnI(N18+V105C+C202S)-Alexa488-Alexa546 proteins were performed using

an inverted confocal microscope using various assay conditions: without DNA, with non-specific (NSP) DNA, and with specific (SP) DNA, all in the absence and in the presence of Ca^{2+} ions (Figure 18A-C). In the absence of DNA and Ca^{2+} ions, the mean FRET efficiency (E_{FRET}=0.61) correlated with the theoretical FRET efficiency of apo-BcnI (E_{FRET}=0.63, r=5.51 nm (Figure 15A), R_0=6 nm (Table 6)). The broad E_{FRET} histogram (σ=0.41, Figure 18A and Table 7) indicates that under these conditions BcnI is flexible and the DNA recognition and catalytic subdomains do not have defined positions relative to each other. The low-FRET part of the distribution presumably corresponds to the BcnI conformations that are more 'open' than observed in the apo-structure (Figure 15A), whereas the high-FRET part of the distribution indicates that a comparable fraction of BcnI molecules exist in a more closed conformation, which is reminiscent of the DNA-bound structure (E_{FRET}=0.89, r=4.2 nm (Figure 15B-C), R_0=6 nm (Table 6)). Addition of NSP or SP DNA resulted in significantly narrower distributions for the E_{FRET} values (σ=0.2), indicative of a more defined BcnI conformation, but the E_{FRET} values in both experiments remained low (0.51-0.53, Figure 18B-C). This is consistent with the lack of SP/NSP DNA discrimination by BcnI in the absence of divalent metal ions (K_d(BcnI-DNA_{NSP})=870 nM, K_d(BcnI-DNA_{SP})=540 nM, see 2.2.5., unpublished data). BcnI forms slightly more closed complexes with both DNAs in the presence of Ca^{2+} (E_{FRET}=0.57, Figure 18B-C), albeit a narrower E_{FRET} distribution observed with SP DNA (σ=0.09 for SP DNA *vs* 0.21 for NSP DNA) suggests that the conformation of BcnI with SP DNA is less flexible, i.e. better defined. These findings revealed that in solution DNA-bound BcnI conformation differs from crystallographic structure conformation, but SP DNA stabilizes BcnI conformation. Interestingly, similar E_{FRET} values distributions for BcnI with SP and NSP DNA (Figure 18B-C), suggesting that during target search (sliding), BcnI encircles DNA in a similar way as in the specific complex.

Surprisingly, the highest E_{FRET} value of 0.72 was observed for apo-BcnI in the presence of Ca^{2+} (Figure 18A, Table 7).

Table 7. FRET efficiency values. FRET efficiency (see 3.2.6. and 3.2.8.1.) mean (μ) and standard deviation (σ) values from normal distribution fits to confocal single molecule FRET results.

BcnI conjugate	Conditions	E_{FRET}	
		$\mu \pm s.e.m.$	$\sigma \pm s.e.m.$
BcnI(N18C+V105C+C202S)-Alexa488-Alexa546	-	0.61±0.04	0.41±0.05
BcnI(N18C+V105C+C202S)-Alexa488-Alexa546	10 mM $Ca(OAc)_2$	0.72±0.04	0.12±0.01
BcnI(N18C+V105C+C202S)-Alexa488-Alexa546	nsp DNA	0.51±0.01	0.2±0.02
BcnI(N18C+V105C+C202S)-Alexa488-Alexa546	nsp DNA+10 mM $Ca(OAc)_2$	0.58±0.02	0.21±0.02
BcnI(N18C+V105C+C202S)-Alexa488-Alexa546	sp DNA	0.53±0.01	0.14±0.01
BcnI(N18C+V105C+C202S)-Alexa488-Alexa546	sp DNA+10 mM $Ca(OAc)_2$	0.57±0.01	0.09±0.02
BcnI(N18C+C202S)-Alexa488	Alexa546-C-DNA+ 10 mM Ca(OAc)	0.35±0.04	0.11±0.01
		0.69±0.01	0.15±0.04
BcnI(N18C+C202S)-Alexa488	Alexa546-G-DNA+ 10 mM Ca(OAc)	0.26±0.01	0.11±0.01
		0.62±0.07	0.2±0.06
BcnI(V105C+C202S)-Alexa488	Alexa546-C-DNA+ 10 mM Ca(OAc)	0.3±0.02	0.1±0.01
		0.6±0.1	0.13±0.1
BcnI(V105C+C202S)-Alexa488	Alexa546-G-DNA+ 10 mM Ca(OAc)	0.31±0.1	0.29±0.1
		0.68±0.01	0.1±0.02
BcnI(C202S+K209C)-Alexa488)	Alexa546-C-DNA+ 10 mM Ca(OAc)	0.24±0.01	0.11±0.01
		0.61±0.03	0.13±0.03
BcnI(C202S+K209C)-Alexa488	Alexa546-G-DNA+ 10 mM Ca(OAc)	0.16±0.06	0.25±0.06
		0.68±0.01	0.09±0.01

Presumably, Ca^{2+} coordination by the negatively charged side chains in the DNA binding cleft brings the catalytic and recognition subdomains into close proximity. Noteworthy, the observed changes in FRET efficiencies upon addition of DNA/Ca^{2+} were not due to changes of the relative orientations of the dye dipoles, since the dye mobilities as measured by the fluorescence anisotropies of single labelled BcnI were not affected by the presence of Ca^{2+} (Table 6).

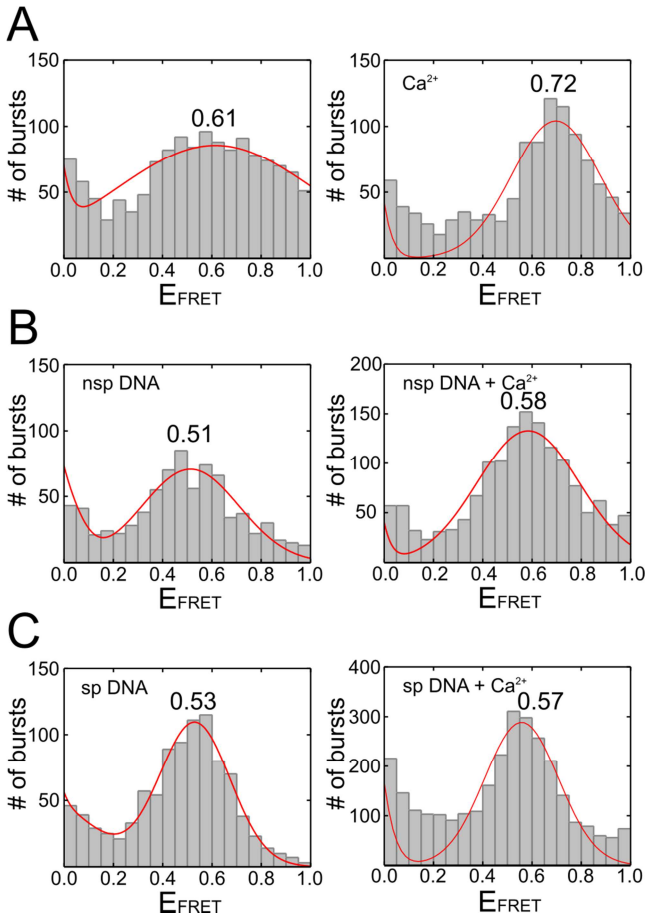

Figure 18. BcnI conformational dynamics in the absence and in the presence of DNA. Single molecule FRET experiments were performed with double-labelled BcnI(N18C+V105C+C202S)-Alexa488-Alexa546 using a confocal microscope. FRET efficiency histograms obtained for double-labelled BcnI(N18C+V105C+C202S)-Alexa488-Alexa546 in the absence or presence of Ca^{2+} ions are shown for BcnI only (A), BcnI in the presence of non-specific DNA (B) and BcnI in the presence of specific DNA (C).

3.2.7. Dynamics of the non-cognate BcnI-DNA interactions

3.2.7.1. 1-D diffusion and jumping of single BcnI molecule on DNA

Bulk kinetic data suggested that the flip of the BcnI orientation (Figure 14), which is required to complete the dsDNA cleavage reaction, involves sliding and/or hopping of enzyme molecule on the nonspecific DNA surrounding the

recognition site (Sasnauskas et al., 2011). To visualize the motion of individual BcnI molecules on stretched DNA molecules and to determine the quantitative parameters for the dynamics of the BcnI-nonspecific DNA interactions, we employed a custom-built experimental setup, which combines total internal reflection fluorescence (TIRF) microscopy with magnetic tweezers (Schwarz et al., 2013). A 22.8 kbp DNA fragment devoid of BcnI recognition sequences was immobilized between the bottom surface of a flow cell and a magnetic bead. The magnetic tweezers were used to stretch the DNA construct laterally such that the DNA molecules were almost parallel to the glass surface. The binding and movement of individual quantum dot-labelled BcnI molecules was observed using the TIRF unit of the setup (see 2.2.11.3., Figure 19A). Enzyme binding resulted in the appearance of diffraction limited fluorescence spots at random positions on the DNA. Following binding, the enzyme molecules were mobile and moved along the DNA. Two types of motion could be distinguished: 1D diffusion of BcnI resulting in a continuous change of the BcnI position along the DNA axis, as well as abrupt changes of the BcnI position (≥100 nm between two consecutive frames separated by 100 ms) that were interpreted as jumps, i.e. dissociation of BcnI and re-association with the DNA at a distant site. Taking into account the subnanomolar concentration of BcnI used in the experiments and the frequency of association of new BcnI molecules, arrival of a second BcnI molecule during a single time frame (100 ms) during the jump event is highly improbable (Bonnet et al., 2008).

1-D diffusion of BcnI on DNA was tested in the absence of divalent metal ions, in the presence of Ca^{2+}, and in the presence of Mg^{2+} ions. In the absence of divalent cations diffusion events of BcnI appeared to be long-lived and without jumps. In contrast, in the presence of Mg^{2+} and Ca^{2+}, the diffusion events were shorter and frequently terminated by jumps or dissociation events (Figure 19B).

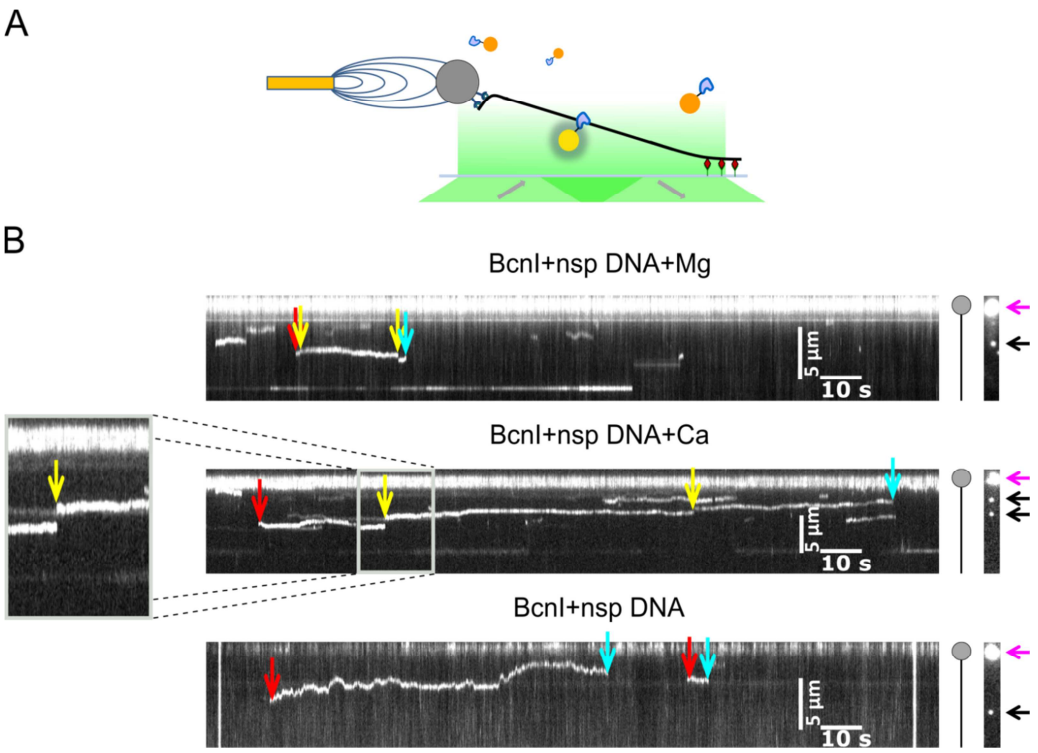

Figure 19. BcnI sliding and jumping on DNA. (A) Experimental configuration. A 22.8 kbp DNA molecule lacking BcnI recognition sites (black) was attached to a magnetic bead (grey sphere) and to the surface of a flow cell. The DNA was stretched side-wards using a magnet placed next to the flow cell. An evanescent field (green) of a TIRF-microscope was illuminating quantum-dot labelled enzymes bound to the DNA (yellow). Most of the freely diffusing enzymes in solution (orange) were outside of the evanescent field. (B) Representative kymographs of the movement of quantum-dot labelled BcnI on the DNA in the presence of Mg^{2+} ions (top) (straight horizontal line in the lower part of the kymograph depicts protein stuck on the surface of the flow cell), in the presence of Ca^{2+} ions (middle), and without divalent metal ions (bottom). Protein association, jumps, and protein dissociation are marked with red, green and blue arrows, respectively. Positions of the magnetic bead and fluorescent BcnI proteins are marked on the right-hand side with magenta and black arrows, respectively.

From the time trajectories of enzyme position during diffusion on DNA, mean-square displacement (MSD) *vs* time plots were calculated and used to estimate the 1D diffusion coefficients (D_{1D}). We found that the diffusion coefficient D_{1D} for 1-dimensional sliding of BcnI on the DNA is 1.7×10^{-2} µm^2/s in the absence of divalent metal ions, 0.8×10^{-2} µm^2/s in the presence of 10 mM Ca^{2+}, and 0.4×10^{-2} µm^2/s in the presence of 10 mM Mg^{2+} (Figure 20A). 1D diffusion

constants in the order of 1×10^{-2} $\mu m^2/s$ were also reported for other DNA-interacting enzymes (Bonnet and Desbiolles, 2011; Bonnet et al., 2008; Dikic et al., 2012; Gorman et al., 2007, 2010; Granéli et al., 2006; Harada et al., 1999; Kim and Larson, 2007; Komazin-Meredith et al., 2008; Laurence et al., 2008; Wang et al., 2006). D_{1D} is at least 1000-fold lower than the calculated 3-dimensional diffusion coefficient D_{3D} of the Qdot-labelled BcnI (30 $\mu m^2/s$) (Halford, 2004; Wilkins et al., 1999). This drastic reduction, also observed for other DNA-acting enzymes (Bonnet et al., 2008), can be attributed to the hydrodynamics of the quantum-dot conjugated enzyme during its helical path around the DNA helix (Bagchi et al., 2008; Schurr, 1979), as well as DNA-protein interactions during the sliding process (Slutsky and Mirny, 2004). Slower diffusion in the presence of divalent metal ions correlates with the more closed BcnI conformation observed in the presence of Ca^{2+} and DNA (Figure 18). Such tighter contacts between enzyme and non-cognate DNA may be required for probing the DNA sequence and recognition of the cognate site.

Current theoretical and experimental studies indicate that target site localization by site-specific proteins involves both 1D sliding along the DNA, which allows probing of all DNA sites in the scanned region, and 3D jumps, which relocate the protein to a nearby or a distant DNA site. A interplay of 1D and 3D diffusion may significantly accelerate target site location in comparison to a simple 3D search (Halford, 2004).

Along with protein sliding, our single molecule diffusion experiments revealed sudden translocations of BcnI on the DNA with a length of 100-1000 nm between two consecutive time frames (100 ms) (Figure 19 B, Figure 20 B). Such protein movements would require a diffusion coefficient of ~0.1-10 $\mu m^2/s$, which is significantly higher than the 1D diffusion coefficient D_{1D} discussed above (Bonnet et al., 2008). We therefore attribute these BcnI movements to 3D jumps on the DNA. Intriguingly, we find that the jump frequency is significantly lower

in the absence of divalent metal ions (on average, one ≥100 nm translocation every 160 s) than in the presence of Ca^{2+} and Mg^{2+} (one translocation every 20-25 s, Figure 19 B), indicating that metal ions facilitate enzyme dissociation from the DNA. As with EcoRV (Bonnet et al., 2008; Loverdo et al., 2009), the jump frequency decreased with the jump length (Figure 20 B). Due to the spatial resolution of our experimental setup, jumps shorter than 100 nm could not be detected, but their frequency could be estimated using a theoretical model developed by Kolesov et al., stating that each jump is on average accompanied by ~5 hops (i.e. jumps shorter than 50 nm, a single DNA persistence length) (Kolesov et al., 2007) This gives us the upper estimate of the average BcnI sliding duration, ~30 (150/5) s in the absence of divalent metal ions, and ~4 (20/5) s in the presence of Ca^{2+}/Mg^{2+}. Given the experimentally determined 1D diffusion coefficients, the average BcnI sliding length [$l_{sl}=(2\cdot D_{1D}\cdot t)^{0.5}$] in the absence of divalent metal ions is ~1000 nm or 3500 bp, and up to ~200 nm or 700 bp in the presence of Mg^{2+} or Ca^{2+}. Note that the sliding length could be up to 2-fold longer for a Qdot-free BcnI, given the smaller hydrodynamic radius of the unlabelled protein (Dikic et al., 2012). The sliding distance of BcnI estimated here is consistent with a high processivity of BcnI on DNA substrates with inter-site distance as large as 500 bp (Figure 21).

According to Halford and Marko (Halford, 2004), acceleration of the target site localization rate (k_a) beyond the diffusion-limited value ($D_{3D}\cdot a$) is expressed by eq. (51):

$$\frac{k_a}{D_3 a} = \left(\frac{a}{l_{sl}} + \frac{D_3}{D_1} a L l_{sl} c\right)^{-1} \quad (51)$$

Assuming a=1.7 nm (length of the 5 bp BcnI recognition site), L=1000 nm (length of a 3000 bp DNA fragment), c=1×10^{-10} nm^{-3} (~0.1 nM target site concentration expressed as the number of molecules per cubic nanometer), and using the sliding length (l_{sl}) and diffusion coefficients (D_{1D}, D_{3D}) estimated in the

present study, a quite significant acceleration in the presence of divalent metal ions of 3- to 8-fold is obtained. Intriguingly, divalent metal ions seem to play a dual role in the nonspecific BcnI-DNA interactions: they decrease the 1D diffusion coefficient D_{1D} (presumably due to tighter protein-DNA interactions in the presence of divalent ions), and simultaneously increase the protein dissociation rate (or jumping frequency).

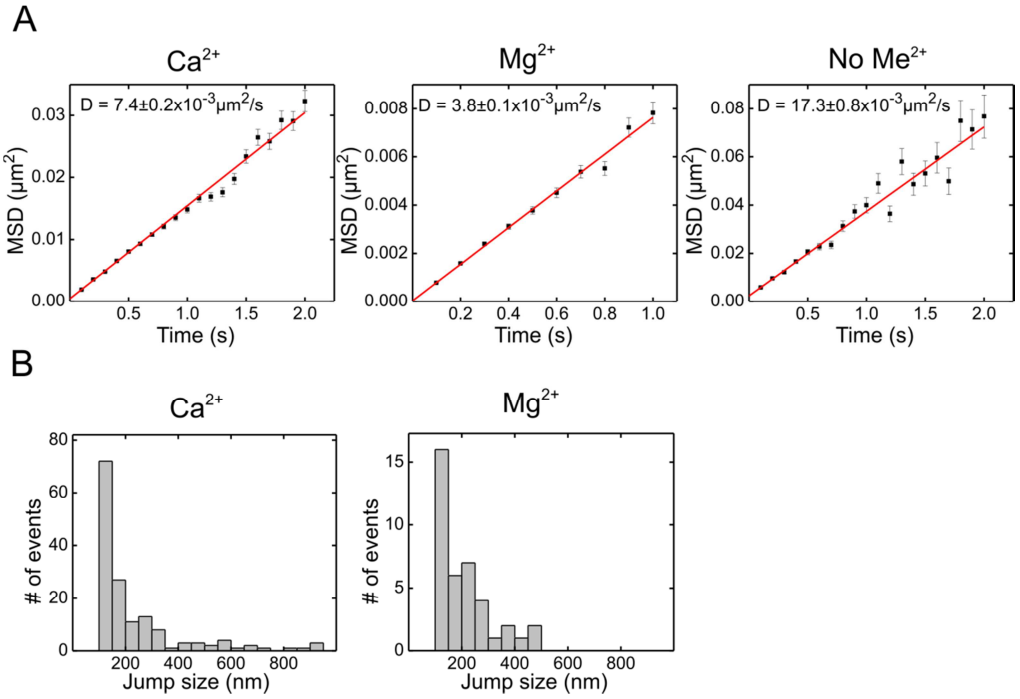

Figure 20. BcnI 1D diffusion coefficients and jump sizes. (A) Mean square displacements as a function of time for the motion of BcnI along DNA in the absence of divalent ions or in the presence of Ca^{2+} and Mg^{2+}. The diffusion constants D_{1D} where obtained from linear fits to the data at short times (red lines). (B) Jump size distribution of BcnI in the presence of Mg^{2+} and Ca^{2+}. Jumps in the absence of divalent ions were too rare to obtain statistically meaningful data.

3.2.7.2. BcnI processivity

To obtain an independent estimate of the BcnI sliding length, we have also measured the processivity of BcnI, being defined as the ability of the enzyme to act on multiple recognition sites during a single binding event. It is analogous to reactions of some orthodox restriction endonucleases on DNA substrates bearing

two (or more) recognition sites, that upon cleavage of the first recognition site remain associated with the surrounding nonspecific sequences and may diffuse to another target site on the same DNA molecule and cleave it (see 1.3.6.1.). The extensive 1D diffusion of BcnI on dsDNA suggested that the processive action of BcnI should extend to long inter-site distances. To test the processivity of BcnI, we performed BcnI cleavage reactions (see 2.2.6.3.) on two-site DNA fragments with inter-site distances of either 100 or 500 bp (see 2.2.4.3., Figure 8C). The maximal processivity of BcnI (equivalent to the fraction of DNA molecules cleaved at both sites during a single BcnI binding event) is expected to be 50 %, since upon cleavage of the first recognition site there is only a ~50 % probability for BcnI to remain on the fragment with the second recognition site (the other ~50 % of BcnI will remain associated with the fragment devoid of the second recognition site, see Figure 21C). The processivity of BcnI was determined as $|v_{PP}/v_{SS}|$ being the ratio of the initial rates of formation of the double-cut product v_{PP} and of the total cleavage rate of the uncut substrate v_{SS} .It is thus the fraction of the double-cut products among all cleaved DNAs at early time points. The measured processivity approaches the theoretical maximum of 50%, when the diffusion of BcnI to the second recognition site and its subsequent cleavage is much faster than the dissociation from the fragment ($k_{cross} >> k_{diss}$). Considering the competition between these two processes in case that they occur at similar rates, one can express the processivity as $50\ \% \times k_{cross}/(k_{cross}+k_{diss})$.

To gain insight into the processivity of BcnI, amounts of uncut, single cut (corresponds to non-processive cleavage reaction) and double-cut (corresponds to processive BcnI reaction) DNA forms (Figure 21A) were quantified at different reaction time points and the processivity was determined from the ratio $|v_{PP}/v_{SS}|$ (Figure 21B). We find that BcnI processively cuts ~41-43 % of both double-site fragments tested, indicating that k_{cross} is ~4-fold higher than k_{diss}. Thus, BcnI is

able to locate DNA sites 100 bp or 500 bp away from the search start position with high efficiency.

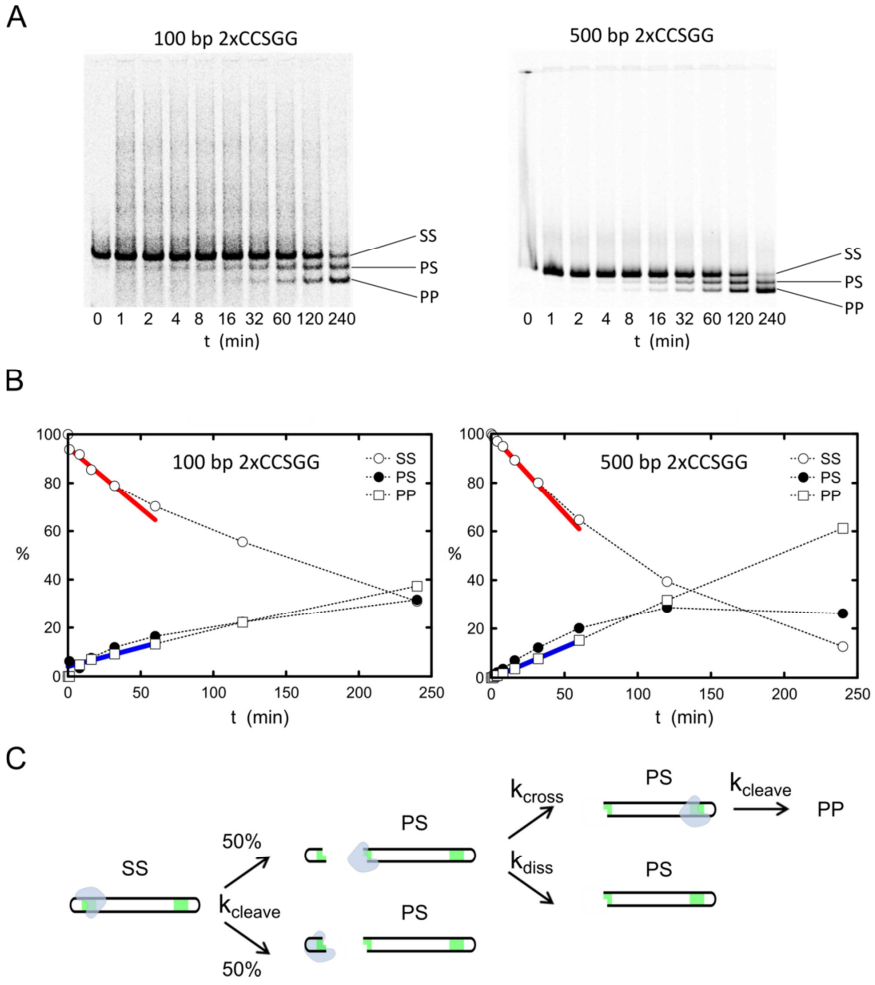

Figure 21. Representation of BcnI reactions on the two-site DNA substrates. Steady-state kinetic experiments (see 2.2.6.3.) were performed with BcnI and 135 and 535 bp two-site DNA (2×CCSGG) substrates (inter-site distances 100 bp or 500 bp, respectively, see Figure 8C). (A) Uncut (SS), single cut (PS) and double-cut (PP) DNA forms were separated by polyacrylamide gel electrophoresis and (B) amounts of different DNA forms were determined by densitometric analysis of gel images. The initial rates of the SS DNA cleavage and formation of the PP product were calculated by linear regression. (C) Reaction scheme. Processive cleavage of the two-site substrate is possible only if upon cleavage of the first recognition site BcnI remains associated with the DNA fragment containing the second recognition site (probability 1/2) and then locates the second site before dissociation from the DNA [probability $k_{cross}/(k_{cross}+k_{diss})$]. The calculated processivity of BcnI (the fraction of processively cleaved DNA) was equal to 0.43 for the "135" and 0.41 for the "535" fragment.

3.2.8. Site-specific BcnI-DNA interactions

3.2.8.1. BcnI orientation on DNA

BcnI recognizes the pseudopalindromic DNA recognition sequence 5′-CC(C/G)GG-3′. Being an asymmetric monomeric protein with a single catalytic site, BcnI can bind the recognition sequence in two orientations, i.e. by placing the catalytic center either in the vicinity of the ‘C’ (5′-CC<u>C</u>GG-3′) strand (the ‘C’ binding orientation), or in the vicinity of the ‘G’ (5′-CC<u>G</u>GG-3′) strand (the ‘G’ binding orientation). Cleavage of double-stranded DNA by BcnI therefore must involve sequential binding of the enzyme in both orientations and cleavage of the corresponding DNA strands (Figure 22). Though the structures of both types of BcnI-DNA complexes were solved (PDB IDs 2ODI and 3IMB) (Figure 15), (Sokolowska et al., 2007), bulk studies demonstrated that BcnI cleaves the majority of DNA *via* an intermediate with a nick in the ‘G’ strand, implying that the ‘G’ binding orientation is preferred by BcnI (Sasnauskas et al., 2011). To test this prediction, we performed single molecule FRET measurements of freely diffusing protein-DNA complexes in a confocal detection scheme (see 2.2.11.1.).

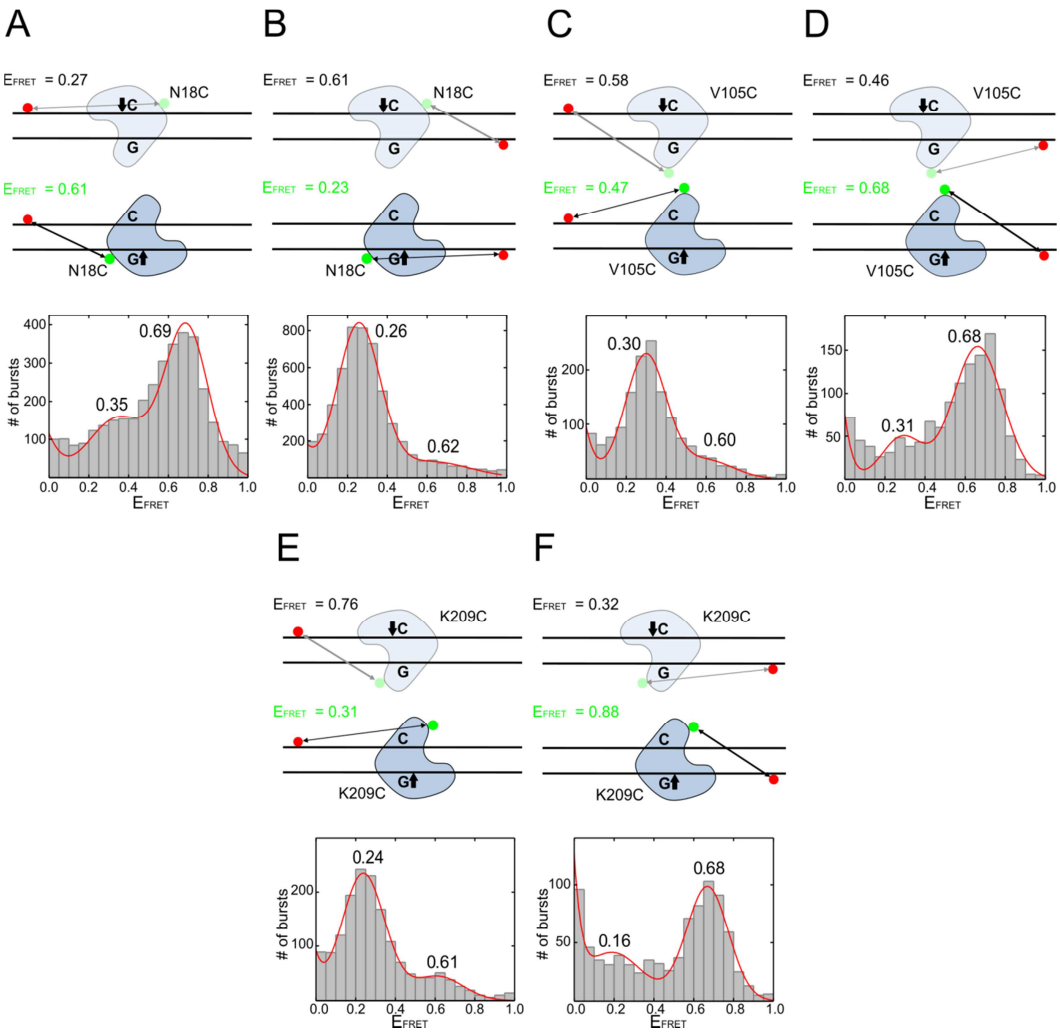

Figure 22. BcnI preferred binding orientation. Single molecule FRET experiments were performed with Alexa488-labelled BcnI(N18C+C202S) and Alexa546-labelled DNA. (A) FRET efficiency histogram obtained for 'C' strand-labelled DNA. Based on the available structures of BcnI-DNA complexes (PDB IDs 2ODI and 3IMB), the expected distance between the Alexa488 (green sphere) and Alexa546 (red sphere) dyes is 71.3 and 56.2 Å for the different orientations of the protein-DNA complexes. This is equivalent to FRET efficiencies of 0.27 and 0.61 for protein bound in the 'C' and 'G' orientations, respectively (see sketches at the top, see 3.2.2., Table 4). A double-Gaussian fit to the FRET efficiency data (red line) is consistent with preferred binding of BcnI in the 'G' orientation. (B) FRET efficiency histogram obtained for 'G' strand-labelled DNA. The expected FRET efficiencies are 0.61 and 0.23 for protein bound in the 'C' and 'G' orientations, respectively (see sketches at the top). As with the 'C' strand-labelled DNA, the experimental data is consistent with the preferential binding in the 'G' orientation. Expected theoretical E_{FRET} values and single molecule experiments data for Alexa488-labelled BcnI(V105C+C202S) and Alexa488-labelled BcnI(C202S+K209C) are depicted in (C), (D) and in (E), (F) respectively. R_0 values determined for BcnI conjugates with Ca^{2+} and DNA are listed in Table 6.

Measurements with BcnI(N18C+C202S)-Alexa488 and Alexa546-C-DNA revealed two E_{FRET} populations: a less abundant with a low FRET efficiency (E_{FRET}=0.35) and a more abundant with a high FRET efficiency (E_{FRET}=0.69, Figure 22A). Both values were in agreement with the theoretically expected FRET efficiencies for protein binding to the Alexa546-C-DNA in the 'C' and 'G' orientations of 0.27 and 0.61, respectively (Figure 22A). The opposite distribution was observed for the Alexa546-G-DNA, where the low E_{FRET} state (0.26) was more populated, and the high E_{FRET} state (0.62) was less populated, both values in good agreement with the expected values of 0.23 and 0.61 (Figure 22B). Thus, the single molecule FRET data obtained with both DNAs is consistent with a preferential binding of BcnI to DNA in the 'G' orientation. This conclusion is also supported by data obtained with BcnI(V105C+C202S)-Alexa488 and BcnI(C202S+K209C)-Alexa488 (Figure 22C-F, Table 7).

3.2.8.2. Dynamics of site-specific BcnI-DNA interactions

According to bulk kinetic measurements, BcnI rapidly localizes its specific recognition site (the lower limit for the bimolecular rate constant is 3×10^8 $M^{-1}s^{-1}$), followed by rapid cleavage of the first strand (first-order rate constant ~7 s^{-1}), and a subsequent slow cut of the second DNA strand (observed rate constant ~0.15-0.3 s^{-1} (Sasnauskas et al., 2011). The latter reaction stage must involve enzyme dissociation from the nicked intermediate, a switch in enzyme orientation, and DNA hydrolysis itself (Figure 14). Rapid cleavage of the pre-nicked DNA by BcnI (first-order rate constant ~10 s^{-1}) suggested that the rate-limiting step of the second DNA strand cleavage is enzyme dissociation from the nicked DNA. To probe the dynamics of BcnI-specific DNA interactions at the single molecule level, we employed a custom-built setup, which supports objective-type TIRF microscopy with simultaneous dual-color FRET detection (Kemmerich et al., 2015). Cy5-labelled 36 bp DNA oligoduplexes (Table 2) were attached to the

bottom surface of a flow cell and positions of the attached fluorescent oligoduplexes were determined by short illumination (~2 s) with a 642 nm laser. Upon injection of Cy3-labelled BcnI (final concentration 0.2 nM) into the flow cell, the BcnI-Cy3 conjugates were excited with a 532 nm laser (see 2.2.11.2.). Association of the Cy3-labelled BcnI with Cy5-labelled DNA correlated with a significant increase of fluorescence intensity in both the donor and the acceptor channels (Figure 23A). The durations of the events with significant FRET (apparent E_{FRET}>0.1) in the presence of Ca^{2+} (Ca^{2+} supports specific DNA binding but not cleavage by BcnI) were best described by a double exponential distribution indicative of two types of BcnI-DNA complexes (Figure 23B). The short-lived binding events (mean duration 0.35 s) were more frequent (~70 % of all events) than the long-lived binding events (mean duration 8.3 s). Presumably, the short BcnI-DNA association events correspond to non-specific enzyme-DNA complexes (target search intermediates), while longer association times correspond to specific enzyme-DNA interactions.

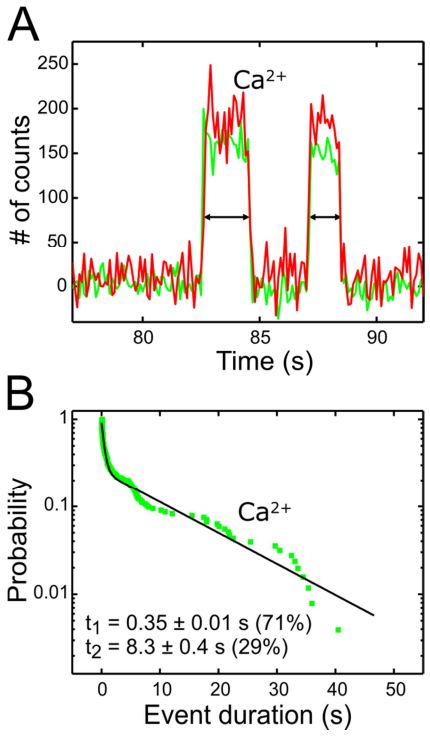

Figure 23. Dynamics of BcnI binding to its target site. Single molecule TRIF-based FRET experiments using surface-tethered 36 bp long Cy5-labelled DNA and Cy3-labelled BcnI(N18C+C202S). (A) Time trajectory of donor and acceptor fluorescence measured on a single DNA in the presence of Ca^{2+}. Arrows indicate the event duration times. (B) Cumulative distribution of the measured event durations. Double exponential fit to the data is shown as a solid line. Fit parameters are given next to the plot.

3.2.8.3. Kinetics of the DNA second strand cleavage

To directly assess the time required for a BcnI molecule to change its orientation on the recognition site after nicking of the first target strand, we employed magnetic tweezers to measure DNA cleavage (see 2.2.11.4.) (van Aelst et al., 2010; Rutkauskas et al., 2015). Different termini of the 7.4 kbp DNA construct with a single BcnI recognition site were attached to the bottom surface of a flow cell and a magnetic bead. Using a pair of magnets placed above the flow cell the DNA was held stretched at a tension of 2 pN, while being positively supercoiled. Introduction of 25 positive turns reduced the length of the DNA construct due to formation of a plectonemic superhelix (Figure 24A). Two events were observed upon addition of BcnI: first, the full DNA length was recovered due to nicking of the first strand, followed by the disappearance of the bead due to cleavage of the second DNA strand (Figure 24B). The cumulative distribution of time intervals between the first and the second strand nicking was fitted with a double-exponential function, yielding rate constants for the second strand cleavage $k_{obs}(1)$=0.3 ±0.1 s^{-1}(30% of cleavage events) and $k_{obs}(2)$=0.06±0.01 s^{-1} (70% of cleavage events) (Figure 24B inset).

These values are in good agreement with the second DNA strand cleavage rates determined from bulk kinetics, the rate constant $k_{obs}(G)$ for cleavage of the ‘G’ strand in the ‘C-nick’ intermediate (0.32 s^{-1}, ~30 % of all DNA), and the rate constant $k_{obs}(C)$ for cleavage of the ‘C’ strand in the ‘G-nick’ intermediate (0.14 s^{-1}, ~70 % of all DNA) (Sasnauskas et al., 2011). Thus, the slower cleavage events [$k_{obs}(2)$] observed in the single molecule setup may correspond to the predominant (70 %) DNA cleavage pathway, where ‘C’ strand is cleaved after the ‘G’ strand, and the more rapid cleavage events [$k_{obs}(1)$] may correspond to the alternative (30 %) pathway, where the cleavage order is reversed. The dominance of the ‘G-nick’

pathway in bulk kinetics (Sasnauskas et al., 2011) was attributed to preferential binding of BcnI to DNA in an orientation that places the catalytic center close to the 'G' strand. We now confirm this BcnI binding preference using single molecule FRET measurements with labelled BcnI and DNA (Figure 22). The second strand cleavage rate k_{obs} can be expressed by equation (52)

$$\frac{1}{k_{obs}} = \frac{1}{k_{dissoc}} + \frac{1}{k_{flip}} + \frac{1}{k_{chem}} \quad (52)$$

where k_{dissoc}, k_{flip} and k_{chem} are the rate constants for enzyme dissociation from nicked DNA, re-binding, and DNA hydrolysis, respectively. Since the hydrolysis step k_{chem} is rapid, 8-10 s^{-1}(see 3.1.1., 3.1.2.), and we show here that BcnI jumps on the DNA take less than 0.1 s (Figure 19 B), the rate limiting step for k_{obs}, must be k_{dissoc}, i. e. slow dissociation of BcnI from the nicked intermediate. Different k_{obs} values observed for the 'G-nick' and 'C-nick' reaction pathways must therefore reflect different enzyme dissociation rates from the 'G-nick' and the 'C-nick' intermediates. Here slower dissociation from the 'G-nick' intermediate prior to 'C' strand cleavage correlates with tighter enzyme binding in the 'G' orientation.

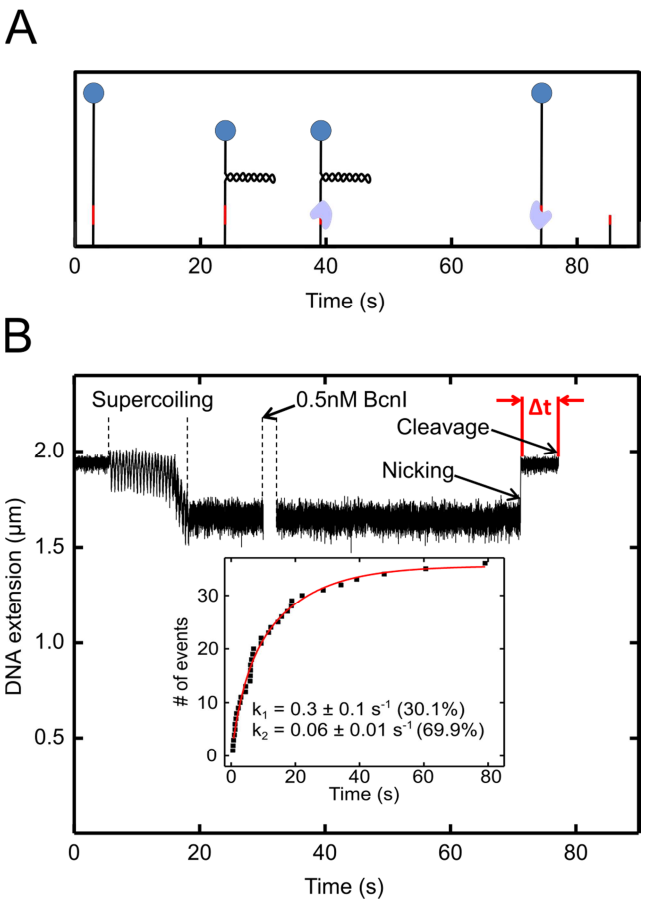

Figure 24. Single DNA molecule cleavage by BcnI. (A) Scheme of the experiment. A 7.4 kbp DNA fragment with a single BcnI recognition site was attached to the flow cell surface and a magnetic bead. The DNA was held stretched at 2 pN force and supercoiled with +25 turns. Subsequently, 0.2-1 nM BcnI was added. DNA nicking recovered the initial DNA length and cleavage of the second DNA strand released the bead. The time interval *Δt* between these two events is the lifetime of the nicked intermediate, or the inverse of the second DNA strand cleavage rate. (B) Experimental results. The cumulative distribution of the measured *Δt* values is shown in the inset. A double-exponential fit yielded $k_{obs}(1)$=0.3±0.1 s^{-1} (~30 % events) and $k_{obs}(2)$=0.06±0.01 s^{-1} (~70 % events).

Taken together, we have performed a thorough study of the monomeric restriction enzyme BcnI-DNA interactions, employing a diverse set of single molecule techniques. This allowed us to characterize reaction steps that are difficult or impossible to access using conventional techniques, for example, direct observation of 1D diffusion and jumping of the protein on the DNA, protein binding orientation and conformational dynamics, and dynamics of specific and non-specific protein-DNA interactions. Our results confirm the BcnI reaction mechanism proposed from bulk solution studies, and provide additional mechanistic details, such as enzyme-DNA dissociation times, sliding length and

jumping frequency of the protein. The set of single-molecule techniques described here could be successfully applied to other DNA-interacting proteins.

CONCLUSIONS

- To generate a double-strand break BcnI binds the 5′-CCSGG-3′ recognition sequence in one orientation, cleaves the first DNA strand, switches its orientation on DNA and then cleaves the second DNA strand.
- The rate limiting step for the second DNA strand cleavage is the switch in enzyme orientation, which occurs without an excursion into bulk solution, as the same BcnI molecule acts processively on both DNA strands.
- Target site location and the switch in BcnI orientation involve sliding and jumping of the enzyme on the nonspecific DNA; sliding and jumping also enable processive cleavage of multiple BcnI target sites located as far as 500 bp apart.
- The DNA-binding cleft, formed by the catalytic and DNA recognition subdomains of apo-BcnI is relatively wide and flexible; DNA and divalent metal ion binding brings the catalytic and recognition subdomains into close proximity.

LIST OF PUBLICATIONS

The thesis is based on the following original publications:

1. Sasnauskas G, **Kostiuk G**, Tamulaitis G and Siksnys V (2011) Target site cleavage by the monomeric restriction enzyme BcnI requires translocation to a random DNA sequence and a switch in enzyme orientation. Nucleic Acids Res., 39, 8844-56.

2. **Kostiuk G‡,** Dikic J‡, Schwarz F W, Sasnauskas G, Seidel R. and Siksnys V (2017). The dynamics of the monomeric restriction endonuclease BcnI during its interaction with DNA. Nucleic Acids Res. doi: 10.1093/nar/gkx294. [Epub ahead of print]

‡ – authors contributed equally to this work.

Other publications:

3. **Kostiuk G**, Sasnauskas G, Tamulaitiene G and Siksnys V (2011) Degenerate sequence recognition by the monomeric restriction enzyme: single mutation converts BcnI into a strand-specific nicking endonuclease. Nucleic Acids Res., 39, 3744–3753.

4. Kazlauskiene M, Tamulaitis G, **Kostiuk G**, Venclovas Č, Siksnys V. (2016) Spatiotemporal Control of Type III-A CRISPR-Cas Immunity: Coupling DNA Degradation with the Target RNA Recognition. Mol. Cell., 62(2), 295-306.

CONFERENCE PRESENTATIONS

1. Dikic J, **Kostiuk G**, Siksnys V, Seidel R. Protein diffusion on DNA. Diffusion fundamentals V. Leipzig, Germany, 2013.08.26-28.

2. **Kostiuk G**, Dikić J, Sasnauskas G, Seidel R and Siksnys V. Monomeric restriction enzyme diffusion on DNA. IRTG-workshop. Sankt Petersburg, Russia, 2013.09.17-20.

3. Dikic J, **Kostiuk G**, Siksnys V, Seidel R. Single molecule analysis of monomeric restriction enzyme BcnI. Machines on genes: Nucleic Acids Enzymes. Snowmass Village, Colorado, USA, 2014.06.22-27.

4. **Kostiuk G**, Dikic J, Sasnauskas G, Seidel R and Siksnys V. Single molecule analysis on restriction enzyme BcnI. Single biomolecules – in silico, in vitro and in vivo. Hertfordshire, UK, 2014.09.11-13.

5. **Kostiuk G**, Dikić J, Sasnauskas G, Seidel R and Siksnys V. Single-molecule analysis of the monomeric restriction enzyme BcnI. 7th New England Biolabs Meeting on Restriction and Modification. Gdansk, Poland, 2015.08.24-29.

FINANCIAL SUPPORT

The work was supported by the European Social Fund under the Global Grant measure (project R100), Research Council of Lithuania (KEL-11460, DOC-13060) and European Union Research Potencial Cal FP7-REGPOT-2009-1 [245721 ‚MoBiLi' project]. Scholarships for academic achievement were recieved from the Research Council of Lithuania.

ACKNOWLEDGEMENTS

I am very appreciative to my supervisor prof. V. Šikšnys for opportunity to work in the Department of protein – DNA interactions, for interdisciplinary topic, valuable discussions, motivation and for annual laboratory retreat.

I am very indebted to my supervisor dr. G. Sasnauskas for valuable discussions, critical remarks and for help arranging publications and dissertation.

I am grateful to prof. R. Seidel (Leipzig University) for opportunity to conduct single molecule experiments in DNA motors laboratory ir Dresden Technical and Munster universities.

I am grateful to dr. J. Dikić (Leipzig University) for help and provided skills conducting single molecule experiments, data analysis and for DNR constructs.

I am thankful to dr. F.W. Schwarz (Dresden Technical University) for first single molecule experiments lessons.

I am grateful to my first supervisor dr. G. Tamulaitienė for guidance conducting first experiments and for supervision during Bachelor‘s and Master‘s thesis work.

I thank to dr. A. Šilanskas for help performing first BcnI labelling experiments and for good mood in our office.

I am grateful to all my colleagues for valuable discussions and motivation.

I am grateful to my chemistry teacher L. Kvedaravičienė for interesting chemistry lessons and for encourage to study biochemistry.

I am very appreciative to all my family members and friends for support and motivation, especially to my wife Ingrida and my mother Olga.

REFERENCES

1. Adam, G., and Delbruck, M. (1968). Reduction of Dimensionality in Biological Diffusion Processes. In Structural Chemistry and Molecular Biology, (San Francisco: W. H. Freeman), pp. 198–215.
2. Adams, C.D., Schnurr, B., Marko, J.F., and Reznikoff, W.S. (2007). Pulling Apart Catalytically Active Tn5 Synaptic Complexes Using Magnetic Tweezers. J. Mol. Biol. *367*, 319–327.
3. van Aelst, K., Toth, J., Ramanathan, S.P., Schwarz, F.W., Seidel, R., and Szczelkun, M.D. (2010). Type III restriction enzymes cleave DNA by long-range interaction between sites in both head-to-head and tail-to-tail inverted repeat. Proc. Natl. Acad. Sci. *107*, 9123–9128.
4. Aitken, C.E., Marshall, R.A., and Puglisi, J.D. (2008). An Oxygen Scavenging System for Improvement of Dye Stability in Single-Molecule Fluorescence Experiments. Biophys. J. *94*, 1826–1835.
5. Allemand, J.F., Bensimon, D., Lavery, R., and Croquette, V. (1998). Stretched and overwound DNA forms a Pauling-like structure with exposed bases. Proc. Natl. Acad. Sci. *95*, 14152–14157.
6. Aregger, R., and Klostermeier, D. (2009). The DEAD Box Helicase YxiN Maintains a Closed Conformation during ATP Hydrolysis. Biochemistry *48*, 10679–10681.
7. Armalyte, E., Bujnicki, J.M., Giedriene, J., Gasiunas, G., Kosinski, J., and Lubys, A. (2005). Mva1269I: A Monomeric Type IIS Restriction Endonuclease from Micrococcus Varians with Two EcoRI- and FokI-like Catalytic Domains. J. Biol. Chem. *280*, 41584–41594.
8. Atwell, S., Disseau, L., Stasiak, A.Z., Stasiak, A., Renodon-Corniere, A., Takahashi, M., Viovy, J.-L., and Cappello, G. (2012). Probing Rad51-DNA interactions by changing DNA twist. Nucleic Acids Res. *40*, 11769–11776.
9. Axelrod, D. (2001). Total internal reflection fluorescence microscopy in cell biology. Traffic *2*, 764–774.
10. Axelrod, D. (2003). Total internal reflection fluorescence microscopy in cell biology. Methods Enzymol. *361*, 1–33.
11. Axelrod, D., Burghardt, T.P., and Thompson, N.L. (1984). Total Internal Reflection Fluorescence. Annu. Rev. Biophys. Bioeng. *13*, 247–268.
12. Bacia, K., and Schwille, P. (2007). Practical guidelines for dual-color fluorescence cross-correlation spectroscopy. Nat. Protoc. *2*, 2842–2856.
13. Bagchi, B., Blainey, P.C., and Xie, X.S. (2008). Diffusion Constant of a Nonspecifically Bound Protein Undergoing Curvilinear Motion along DNA †. J. Phys. Chem. B *112*, 6282–6284.
14. Basu, A., Parente, A.C., and Bryant, Z. (2016). Structural Dynamics and

Mechanochemical Coupling in DNA Gyrase. J. Mol. Biol. *428*, 1833–1845.
15. Bellamy, S.R.W., Milsom, S.E., Scott, D.J., Daniels, L.E., Wilson, G.G., and Halford, S.E. (2005). Cleavage of Individual DNA Strands by the Different Subunits of the Heterodimeric Restriction Endonuclease BbvCI. J. Mol. Biol. *348*, 641–653.
16. BENESCH, R.E., and BENESCH, R. (1953). Enzymatic removal of oxygen for polarography and related methods. Science *118*, 447–448.
17. Berg, H.C. (1993). Rondom Walks in Biology (Princeton University Press).
18. Berg, O.G., and Blomberg, C. (1976). Association kinetics with coupled diffusional flows. Biophys. Chem. *4*, 367–381.
19. Berg, O.G., Winter, R.B., and Von Hippel, P.H. (1981). Diffusion-driven mechanisms of protein translocation on nucleic acids. 1. Models and theory. Biochemistry *20*, 6929–6948.
20. Berkhout, B., and van Wamel, J. (1996). Accurate Scanning of the BssHII Endonuclease in Search for Its DNA Cleavage Site. J. Biol. Chem. *271*, 1837–1840.
21. Biebricher, A., Wende, W., Escudé, C., Pingoud, A., and Desbiolles, P. (2009). Tracking of Single Quantum Dot Labeled EcoRV Sliding along DNA Manipulated by Double Optical Tweezers. Biophys. J. *96*, L50–L52.
22. Blainey, P.C., Luo, G., Kou, S.C., Mangel, W.F., Verdine, G.L., Bagchi, B., and Xie, X.S. (2009). Nonspecifically bound proteins spin while diffusing along DNA. Nat. Struct. Mol. Biol. *16*, 1224–1229.
23. Bonnet, I., and Desbiolles, P. (2011). The diffusion constant of a labeled protein sliding along DNA. Eur. Phys. J. E *34*, 25.
24. Bonnet, I., Biebricher, A., Porte, P.-L., Loverdo, C., Benichou, O., Voituriez, R., Escude, C., Wende, W., Pingoud, A., and Desbiolles, P. (2008). Sliding and jumping of single EcoRV restriction enzymes on non-cognate DNA. Nucleic Acids Res. *36*, 4118–4127.
25. Bouchiat, C., Wang, M.D., Allemand, J.-F., Strick, T., Block, S.M., and Croquette, V. (1999). Estimating the Persistence Length of a Worm-Like Chain Molecule from Force-Extension Measurements. Biophys. J. *76*, 409–413.
26. Capitanio, M., and Pavone, F.S. (2013). Interrogating Biology with Force: Single Molecule High-Resolution Measurements with Optical Tweezers. Biophys. J. *105*, 1293–1303.
27. Catto, L.E., Bellamy, S.R.W., Retter, S.E., and Halford, S.E. (2008). Dynamics and consequences of DNA looping by the FokI restriction endonuclease. Nucleic Acids Res. *36*, 2073–2081.
28. Chou, K., and Dennis, A. (2015). Förster Resonance Energy Transfer between Quantum Dot Donors and Quantum Dot Acceptors. Sensors *15*,

13288–13325.
29. Comstock, M.J., Whitley, K.D., Jia, H., Sokoloski, J., Lohman, T.M., Ha, T., and Chemla, Y.R. (2015). Direct observation of structure-function relationship in a nucleic acid-processing enzyme. Science (80-.). *348*, 352–354.
30. Dahan, M. (2003). Diffusion Dynamics of Glycine Receptors Revealed by Single-Quantum Dot Tracking. Science (80-.). *302*, 442–445.
31. Daldrop, P., Brutzer, H., Huhle, A., Kauert, D.J., and Seidel, R. (2015). Extending the Range for Force Calibration in Magnetic Tweezers. Biophys. J. *108*, 2550–2561.
32. Dawid, A., Croquette, V., Grigoriev, M., and Heslot, F. (2004). Single-molecule study of RuvAB-mediated Holliday-junction migration. Proc. Natl. Acad. Sci. *101*, 11611–11616.
33. Day, R.N., and Davidson, M.W. (2009). The fluorescent protein palette: tools for cellular imaging. Chem. Soc. Rev. *38*, 2887.
34. Day, R.N., and Davidson, M.W. (2012). Fluorescent proteins for FRET microscopy: Monitoring protein interactions in living cells. BioEssays *34*, 341–350.
35. Deibert, M. (1999). Crystal structure of MunI restriction endonuclease in complex with cognate DNA at 1.7 A resolution. EMBO J. *18*, 5805–5816.
36. DeRocco, V., Anderson, T., Piehler, J., Erie, D., and Weninger, K. (2010). Four-color single-molecule fluorescence with noncovalent dye labeling to monitor dynamic multimolecular complexes. Biotechniques *49*, 807–816.
37. Diamandis, E.P., and Christopoulos, T.K. (1991). The biotin-(strept)avidin system: principles and applications in biotechnology. Clin. Chem. *37*, 625–636.
38. Dikic, J., Menges, C., Clarke, S., Kokkinidis, M., Pingoud, A., Wende, W., and Desbiolles, P. (2012). The rotation-coupled sliding of EcoRV. Nucleic Acids Res. *40*, 4064–4070.
39. Dikić, J. (2009). Doctoral Dissertation. The conformational dynamics of BsoBI, analyzed by fluorescence spectroscopy down to the single molecule level. Justus-Liebig-Universität.
40. Ehbrecht, H.J., Pingoud, A., Urbanke, C., Maass, G., and Gualerzi, C. (1985). Linear diffusion of restriction endonucleases on DNA. J. Biol. Chem. *260*, 6160–6166.
41. Elf, J., Li, G.-W., and Xie, X.S. (2007). Probing Transcription Factor Dynamics at the Single-Molecule Level in a Living Cell. Science (80-.). *316*, 1191–1194.
42. Embleton, M.L., Siksnys, V., and Halford, S.E. (2001). DNA cleavage reactions by type II restriction enzymes that require two copies of their recognition sites. J. Mol. Biol. *311*, 503–514.

43. Erkens, G.B., Hänelt, I., Goudsmits, J.M.H., Slotboom, D.J., and van Oijen, A.M. (2013). Unsynchronised subunit motion in single trimeric sodium-coupled aspartate transporters. Nature *502*, 119–123.
44. Ernst, S., Düser, M.G., Zarrabi, N., and Börsch, M. (2012). Three-color Förster resonance energy transfer within single F[sub O]F[sub 1]-ATP synthases: monitoring elastic deformations of the rotary double motor in real time. J. Biomed. Opt. *17*, 11004.
45. Fan, J., Leroux-Coyau, M., Savery, N.J., and Strick, T.R. (2016). Reconstruction of bacterial transcription-coupled repair at single-molecule resolution. Nature *536*, 234–237.
46. Fish, K.N. (2009). Total Internal Reflection Fluorescence (TIRF) Microscopy. In Current Protocols in Cytometry, (Hoboken, NJ, USA: John Wiley & Sons, Inc.), pp. 1–13.
47. Gahl, R.F., Tekle, E., and Tjandra, N. (2014). Single color FRET based measurements of conformational changes of proteins resulting from translocation inside cells. Methods *66*, 180–187.
48. Gasiunas, G., Sasnauskas, G., Tamulaitis, G., Urbanke, C., Razaniene, D., and Siksnys, V. (2008). Tetrameric restriction enzymes: expansion to the GIY-YIG nuclease family. Nucleic Acids Res. *36*, 938–949.
49. Gorman, J., and Greene, E.C. (2008). Visualizing one-dimensional diffusion of proteins along DNA. Nat. Struct. Mol. Biol. *15*, 768–774.
50. Gorman, J., Chowdhury, A., Surtees, J.A., Shimada, J., Reichman, D.R., Alani, E., and Greene, E.C. (2007). Dynamic Basis for One-Dimensional DNA Scanning by the Mismatch Repair Complex Msh2-Msh6. Mol. Cell *28*, 359–370.
51. Gorman, J., Plys, A.J., Visnapuu, M.-L., Alani, E., and Greene, E.C. (2010). Visualizing one-dimensional diffusion of eukaryotic DNA repair factors along a chromatin lattice. Nat. Struct. Mol. Biol. *17*, 932–938.
52. Gowers, D.M., and Halford, S.E. (2003). Protein motion from non-specific to specific DNA by three-dimensional routes aided by supercoiling. EMBO J. *22*, 1410–1418.
53. Gowers, D.M., Wilson, G.G., and Halford, S.E. (2005). Measurement of the contributions of 1D and 3D pathways to the translocation of a protein along DNA. Proc. Natl. Acad. Sci. U. S. A. *102*, 15883–15888.
54. Granéli, A., Yeykal, C.C., Robertson, R.B., and Greene, E.C. (2006). Long-distance lateral diffusion of human Rad51 on double-stranded DNA. Proc. Natl. Acad. Sci. U. S. A. *103*, 1221–1226.
55. Gubaev, A., Hilbert, M., and Klostermeier, D. (2009). The DNA-gate of Bacillus subtilis gyrase is predominantly in the closed conformation during the DNA supercoiling reaction. Proc. Natl. Acad. Sci. *106*, 13278–13283.
56. Gust, A., Zander, A., Gietl, A., Holzmeister, P., Schulz, S., Lalkens, B.,

Tinnefeld, P., and Grohmann, D. (2014). A Starting Point for Fluorescence-Based Single-Molecule Measurements in Biomolecular Research. Molecules *19*, 15824–15865.
57. Ha, T. (2014). Single-molecule methods leap ahead. Nat. Methods *11*, 1015–1018.
58. Ha, T., and Tinnefeld, P. (2012). Photophysics of Fluorescent Probes for Single-Molecule Biophysics and Super-Resolution Imaging. Annu. Rev. Phys. Chem. *63*, 595–617.
59. Halford, S.E. (2004). How do site-specific DNA-binding proteins find their targets? Nucleic Acids Res. *32*, 3040–3052.
60. Halford, S.E. (2009). An end to 40 years of mistakes in DNA–protein association kinetics? Biochem. Soc. Trans. *37*, 343–348.
61. Harada, Y., Funatsu, T., Murakami, K., Nonoyama, Y., Ishihama, A., and Yanagida, T. (1999). Single-Molecule Imaging of RNA Polymerase-DNA Interactions in Real Time. Biophys. J. *76*, 709–715.
62. Hedglin, M., and O'Brien, P.J. (2008). Human Alkyladenine DNA Glycosylase Employs a Processive Search for DNA Damage †. Biochemistry *47*, 11434–11445.
63. van der Heijden, T., Modesti, M., Hage, S., Kanaar, R., Wyman, C., and Dekker, C. (2008). Homologous Recombination in Real Time: DNA Strand Exchange by RecA. Mol. Cell *30*, 530–538.
64. Heller, I., Hoekstra, T.P., King, G.A., Peterman, E.J.G., and Wuite, G.J.L. (2014). Optical Tweezers Analysis of DNA–Protein Complexes. Chem. Rev. *114*, 3087–3119.
65. Hendrix, J., and Lamb, D.C. (2013). Pulsed Interleaved Excitation. In Methods in Enzymology, (Elsevier Inc.), pp. 205–243.
66. Hickerson, R., Majumdar, Z.K., Baucom, A., Clegg, R.M., and Noller, H.F. (2005). Measurement of Internal Movements within the 30S Ribosomal Subunit Using Förster Resonance Energy Transfer. J. Mol. Biol. *354*, 459–472.
67. von Hippel, P.H., and Berg, O.G. (1989). Facilitated target location in biological systems. J. Biol. Chem. *264*, 675–678.
68. Hodeib, S., Raj, S., Manosas, M., Zhang, W., Bagchi, D., Ducos, B., Allemand, J.-F., Bensimon, D., and Croquette, V. (2016). Single molecule studies of helicases with magnetic tweezers. Methods *105*, 3–15.
69. Hohlbein, J., Aigrain, L., Craggs, T.D., Bermek, O., Potapova, O., Shoolizadeh, P., Grindley, N.D.F., Joyce, C.M., and Kapanidis, A.N. (2013). Conformational landscapes of DNA polymerase I and mutator derivatives establish fidelity checkpoints for nucleotide insertion. Nat. Commun. *4*, 1–11.
70. Hohlbein, J., Craggs, T.D., and Cordes, T. (2014). Alternating-laser

excitation: single-molecule FRET and beyond. Chem. Soc. Rev. *43*, 1156–1171.
71. Hohng, S., and Ha, T. (2005). Single-Molecule Quantum-Dot Fluorescence Resonance Energy Transfer. ChemPhysChem *6*, 956–960.
72. Hohng, S., Joo, C., and Ha, T. (2004). Single-Molecule Three-Color FRET. Biophys. J. *87*, 1328–1337.
73. Holzmeister, P., Gietl, A., and Tinnefeld, P. (2014). Geminate Recombination as a Photoprotection Mechanism for Fluorescent Dyes. Angew. Chemie Int. Ed. *53*, 5685–5688.
74. Hoskins, A., Gelles, J., and Moore, M. (2011). New insights into the spliceosome by single molecule fluorescence microscopy. Curr. Opin. Chem. Biol. *15*, 864–870.
75. Hu, T., Grosberg, a Y., and Shklovskii, B.I. (2006). How Proteins Search for Their Specific Sites on DNA: The Role of DNA Conformation. Biophys. J. *90*, 2731–2744.
76. Huang, F., Rajagopalan, S., Settanni, G., Marsh, R.J., Armoogum, D.A., Nicolaou, N., Bain, A.J., Lerner, E., Haas, E., Ying, L., et al. (2009). Multiple conformations of full-length p53 detected with single-molecule fluorescence resonance energy transfer. Proc. Natl. Acad. Sci. *106*, 20758–20763.
77. Huhle, A., Klaue, D., Brutzer, H., Daldrop, P., Joo, S., Otto, O., Keyser, U.F., and Seidel, R. (2015a). Camera-based three-dimensional real-time particle tracking at kHz rates and Ångström accuracy. Nat. Commun. *6*, 5885.
78. Huhle, A., Klaue, D., Brutzer, H., Daldrop, P., Joo, S., Otto, O., Keyser, U.F., and Seidel, R. (2015b). Camera-based three-dimensional real-time particle tracking at kHz rates and Ångström accuracy. Nat. Commun. *6*, 5885.
79. Hwang, H., Kim, H., and Myong, S. (2011). Protein induced fluorescence enhancement as a single molecule assay with short distance sensitivity. Proc. Natl. Acad. Sci. *108*, 7414–7418.
80. Jack, W.E., Terry, B.J., and Modrich, P. (1982). Involvement of outside DNA sequences in the major kinetic path by which EcoRI endonuclease locates and leaves its recognition sequence. Proc. Natl. Acad. Sci. *79*, 4010–4014.
81. Jeltsch, A., and Pingoud, A. (1998). Kinetic Characterization of Linear Diffusion of the Restriction Endonuclease Eco RV on DNA †. Biochemistry *37*, 2160–2169.
82. Jeltsch, A., Alves, J., Wolfes, H., Maass, G., and Pingoud, A. (1994). Pausing of the Restriction Endonuclease EcoRI during Linear Diffusion on DNA. Biochemistry *33*, 10215–10219.

83. Joo, C., Balci, H., Ishitsuka, Y., Buranachai, C., and Ha, T. (2008). Advances in Single-Molecule Fluorescence Methods for Molecular Biology. Annu. Rev. Biochem. *77*, 51–76.
84. Kapanidis, A.N., Margeat, E., Ho, S.O., Kortkhonjia, E., Weiss, S., and Ebright, R.H. (2006). Initial Transcription by RNA Polymerase Proceeds Through a DNA-Scrunching Mechanism. Science (80-.). *314*, 1144–1147.
85. Kelly, T.J., and Smith, H.O. (1970). A restriction enzyme from Hemophilus influenzae. II. J. Mol. Biol. *51*, 393–409.
86. Kemmerich, F.E., Swoboda, M., Kauert, D.J., Grieb, M.S., Hahn, S., Schwarz, F.W., Seidel, R., and Schlierf, M. (2015). Simultaneous single-molecule force and fluorescence sampling of DNA nanostructure conformations using magnetic tweezers. Nano Lett. acs.nanolett.5b03956.
87. Kemmerich, F.E., Kasaciunaite, K., and Seidel, R. (2016). Modular magnetic tweezers for single-molecule characterizations of helicases. Methods *108*, 4–13.
88. Kessler, C. (1991). The digoxigenin:anti-digoxigenin (DIG) technology—a survey on the concept and realization of a novel bioanalytical indicator system. Mol. Cell. Probes *5*, 161–205.
89. Kim, H., and Ha, T. (2013). Single-molecule nanometry for biological physics. Reports Prog. Phys. *76*, 16601.
90. Kim, J.H., and Larson, R.G. (2007). Single-molecule analysis of 1D diffusion and transcription elongation of T7 RNA polymerase along individual stretched DNA molecules. Nucleic Acids Res. *35*, 3848–3858.
91. Kim, C.H., Axup, J.Y., and Schultz, P.G. (2013a). Protein conjugation with genetically encoded unnatural amino acids. Curr Opin Chem Biol *17*, 412–419.
92. Kim, H., Abeysirigunawarden, S.C., Chen, K., Mayerle, M., Ragunathan, K., Luthey-Schulten, Z., Ha, T., and Woodson, S. a (2014). Protein-guided RNA dynamics during early ribosome assembly. Nature *506*, 334–338.
93. Kim, J., Seo, M.-H., Lee, S., Cho, K., Yang, A., Woo, K., Kim, H.-S., and Park, H.-S. (2013b). Simple and Efficient Strategy for Site-Specific Dual Labeling of Proteins for Single-Molecule Fluorescence Resonance Energy Transfer Analysis. Anal. Chem. *85*, 1468–1474.
94. Kim, S.Y., Miller, E.J., Frydman, J., and Moerner, W.E. (2010). Action of the Chaperonin GroEL/ES on a Non-native Substrate Observed with Single-Molecule FRET. J. Mol. Biol. *401*, 553–563.
95. Kim, Y.C., Grable, J.C., Love, R., Greene, P.J., and Rosenberg, J.M. (1990). Refinement of Eco RI endonuclease crystal structure: a revised protein chain tracing. Science *249*, 1307–1309.
96. Klenin, K. V., Merlitz, H., Langowski, J., and Wu, C.-X. (2006). Facilitated Diffusion of DNA-Binding Proteins. Phys. Rev. Lett. *96*, 18104.

97. Kochaniak, A.B., Habuchi, S., Loparo, J.J., Chang, D.J., Cimprich, K.A., Walter, J.C., and van Oijen, A.M. (2009). Proliferating Cell Nuclear Antigen Uses Two Distinct Modes to Move along DNA. J. Biol. Chem. *284*, 17700–17710.
98. Kolesov, G., Wunderlich, Z., Laikova, O.N., Gelfand, M.S., and Mirny, L. a (2007). How gene order is influenced by the biophysics of transcription regulation. Proc. Natl. Acad. Sci. *104*, 13948–13953.
99. Komazin-Meredith, G., Mirchev, R., Golan, D.E., van Oijen, A.M., and Coen, D.M. (2008). Hopping of a processivity factor on DNA revealed by single-molecule assays of diffusion. Proc. Natl. Acad. Sci. *105*, 10721–10726.
100. Kostiuk, G., Sasnauskas, G., Tamulaitiene, G., and Siksnys, V. (2011). Degenerate sequence recognition by the monomeric restriction enzyme: single mutation converts BcnI into a strand-specific nicking endonuclease. Nucleic Acids Res. *39*, 3744–3753.
101. Kricka, L.J., and Fortina, P. (2009). Analytical Ancestry: “Firsts” in Fluorescent Labeling of Nucleosides, Nucleotides, and Nucleic Acids. Clin. Chem. *55*, 670–683.
102. Kurpiewski, M.R., Engler, L.E., Wozniak, L.A., Kobylanska, A., Koziolkiewicz, M., Stec, W.J., and Jen-Jacobson, L. (2004). Mechanisms of Coupling between DNA Recognition Specificity and Catalysis in EcoRI Endonuclease. Structure *12*, 1775–1788.
103. Lakowicz, J.R. (2006). Principles of Fluorescence Spectroscopy (Boston, MA: Springer US).
104. Lanz, M. a., and Klostermeier, D. (2011). Guiding strand passage: DNA-induced movement of the gyrase C-terminal domains defines an early step in the supercoiling cycle. Nucleic Acids Res. *39*, 9681–9694.
105. Laurence, T. a., Kwon, Y., Johnson, A., Hollars, C.W., O’Donnell, M., Camarero, J. a., and Barsky, D. (2008). Motion of a DNA Sliding Clamp Observed by Single Molecule Fluorescence Spectroscopy. J. Biol. Chem. *283*, 22895–22906.
106. Laurens, N., Bellamy, S.R.W., Harms, A.F., Kovacheva, Y.S., Halford, S.E., and Wuite, G.J.L. (2009). Dissecting protein-induced DNA looping dynamics in real time. Nucleic Acids Res. *37*, 5454–5464.
107. Lee, J., Lee, S., Ragunathan, K., Joo, C., Ha, T., and Hohng, S. (2010). Single-Molecule Four-Color FRET. Angew. Chemie Int. Ed. *49*, 9922–9925.
108. Lee, M., Lipfert, J., Sanchez, H., Wyman, C., and Dekker, N.H. (2013). Structural and torsional properties of the RAD51-dsDNA nucleoprotein filament. Nucleic Acids Res. *41*, 7023–7030.
109. Lee, N.K., Kapanidis, A.N., Wang, Y., Michalet, X., Mukhopadhyay, J.,

Ebright, R.H., and Weiss, S. (2005). Accurate FRET Measurements within Single Diffusing Biomolecules Using Alternating-Laser Excitation. Biophys. J. *88*, 2939–2953.
110. Lee, N.K., Kapanidis, A.N., Koh, H.R., Korlann, Y., Ho, S.O., Kim, Y., Gassman, N., Kim, S.K., and Weiss, S. (2007). Three-Color Alternating-Laser Excitation of Single Molecules: Monitoring Multiple Interactions and Distances. Biophys. J. *92*, 303–312.
111. Lin, Y., Zhao, T., Jian, X., Farooqui, Z., Qu, X., He, C., Dinner, A.R., and Scherer, N.F. (2009). Using the Bias from Flow to Elucidate Single DNA Repair Protein Sliding and Interactions with DNA. Biophys. J. *96*, 1911–1917.
112. Liu, S., Abbondanzieri, E. a, Rausch, J.W., Grice, S.F.J.L., and Zhuang, X. (2008). Slide into Action: Dynamic Shuttling of HIV Reverse Transcriptase on Nucleic Acid Substrates. Science (80-.). *322*, 1092–1097.
113. Liu, S., Chistol, G., Hetherington, C.L., Tafoya, S., Aathavan, K., Schnitzbauer, J., Grimes, S., Jardine, P.J., and Bustamante, C. (2014). A Viral Packaging Motor Varies Its DNA Rotation and Step Size to Preserve Subunit Coordination as the Capsid Fills. Cell *157*, 702–713.
114. Loura, L. (2012). Simple Estimation of Förster Resonance Energy Transfer (FRET) Orientation Factor Distribution in Membranes. Int. J. Mol. Sci. *13*, 15252–15270.
115. Loverdo, C., Bénichou, O., Voituriez, R., Biebricher, a., Bonnet, I., and Desbiolles, P. (2009). Quantifying hopping and jumping in facilitated diffusion of DNA-binding proteins. Phys. Rev. Lett. *102*, 1–4.
116. Ma, J., Bai, L., and Wang, M.D. (2013). Transcription Under Torsion. Science (80-.). *340*, 1580–1583.
117. Majumdar, D.S., Smirnova, I., Kasho, V., Nir, E., Kong, X., Weiss, S., and Kaback, H.R. (2007). Single-molecule FRET reveals sugar-induced conformational dynamics in LacY. Proc. Natl. Acad. Sci. *104*, 12640–12645.
118. Manosas, M., Meglio, A., Spiering, M.M., Ding, F., Benkovic, S.J., Barre, F.-X., Saleh, O.A., Allemand, J.F., Bensimon, D., and Croquette, V. (2010). Magnetic Tweezers for the Study of DNA Tracking Motors. In Methods in Enzymology, pp. 297–320.
119. Medintz, I.L., Uyeda, H.T., Goldman, E.R., and Mattoussi, H. (2005). Quantum dot bioconjugates for imaging, labelling and sensing. Nat. Mater. *4*, 435–446.
120. Michalet, X. (2010). Mean square displacement analysis of single-particle trajectories with localization error: Brownian motion in an isotropic medium. Phys. Rev. E. Stat. Nonlin. Soft Matter Phys. *82*, 41914.
121. Miyawaki, A. (2011). Development of Probes for Cellular Functions Using

Fluorescent Proteins and Fluorescence Resonance Energy Transfer. Annu. Rev. Biochem. *80*, 357–373.
122. Mori, T., Vale, R.D., and Tomishige, M. (2007). How kinesin waits between steps. Nature *450*, 750–754.
123. Müller, B.K., Zaychikov, E., Bräuchle, C., and Lamb, D.C. (2005). Pulsed Interleaved Excitation. Biophys. J. *89*, 3508–3522.
124. Munro, J.B., Altman, R.B., O'Connor, N., and Blanchard, S.C. (2007). Identification of Two Distinct Hybrid State Intermediates on the Ribosome. Mol. Cell *25*, 505–517.
125. Neuman, K.C., and Nagy, A. (2008). Single-molecule force spectroscopy: optical tweezers, magnetic tweezers and atomic force microscopy. Nat. Methods *5*, 491–505.
126. Northrup, S.H., Boles, J.O., and Reynolds, J.C. (1988). Brownian dynamics of cytochrome c and cytochrome c peroxidase association. Science (80-.). *241*, 67 LP-70.
127. Orm, M., Cubitt, A.B., Kallio, K., Gross, L.A., Tsien, R.Y., and Remington, S.J. (1996). Crystal Structure of the Aequorea victoria Green Fluorescent Protein. Science (80-.). *273*, 1392–1395.
128. Otto, O., Czerwinski, F., Gornall, J.L., Stober, G., Oddershede, L.B., Seidel, R., and Keyser, U.F. (2010). Real-time particle tracking at 10,000 fps using optical fiber illumination. Opt. Express *18*, 22722.
129. Petryayeva, E., Algar, W.R., and Medintz, I.L. (2013). Quantum Dots in Bioanalysis: A Review of Applications Across Various Platforms for Fluorescence Spectroscopy and Imaging. Appl. Spectrosc. *67*, 215–252.
130. Pingoud, A., Wilson, G.G., and Wende, W. (2014). Type II restriction endonucleases—a historical perspective and more. Nucleic Acids Res. *42*, 7489–7527.
131. Pollak, A.J., Chin, A.T., and Reich, N.O. (2014). Distinct Facilitated Diffusion Mechanisms by E. coli Type II Restriction Endonucleases. Biochemistry *53*, 7028–7037.
132. Porecha, R.H., and Stivers, J.T. (2008). Uracil DNA glycosylase uses DNA hopping and short-range sliding to trap extrahelical uracils. Proc. Natl. Acad. Sci. *105*, 10791–10796.
133. Posson, D.J., Ge, P., Miller, C., Bezanilla, F., and Selvin, P.R. (2005). Small vertical movement of a K+ channel voltage sensor measured with luminescence energy transfer. Nature *436*, 848–851.
134. Preus, S., and Wilhelmsson, L.M. (2012). Advances in Quantitative FRET-Based Methods for Studying Nucleic Acids. ChemBioChem *13*, 1990–2001.
135. Qian, H., Sheetz, M.P., and Elson, E.L. (1991). Single particle tracking. Analysis of diffusion and flow in two-dimensional systems. Biophys. J. *60*,

910–921.
136. Qiu, R., DeRocco, V.C., Harris, C., Sharma, A., Hingorani, M.M., Erie, D.A., and Weninger, K.R. (2012). Large conformational changes in MutS during DNA scanning, mismatch recognition and repair signalling. EMBO J. *31*, 2528–2540.
137. Qiu, R., Sakato, M., Sacho, E.J., Wilkins, H., Zhang, X., Modrich, P., Hingorani, M.M., Erie, D.A., and Weninger, K.R. (2015). MutL traps MutS at a DNA mismatch. Proc. Natl. Acad. Sci. *112*, 10914–10919.
138. Ramanathan, S.P., van Aelst, K., Sears, A., Peakman, L.J., Diffin, F.M., Szczelkun, M.D., and Seidel, R. (2009). Type III restriction enzymes communicate in 1D without looping between their target sites. Proc. Natl. Acad. Sci. *106*, 1748–1753.
139. Revyakin, A., Ebright, R.H., and Strick, T.R. (2004). Promoter unwinding and promoter clearance by RNA polymerase: Detection by single-molecule DNA nanomanipulation. Proc. Natl. Acad. Sci. *101*, 4776–4780.
140. Revyakin, A., Liu, C., Ebright, R.H., and Strick, T.R. (2006). Abortive Initiation and Productive Initiation by RNA Polymerase Involve DNA Scrunching. Science (80-.). *314*, 1139–1143.
141. Richter, P.H., and Eigen, M. (1974). Diffusion controlled reaction rates in spheroidal geometry. Biophys. Chem. *2*, 255–263.
142. Riggs, A.D., Bourgeois, S., and Cohn, M. (1970). The lac represser-operator interaction. J. Mol. Biol. *53*, 401–417.
143. Rigler, R., and Elson, E.. (2001). Fluorescence Correlation Spectroscopy. Theory and Applications (Springer Series in Chemical Physics).
144. Rowland, M.M., Schonhoft, J.D., McKibbin, P.L., David, S.S., and Stivers, J.T. (2014). Microscopic mechanism of DNA damage searching by hOGG1. Nucleic Acids Res. *42*, 9295–9303.
145. Roy, R., Hohng, S., and Ha, T. (2008). A practical guide to single-molecule FRET. Nat. Methods *5*, 507–516.
146. Ruhnow, F., Zwicker, D., and Diez, S. (2011). Tracking Single Particles and Elongated Filaments with Nanometer Precision. Biophys. J. *100*, 2820–2828.
147. Rutkauskas, M., Sinkunas, T., Songailiene, I., Tikhomirova, M., Siksnys, V., and Seidel, R. (2015). Directional R-loop formation by the CRISPR-cas surveillance complex cascade provides efficient off-target site rejection. Cell Rep. *10*, 1534–1543.
148. Ryu, Y., and Schultz, P.G. (2006). Efficient incorporation of unnatural amino acids into proteins in Escherichia coli. Nat. Methods *3*, 263–265.
149. Sambrook, J., E. F., F., and Maniatis, T. (1989). Molecular cloning: a laboratory manual (New York: Cold Spring Harbor, N.Y.: Cold Spring Harbor Laboratory).

150. Sapranauskas, R., Sasnauskas, G., Lagunavicius, A., Vilkaitis, G., Lubys, A., and Siksnys, V. (2000). Novel Subtype of Type IIs Restriction Enzymes: BfiI ENDONUCLEASE EXHIBITS SIMILARITIES TO THE EDTA-RESISTANT NUCLEASE Nuc OF SALMONELLA TYPHIMURIUM. J. Biol. Chem. *275*, 30878–30885.
151. Sasmal, D.K., and Lu, H.P. (2014). Single-Molecule Patch-Clamp FRET Microscopy Studies of NMDA Receptor Ion Channel Dynamics in Living Cells: Revealing the Multiple Conformational States Associated with a Channel at Its Electrical Off State. J. Am. Chem. Soc. *136*, 12998–13005.
152. Sasnauskas, G., Jeltsch, A., Pingoud, A., and Siksnys, V. (1999). Plasmid DNA Cleavage by Mun I Restriction Enzyme: Single-Turnover and Steady-State Kinetic Analysis †. Biochemistry *38*, 4028–4036.
153. Sasnauskas, G., Zakrys, L., Zaremba, M., Cosstick, R., Gaynor, J.W., Halford, S.E., and Siksnys, V. (2010). A novel mechanism for the scission of double-stranded DNA: BfiI cuts both 3′–5′ and 5′–3′ strands by rotating a single active site. Nucleic Acids Res. *38*, 2399–2410.
154. Sasnauskas, G., Kostiuk, G., Tamulaitis, G., and Siksnys, V. (2011). Target site cleavage by the monomeric restriction enzyme BcnI requires translocation to a random DNA sequence and a switch in enzyme orientation. Nucleic Acids Res. *39*, 8844–8856.
155. Saxton, M.J., and Jacobson, K. (1997). SINGLE-PARTICLE TRACKING:Applications to Membrane Dynamics. Annu. Rev. Biophys. Biomol. Struct. *26*, 373–399.
156. Schneider, C. a, Rasband, W.S., and Eliceiri, K.W. (2012). NIH Image to ImageJ: 25 years of image analysis. Nat. Methods *9*, 671–675.
157. Schurr, J.M. (1979). The one-dimensional diffusion coefficient of proteins absorbed on DNA. Hydrodynamic considerations. Biophys. Chem. *9*, 413–414.
158. Schwarz, F.W., Toth, J., van Aelst, K., Cui, G., Clausing, S., Szczelkun, M.D., and Seidel, R. (2013). The Helicase-Like Domains of Type III Restriction Enzymes Trigger Long-Range Diffusion Along DNA. Science (80-.). *340*, 353–356.
159. Seidel, R., van Noort, J., van der Scheer, C., Bloom, J.G.P., Dekker, N.H., Dutta, C.F., Blundell, A., Robinson, T., Firman, K., and Dekker, C. (2004). Real-time observation of DNA translocation by the type I restriction modification enzyme EcoR124I. Nat. Struct. Mol. Biol. *11*, 838–843.
160. Seidel, R., Bloom, J.G., van Noort, J., Dutta, C.F., Dekker, N.H., Firman, K., Szczelkun, M.D., and Dekker, C. (2005). Dynamics of initiation, termination and reinitiation of DNA translocation by the motor protein Eco R124I. EMBO J. *24*, 4188–4197.
161. Seidel, R., Bloom, J.G., Dekker, C., and Szczelkun, M.D. (2008). Motor

step size and ATP coupling efficiency of the dsDNA translocase EcoR124I. EMBO J. *27*, 1388–1398.
162. Shaner, N.C., Steinbach, P.A., and Tsien, R.Y. (2005). A guide to choosing fluorescent proteins. Nat. Methods *2*, 905–909.
163. Sharp, K., Fine, R., and Honig, B. (1987). Computer simulations of the diffusion of a substrate to an active site of an enzyme. Science (80-.). *236*, 1460–1463.
164. Sierra, H., Cordova, M., Chen, C.-S.J., and Rajadhyaksha, M. (2015). Confocal Imaging–Guided Laser Ablation of Basal Cell Carcinomas: An Ex Vivo Study. J. Invest. Dermatol. *135*, 612–615.
165. Siksnys, V., Skirgaila, R., Sasnauskas, G., Urbanke, C., Cherny, D., Grazulis, S., and Huber, R. (1999). The Cfr10I restriction enzyme is functional as a tetramer. J. Mol. Biol. *291*, 1105–1118.
166. Sisamakis, E., Valeri, A., Kalinin, S., Rothwell, P.J., and Seidel, C.A.M. (2010). Accurate Single-Molecule FRET Studies Using Multiparameter Fluorescence Detection. In Methods in Enzymology, (Elsevier Inc.), pp. 455–514.
167. Slutsky, M., and Mirny, L. a (2004). Kinetics of Protein-DNA Interaction: Facilitated Target Location in Sequence-Dependent Potential. Biophys. J. *87*, 4021–4035.
168. Smith, S.B., Finzi, L., and Bustamante, C. (1992). Direct mechanical measurements of the elasticity of single DNA molecules by using magnetic beads. Science *258*, 1122–1126.
169. Sokolowska, M., Kaus-Drobek, M., Czapinska, H., Tamulaitis, G., Szczepanowski, R.H., Urbanke, C., Siksnys, V., and Bochtler, M. (2007). Monomeric Restriction Endonuclease BcnI in the Apo Form and in an Asymmetric Complex with Target DNA. J. Mol. Biol. *369*, 722–734.
170. Stanford, N.P. (2000). One- and three-dimensional pathways for proteins to reach specific DNA sites. EMBO J. *19*, 6546–6557.
171. Stennett, E.M.S., Ciuba, M. a, and Levitus, M. (2014). Photophysical processes in single molecule organic fluorescent probes. Chem. Soc. Rev. *43*, 1057–1075.
172. Strick, T., Allemand, J.-F., Croquette, V., and Bensimon, D. (2001). The Manipulation of Single Biomolecules. Phys. Today *54*, 46–51.
173. Strick, T.R., Allemand, J.-F., Bensimon, D., Bensimon, A., and Croquette, V. (1996). The Elasticity of a Single Supercoiled DNA Molecule. Science (80-.). *271*, 1835–1837.
174. Strick, T.R., Dessinges, M.-N., Charvin, G., Dekker, N.H., Allemand, J.-F., Bensimon, D., and Croquette, V. (2003). Stretching of macromolecules and proteins. Reports Prog. Phys. *66*, 1–45.
175. Stryer, L. (1978). Fluorescence Energy Transfer as a Spectroscopic Ruler.

Annu. Rev. Biochem. *47*, 819–846.
176. Tafvizi, A., Mirny, L.A., and van Oijen, A.M. (2011a). Dancing on DNA: Kinetic Aspects of Search Processes on DNA. ChemPhysChem *12*, 1481–1489.
177. Tafvizi, A., Huang, F., Fersht, A.R., Mirny, L.A., and van Oijen, A.M. (2011b). A single-molecule characterization of p53 search on DNA. Proc. Natl. Acad. Sci. *108*, 563–568.
178. Tamulaitis, G., Mucke, M., and Siksnys, V. (2006). Biochemical and mutational analysis of Eco RII functional domains reveals evolutionary links between restriction enzymes. FEBS Lett. *580*, 1665–1671.
179. Taylor, J.D., Badcoe, I.G., Clarke, A.R., and Halford, S.E. (1991). EcoRV restriction endonuclease binds all DNA sequences with equal affinity. Biochemistry *30*, 8743–8753.
180. Terry, B.J., Jack, W.E., and Modrich, P. (1985). Facilitated diffusion during catalysis by EcoRI endonuclease. Nonspecific interactions in EcoRI catalysis. J. Biol. Chem. *260*, 13130–13137.
181. Theissen, B., Karow, A.R., Kohler, J., Gubaev, A., and Klostermeier, D. (2008). Cooperative binding of ATP and RNA induces a closed conformation in a DEAD box RNA helicase. Proc. Natl. Acad. Sci. *105*, 548–553.
182. Thompson, R.E., Larson, D.R., and Webb, W.W. (2002). Precise Nanometer Localization Analysis for Individual Fluorescent Probes. Biophys. J. *82*, 2775–2783.
183. Tian, Y., Martinez, M.M., and Pappas, D. (2011). Fluorescence Correlation Spectroscopy: A Review of Biochemical and Microfluidic Applications. Appl. Spectrosc. *65*, 115–124.
184. Toseland, C.P. (2013). Fluorescent labeling and modification of proteins. J. Chem. Biol. *6*, 85–95.
185. Tsien, R.Y. (1998). THE GREEN FLUORESCENT PROTEIN. Annu. Rev. Biochem. *67*, 509–544.
186. Uphoff, S., Holden, S.J., Le Reste, L., Periz, J., van de Linde, S., Heilemann, M., and Kapanidis, A.N. (2010). Monitoring multiple distances within a single molecule using switchable FRET. Nat. Methods *7*, 831–836.
187. Vámosi, G., Gohlke, C., and Clegg, R.M. (1996). Fluorescence characteristics of 5-carboxytetramethylrhodamine linked covalently to the 5’ end of oligonucleotides: multiple conformers of single-stranded and double-stranded dye-DNA complexes. Biophys. J. *71*, 972–994.
188. Veksler, A., and Kolomeisky, A.B. (2013). Speed-Selectivity Paradox in the Protein Search for Targets on DNA: Is It Real or Not? J. Phys. Chem. B *117*, 12695–12701.

189. De Vlaminck, I., and Dekker, C. (2012). Recent Advances in Magnetic Tweezers. Annu. Rev. Biophys. *41*, 453–472.
190. De Vlaminck, I., Henighan, T., van Loenhout, M.T.J., Pfeiffer, I., Huijts, J., Kerssemakers, J.W.J., Katan, A.J., van Langen-Suurling, A., van der Drift, E., Wyman, C., et al. (2011). Highly Parallel Magnetic Tweezers by Targeted DNA Tethering. Nano Lett. *11*, 5489–5493.
191. Vlijm, R., Smitshuijzen, J.S.J., Lusser, A., and Dekker, C. (2012). NAP1-Assisted Nucleosome Assembly on DNA Measured in Real Time by Single-Molecule Magnetic Tweezers. PLoS One *7*, e46306.
192. Vlijm, R., Lee, M., Lipfert, J., Lusser, A., Dekker, C., and Dekker, N.H. (2015). Nucleosome Assembly Dynamics Involve Spontaneous Fluctuations in the Handedness of Tetrasomes. Cell Rep. *10*, 216–225.
193. Vogelsang, J., Kasper, R., Steinhauer, C., Person, B., Heilemann, M., Sauer, M., and Tinnefeld, P. (2008). A Reducing and Oxidizing System Minimizes Photobleaching and Blinking of Fluorescent Dyes. Angew. Chemie Int. Ed. *47*, 5465–5469.
194. Walker, D., Moore, G.R., James, R., and Kleanthous, C. (2003). Thermodynamic Consequences of Bipartite Immunity Protein Binding to the Ribosomal Ribonuclease Colicin E3 †. Biochemistry *42*, 4161–4171.
195. Wang, Y.M., Austin, R.H., and Cox, E.C. (2006). Single Molecule Measurements of Repressor Protein 1D Diffusion on DNA. Phys. Rev. Lett. *97*, 48302.
196. Watanabe, R., and Noji, H. (2015). Characterization of the temperature-sensitive reaction of F1-ATPase by using single-molecule manipulation. Sci. Rep. *4*, 4962.
197. Watanabe, R., Iino, R., and Noji, H. (2010). Phosphate release in F1-ATPase catalytic cycle follows ADP release. Nat. Chem. Biol. *6*, 814–820.
198. Wilkins, D.K., Grimshaw, S.B., Receveur, V., Dobson, C.M., Jones, J. a., and Smith, L.J. (1999). Hydrodynamic radii of native and denatured proteins measured by pulse field gradient NMR techniques. Biochemistry *38*, 16424–16431.
199. Wright, D.J., Jack, W.E., and Modrich, P. (1999). The kinetic mechanism of EcoRI endonuclease. J. Biol. Chem. *274*, 31896–31902.
200. Zaremba, M., Sasnauskas, G., Urbanke, C., and Siksnys, V. (2005). Conversion of the Tetrameric Restriction Endonuclease Bse634I into a Dimer: Oligomeric Structure–Stability–Function Correlations. J. Mol. Biol. *348*, 459–478.
201. Zaremba, M., Owsicka, A., Tamulaitis, G., Sasnauskas, G., Shlyakhtenko, L.S., Lushnikov, A.Y., Lyubchenko, Y.L., Laurens, N., van den Broek, B., Wuite, G.J.L., et al. (2010). DNA synapsis through transient tetramerization triggers cleavage by Ecl18kI restriction enzyme. Nucleic

Acids Res. *38*, 7142–7154.
202. Zhang, Y., and Wang, T.-H. (2012). Quantum Dot Enabled Molecular Sensing and Diagnostics. Theranostics *2*, 631–654.
203. Zhao, Y., Terry, D.S., Shi, L., Quick, M., Weinstein, H., Blanchard, S.C., and Javitch, J. a (2011). Substrate-modulated gating dynamics in a Na+-coupled neurotransmitter transporter homologue. Nature *474*, 109–113.
204. Zheng, L. (2004). An efficient one-step site-directed and site-saturation mutagenesis protocol. Nucleic Acids Res. *32*, e115–e115.
205. Zheng, Q., Juette, M.F., Jockusch, S., Wasserman, M.R., Zhou, Z., Altman, R.B., and Blanchard, S.C. (2014). Ultra-stable organic fluorophores for single-molecule research. Chem. Soc. Rev. *43*, 1044–1056.
206. Zhou, D., Piper, J.D., Abell, C., Klenerman, D., Kang, D.-J., and Ying, L. (2005). Fluorescence resonance energy transfer between a quantum dot donor and a dye acceptor attached to DNA. Chem. Commun. 4807.